Lawrence Berkeley National Laboratory

Title
Diffusion in silicon isotope heterostructures

Permalink
https://escholarship.org/uc/item/8bp3g9qr

Author
Silvestri, Hughes Howland

Publication Date
2004-05-14

Diffusion in Silicon Isotope Heterostructures

by

Hughes Howland Silvestri

B.S. (Fairfield University) 1997
M.S. (University of California, Berkeley) 2001

A dissertation submitted in partial satisfaction of the

requirements for the degree of

Doctor of Philosophy

in

Engineering – Materials Science and Engineering

in the

GRADUATE DIVISION

of the

UNIVERSITY OF CALIFORNIA, BERKELEY

Committee in charge:

Professor Eugene E. Haller, Chair
Professor Oscar D. Dubon
Professor Tsu-Jae King
Professor Hartmut A. Bracht

Spring 2004

Abstract

Diffusion in Silicon Isotope Heterostructures

by

Hughes Howland Silvestri

Doctor of Philosophy in Engineering – Materials Science and Engineering

University of California, Berkeley

Professor Eugene E. Haller, Chair

The simultaneous diffusion of Si and the dopants B, P, and As has been studied
by the use of a multilayer structure of isotopically enriched Si. This structure, consisting
of 5 pairs of 120 nm thick natural Si and ^{28}Si enriched layers, enables the observation of
^{30}Si self-diffusion from the natural layers into the ^{28}Si enriched layers, as well as dopant
diffusion from an implanted source in an amorphous Si cap layer, via Secondary Ion
Mass Spectrometry (SIMS). The dopant diffusion created regions of the multilayer
structure that were extrinsic at the diffusion temperatures. In these regions, the Fermi
level shift due to the extrinsic condition altered the concentration and charge state of the
native defects involved in the diffusion process, which affected the dopant and self-
diffusion.

The simultaneously recorded diffusion profiles enabled the modeling of the
coupled dopant and self-diffusion. From the modeling of the simultaneous diffusion, the
dopant diffusion mechanisms, the native defect charge states, and the self- and dopant
diffusion coefficients can be determined. This information is necessary to enhance the
physical modeling of dopant diffusion in Si. It is of particular interest to the modeling of

1

future electronic Si devices, where the nanometer-scale features have created the need for precise physical models of atomic diffusion in Si.

The modeling of the experimental profiles of simultaneous diffusion of B and Si under p-type extrinsic conditions revealed that both species are mediated by neutral and singly, positively charged Si self-interstitials. The diffusion of As and Si under extrinsic n-type conditions yielded a model consisting of the interstitialcy and vacancy mechanisms of diffusion via singly negatively charged self-interstitials and neutral vacancies. The simultaneous diffusion of P and Si has been modeled on the basis of neutral and singly negatively charged self-interstitials and neutral and singly positively charged P species. Additionally, the temperature dependence of the diffusion coefficient of Si in Ge was measured over the temperature range of 550 °C to 900 °C using a buried Si layer in an epitaxially grown Ge layer.

Acknowledgments

I would like to thank my advisor, Professor Eugene Haller, for his continuous support and guidance throughout my graduate career. I would also like to thank my thesis committee members Professors Oscar Dubon, Tsu-Jae King, and Hartmut Bracht for their efforts in reviewing my thesis, as well as my qualifying exam committee members Professors Eicke Weber and T. N. Narasimhan.

This work would not have been possible without the efforts of my research collaborators. Professor Hartmut Bracht has worked tirelessly on all aspects of the diffusion research, not the least of which involved his patience in educating me on the fundamentals of diffusion in semiconductors. Professor Arne Larsen and his group at the University of Aarhus in Denmark, used their expertise in MBE growth to grow the diffusion structures. I would also like to thank Dimitry Kouzminov for his efforts with our SIMS analysis.

I am grateful for the help and support of all of the members of the Haller group, specifically Abe, Ben, and Supriya for their support both in and out of the lab. I would specifically like to thank Jeff Beeman for all of his hard work, patience, and insight throughout my time here, and Ian Sharp for his efforts on the diffusion project and his continued interest and discussion of the research. I would like to acknowledge the aid of former members of the Haller group, Chris, Oscar, Danielle, Marlene, Dawnelle, and Raechelle, whose advice and friendship has been essential to my success. I would like to thank David Hom for his continued assistance at LBNL. I would also like to thank

Professor Nancy Haegel for believing in me, and all those who were acknowledged for their efforts with my Master's thesis.

Table of Contents

1   Introduction

1.1   Motivation and Brief History of Diffusion in Si and SiGe

The current trend in modern silicon-based semiconductor device manufacturing, which calls for continued scaling of device dimensions to below 100 nm, has created the need for a greater control of the diffusion which occurs during device processing [ITRS, 2001]. During processing the silicon wafer is exposed to temperatures on the order of 1000 °C. At such temperatures, diffusion of the dopant atoms, which form the major device features, can occur and may result in a loss of the desired device dimension control.

Variation in device dimensions can adversely affect the electronic behavior of the device. Figure 1.1 is a schematic of a MOS (metal-oxide-semiconductor) transistor showing the effects of device dimension on the channel voltage [Packan, 2000]. The figure is an illustration of the potential voltage contours for two devices, left and right, with identical channel lengths but differing junction depths. The devices shown are biased to the "off" state, where no current should flow through the channel. A high potential across the channel will lead to leakage current and a degradation of the "off" state. The desired structure with low channel potential is shown on the right side of Figure 1.1. Failure to control the diffusion of dopants in the source and drain regions of the device can lead to the deeper junctions seen on the left side of Figure 1.1. The resulting large potential in the channel region of the device will create leakage currents in the "off" state of the transistor, causing a break down of device performance.

1
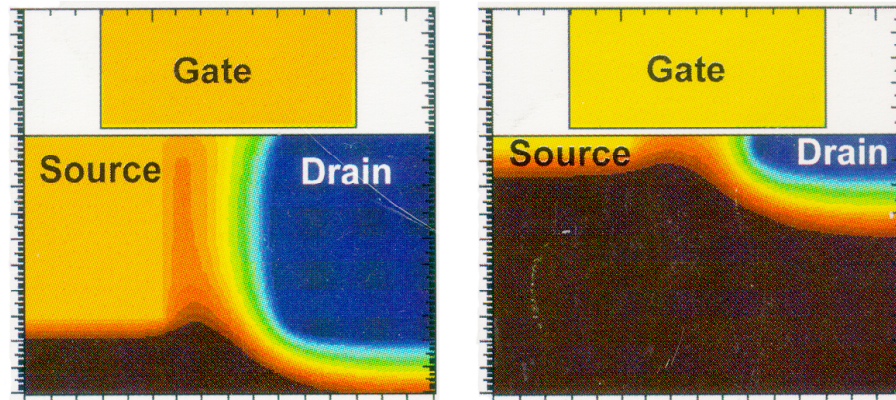
Figure 1.1 Diagram of the cross-sectional voltage distribution in the channel of a MOS transistor for two devices with identical channel lengths (0.1 μm), but with large source and drain regions (left) and small source and drain regions (right). The large potential in the channel on the left side can lead to leakage current [Packan, 2000]

Control of the device dimensions, taking into account the diffusion that occurs, can be achieved through greater understanding of the diffusion process. Diffusion in silicon has been studied in great detail over the last 50 years, and much is known about the diffusion of dopants [see e.g., Stolwijk, 1998]. However, what has been lacking up to this point is a precise and quantitative knowledge of the numerous interactions of dopant atoms with native defects in Si, interstitial host atoms and vacancies.

By simultaneously studying the self-diffusion of Si, which involves the movement of interstitials and vacancies, and the diffusion of dopants in Si, a greater understanding of the interaction of dopant atoms with native defects during diffusion can be achieved. Specifically, this dual approach will enable the determination of the charge states of the native defects during diffusion under intrinsic and extrinsic conditions, the contributions of the native defect charge states to self-diffusion, and any dopant or self-diffusion enhancement under extrinsic conditions. To accomplish these goals using simultaneous

2

dopant and self-diffusion studies in Si, stable isotope heterostructures of Si were employed to monitor the self-diffusion during the simultaneous diffusion of dopants.

One of the common means of measuring self-diffusion of atoms in a solid is to use the radioactive tracer technique. This technique involves the diffusion of a radioactive isotope of the element to be studied from the surface into the material. The diffusion profile is determined by sectioning the material and measuring the activity of each section. By knowing the initial activity and the half-life of the isotope, the concentration of the diffused isotope in each section can be determined. The primary shortcoming of the radiotracer technique is the limitation created by the half-life of the tracer. For isotopes with short half-lives (e.g. - ^{31}Si $(t_{1/2}) = 2.6$ hrs) the duration and temperature range of the diffusion experiments may be limited, since adequate time must be allotted for the diffusion, sectioning, and activity measurement before the activity drops below detectable limits. Further limitations are related to the introduction of defects from the surface and the precautions needed during the handling of radioactive substances. By using layers of isotopically enriched material epitaxially grown on top of natural isotopic composition material, the diffusion of stable isotopes into the enriched layer can be observed, removing the restriction of the radioactive isotope tracer technique. The use of stable isotope structures for self-diffusion has been demonstrated to be a highly beneficial approach in other semiconductor materials systems such as Ge, GaP, GaAs, AlGaAs, and GaSb [Fuchs, 1995; Wang, 1997; Bracht, 1999a; 1999b; 2000; 2001b]. Isotope superlattices of natural and enriched Si will be used in the study of dopant and native defect interactions in Si.

Understanding the mechanisms of self-diffusion in SiGe has gained tremendous attention in recent years due to renewed interest in SiGe for device applications. In the constant effort to increase speed and performance of electronic devices while still reducing dimensions, the incorporation of SiGe alloys into current Si based devices is seen as the next step in improving device performance. Because SiGe is an alloy, its properties can be tailored to a specific application. The use of a thin layer of SiGe as the base layer in Si heterojunction bipolar transistors (HBTs) allows the base layer to be doped to higher densities, which reduces the resistivity of the base and reduces the RC time constant for switching. Due to the smaller bandgap of the SiGe base compared to Si, the gain of the HBT is increased as a result of reduced hole injection. The speed of the HBT can be increased by grading the Ge content in the SiGe base layer resulting in an electric field across the base, which accelerates the carriers. Another advantage of SiGe incorporation is the use of the difference in lattice constant between SiGe and Si to create strained Si within a CMOS device. By growing a Si layer on top of an epitaxial SiGe layer, the Si layer becomes strained in tension, resulting in an increased carrier mobility due to strain splitting of the conduction band, leading to reduced intervalley scattering of carriers. The enhanced mobility allows for device operation at the same speed, but at a lower voltage, which reduces the power consumption of the device. These advantages have led to an increase in the study of the atomic transport properties of the SiGe alloy system because incorporation into current Si devices requires a precise understanding of the behavior of the material during thermal processing. Any unwanted diffusion can alter the device dimensions and ruin device performance.

Previous efforts have concluded that self-diffusion in SiGe alloys occurs via interstitials on the Si rich side and via vacancies on the Ge rich side of SiGe composition [Strohm, 2001]. However, little conclusive evidence has been presented as to the cause of the transition, and the precise composition at which it occurs. In an effort to gain a better understanding of self-diffusion in SiGe, we have used stable isotope heterostructures to generate the first results on simultaneous Si and Ge self-diffusion in SiGe alloys.

A Brief History of Diffusion

The basis of our understanding of particle diffusion phenomena comes from the work of Adolf Fick and his experiments on the diffusion of salt in an aqueous solution. The results of the experiments led to his derivation of the equations of diffusion, now known as Fick's First and Second laws, respectively [Fick, 1855a,b]:

$$J = -D\nabla C \tag{1.1}$$

$$\frac{\partial C}{\partial t} = -D\nabla^2 C \tag{1.2}$$

where J is the flux of particles, C is the concentration of particles, and D is the diffusion coefficient or diffusivity. Equation 1.1 accurately describes the phenomenon of diffusion, where the flux of particles is proportional to the negative of the concentration gradient, with the constant of proportionality being the diffusion coefficient. Any observation of diffusion phenomena will reveal this relationship - particles move from areas of high concentration to areas of low concentration.

In Fick's experiments, he set up a system in steady state so as to make verification of his equations simpler in both an experimental and mathematical sense (dC/dt = 0).

This steady-state for the salt solution was achieved by filling a column with water and fixing the lower open end in immediate contact with solid salt. The column was placed in a large reservoir of pure water. In this manner the concentration at the lower end was completely saturated with salt and the upper end was constantly maintained at a salt concentration of zero by the reservoir of pure water. A steady-state concentration gradient was then established in the column by the diffusion of the salt from the fully saturated lower end to the zero concentration upper end of the column. The concentration of salt in solution at various points along the height of the column was determined by suspending a glass bulb from the beam of a balance and by placing counterweights to balance the beam. The specific gravity of the solution at the height of the bulb is determined by the amount of counterbalance needed. The specific gravity can be used as a measure of the concentration of the solution. In this manner, Fick was able to determine the concentration gradient of salt in the column of water, and verify the equations that he proposed.

In his paper of 1855, Fick states that in looking for a fundamental law of diffusion of a salt in solution, one should expect it to be identical to that of Fourier's equation for the diffusion of heat and Ohm's equation for the diffusion of electricity in a conductor. Indeed, Fick's Law as well as Ohm's Law for the flow of current, are both based on the equation for the conduction of heat first derived by Joseph Fourier in 1822 [Fourier, 1822]. Fourier was able to describe the conduction of heat through a bar using a differential equation of the form:

$$\frac{\partial T}{\partial t} = \frac{K}{\rho c} \nabla^2 T \qquad (1.3)$$

where T is given as the temperature, K is the thermal conductivity, ρ is the mass density of the solid, and c is the specific heat capacity.

Ohm's Law for the conduction of current, which he derived in 1827, is given by [Ohm, 1827]:

$$\frac{\partial U}{\partial t} = \frac{\chi}{\gamma} \nabla^2 U \tag{1.4}$$

where U is the electric potential, χ is the electrical conductivity and γ is the electrical capacitance. The electrical conductivity is the reciprocal of the electrical resistivity.

The analogy between Fourier's heat conduction equation and Fick's and Ohm's laws are evident by considering the similarities in Equations 1.2, 1.3, and 1.4. The partial differential with respect to time of concentration (Fick, Eq. 1.2), temperature (Fourier, Eq. 1.3), and electric potential (Ohm, Eq. 1.4) is equal to the Laplacian of concentration, temperature, and electrical conductivity, respectively; multiplied by a material parameter. This material parameter is the diffusivity, in the case of diffusion; the thermal conductivity divided by the mass density and specific heat, in the case of heat conduction; and the ratio of the electrical conductivity to the electrical capacitance in the case of electrical conduction. A more detailed analysis of the influence of Fourier's heat equation on the history of diffusion is given in the review article by T. N. Narasimhan [Narasimhan, 1999].

Even though Fick's experiments were performed on a liquid solution, the equations that he derived are the basis for studying mass transport in liquids, gases, and solids. One of the most fundamental contributions of Fick's work was the defining of the diffusion coefficient from his equations and his demonstration of how to find it experimentally.

7

The origins of experiments in solid-state diffusion can be traced back to the foundations of metallurgy and the formation of metal alloys. One of the earliest documented observations of diffusion in solids is attributed to Robert Boyle in 1684 [Barr, 1997]. Boyle reports the observation of the penetration of zinc into the face of a copper coin. By filing away the edge of the coin, the penetration of the zinc, and formation of brass, is evident. It is remarkable that a complete understanding of the inter-diffusion of copper and zinc would not be achieved until the work of E. O. Kirkendall in 1942 [Kirkendall, 1942]. The first definitive measurements of the diffusion coefficient for the diffusion of metals were made by William Roberts-Austen, [Roberts-Austen, 1896], who was Chemist and Assayer of the British Mint.

In a recent review of the history of diffusion [Barr, 1997], L. W. Barr attributes the beginning of the modern era of the study of diffusion in the solid-state to the year 1896. Three major milestones were achieved in that year, enabling the modern study of solid-state diffusion. The first was the publication of the work on metal diffusion of Roberts-Austen [Roberts-Austen, 1896], which demonstrated the ability to measure the diffusivity of metals by accurately controlling the temperature of diffusion, mechanical sectioning of the samples and then the determination of the concentration of the section by chemical assaying. This experimental approach of Roberts-Austen has been the foundation for most of the solid-state diffusion experiments of the 20th century. Although it was published in December of 1895, the influence of Roentgen's discovery of x-rays [Roentgen, 1895] on the scientific community was first felt in 1896, and helped to usher in the modern era of diffusion studies. Roentgen's work lead to the discovery of radioactivity in uranium salts by Becquerel [Becquerel, 1896], also in 1896. The

discovery of x-rays enabled the determination of the crystal structures of solids. The crystalline structure of solids has become a fundamental aspect in the modern understanding of solid-state diffusion mechanisms. Becquerel's discovery led to the pioneering work of Georg Hevesy, who first used radioactive isotopes as diffusion tracers [Groh, 1920]. Hevesy's work on the diffusion of radioactive lead isotopes in solid lead enabled the study of self-diffusion in solids [Groh, 1921; Hevesy, 1925]. Prior to the use of radiotracers, no suitable tracer was available to monitor the movements of self-atoms. With the study of self-diffusion came a much greater understanding of the process of diffusion in solids.

With the advances in the understanding of crystal structures from the use of x-rays and the knowledge gained from self-diffusion measurements, the investigation of how exactly the atoms moved through the solid during diffusion began in the early 1920's. The physical mechanisms of diffusion and the role of native defects in the diffusion process in solids were demonstrated during this period. One of the most important contributions to the understanding of diffusion in solids that was made in the 20th century was the discovery of the role of native defects in the diffusion process.

The fundamental work on the theory of diffusion mechanisms in solids was presented by Frenkel [Frenkel, 1926]. In this work he puts forth a model for the diffusion of atoms in a solid via the atoms vibrating about their equilibrium positions. When the atoms move too far from the equilibrium position, they exchange positions with neighboring vacancies in the lattice or possibly dissociate into an interstitial position leaving behind a vacant lattice site. He used Einstein's theory of Brownian motion [Einstein, 1905] to describe the 'random walk' motion of the atoms through the lattice.

While Frenkel's theory was the prevailing concept for the motion of atoms in a solid, it wasn't fully accepted until the experimental work of Kirkendall and his co-workers was presented in 1942 [Kirkendall, 1942; Smigelskas, 1947]. Kirkendall discovered that when diffusing pure copper into brass (60% Cu, 40% Zn), the original interface between the Cu and brass shifted inward toward the brass. Along with the diffusion coefficients that were calculated from his experiments, he concludes that there is an unequal binary diffusion occurring – Zn is diffusing more rapidly than Cu. Since the Zn is diffusing out of the brass faster than Cu can diffuse in, the interface shifts. The only mechanisms that could accurately account for the uneven diffusion fluxes demonstrated experimentally would be those that incorporated the diffusion of lattice vacancies to balance out the fluxes. With the experimental evidence of Kirkendall backing up the theory, the vacancy mechanism of Frenkel was accepted as the primary diffusion mechanism in metals, and the role of native lattice defects in the diffusion process was verified.

Frenkel's theory also accounts for the diffusion of atoms via an interstitial mechanism, which describes atomic movement through the interstices of the lattice. The first experimental evidence of an atom moving interstitially in a solid was presented in 1933 by the work of Seith and Kiel [Seith, 1933]. They performed experiments on Au diffusion in Pb and noted that the Au diffuses much faster in Pb than the Pb atoms themselves. Since the Pb diffusion was the same during self-diffusion as during the Au diffusion experiments, they concluded that the Au must be traveling through the interstitial sites and not exchanging with the Pb. Any place exchange of the Au with the Pb should result in enhanced Pb diffusion, but this was not observed.

A more detailed description of each of the currently accepted diffusion mechanisms will be presented in the following section.

1.2   Background

To begin the discussion of dopant and self-diffusion in Si as well as self-diffusion

in SiGe, a brief review of the fundamentals of solid-state diffusion is presented, along

with a more detailed description of self-diffusion in Si and SiGe. In addition, the current

understanding of dopant diffusion in Si will be established.

1.2.1   Diffusion in Solids

The diffusion of atoms in a solid is different from that of diffusion in a gaseous or

liquid state. In gases and liquids, the movement of the atoms can be seen as pure

"random walk" type diffusion, described accurately by Fick's Second Law (see Equation

1.2). However, for the diffusion of atoms in a solid the interaction of atoms with each

other during the diffusion process can not be neglected due to the rigid lattice of atoms

that define the solid.

There are six generally accepted mechanisms of atomic diffusion in a solid. The

mechanisms can be broken into two main types, direct and indirect. Indirect mechanisms

require the interaction of native defects in the diffusion process while the direct

mechanisms do not. A schematic diagram of the two direct diffusion mechanisms, pure

interstitial and direct exchange is presented in Figure 1.2.

The pure interstitial mechanism involves the movement of the diffusing species

through the interstitial spaces of the solid lattice without interacting with the

substitutional atoms. This mechanism can be easily described by the "random walk" diffusion represented by Fick's Second Law. Because the atoms move entirely within the interstices of the lattice, this type of diffusion is generally restricted to smaller atoms or ions, like H, Li, and O. The 3d transition metals in Si have also been found to diffuse via the pure interstitial mechanism [Weber, 1983]. Due to the small size of the atoms and the lack of interactions with the substitutional species, diffusion via the pure interstitial mechanism results in the highest diffusivities.

The direct exchange mechanism, also depicted in Figure 1.2, describes the movement of substitutional atoms onto neighboring lattice sites through a simple exchange of substitutional sites of either two atoms, or of four atoms in a "ring" mechanism. So far, this is a purely theoretical mechanism because the direct exchange has never been experimentally observed and the energies required for such a transition appear to be too high to make it physically plausible.

Pure interstitial   Direct exchange
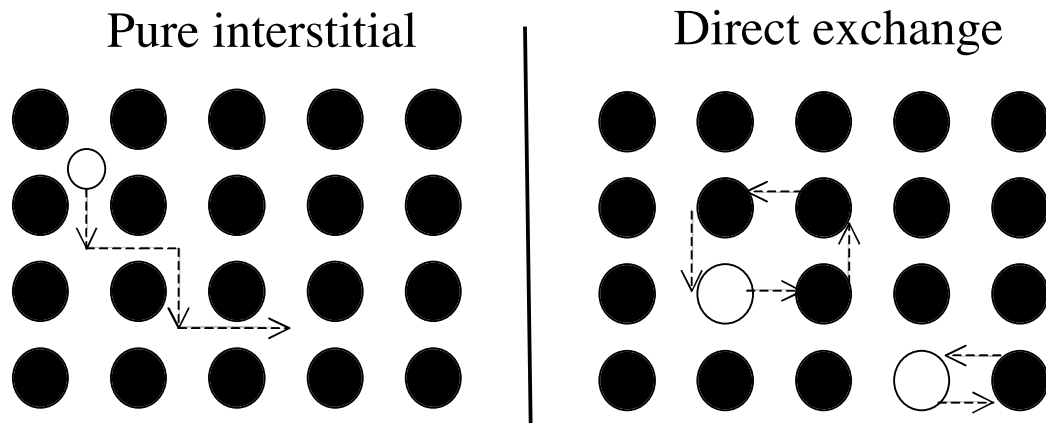
Figure 1.2 Schematic diagrams of the direct diffusion mechanisms in a solid, pure interstitial (left) and direct exchange (right). The black circles represent host atoms on the substitutional lattice; the white circles represent the diffusing species. Dashed arrows are used to indicate motion.

The indirect diffusion mechanisms can be separated based on the native defects that are involved. Therefore, there are two types of indirect diffusion mechanisms, interstitially assisted and vacancy assisted. Furthermore, there are two interstitially assisted diffusion mechanisms, the interstitialcy mechanism and the kick-out mechanism. Both of these mechanisms are represented schematically in Figure 1.3. The interstitialcy mechanism involves a two atom pair sharing a substitutional site, known as an interstitialcy. One atom from this pair can move to a neighboring lattice site occupied by a substitutional atom, forming a new interstitialcy pair while the remaining atom becomes fully substitutional. From this interaction the first atom has completed a diffusion step

Interstitialcy mechanism

$$A_s + I \quad \Leftrightarrow \quad AI$$

Kick-out mechanism

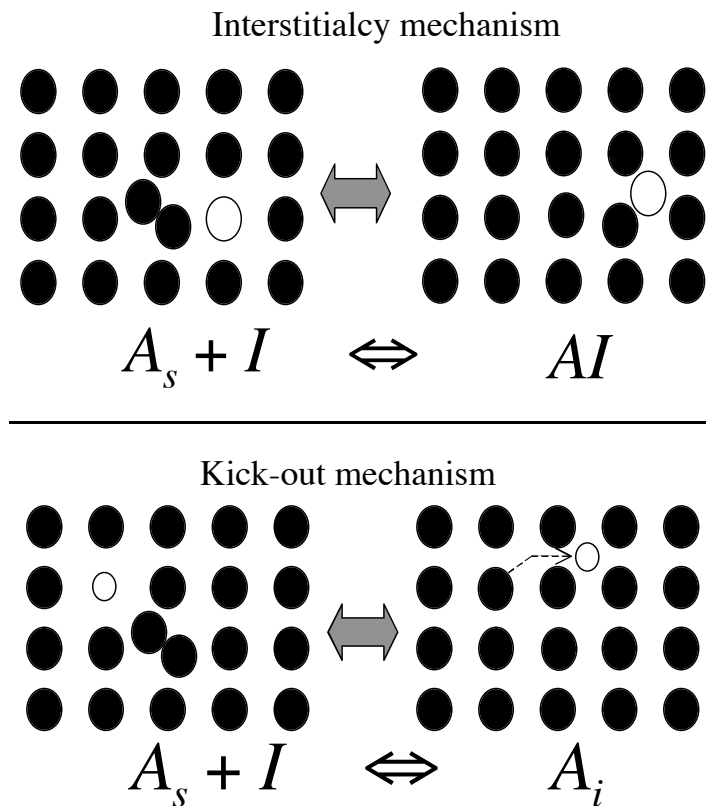$$A_s + I \quad \Leftrightarrow \quad A_i$$

Figure 1.3 Schematic diagrams of the interstitially assisted mechanisms, interstitialcy (top) and kick-out mechanism (bottom). The black circles represent substitutional and interstitial host atoms; the white circles represent tracers to observe diffusion. Dashed arrows are used to indicate motion.

and moved one lattice site. The atomic interaction of the interstitialcy mechanism can be described by the following reaction:

$$A_s + I \leftrightarrow AI \qquad (1.5)$$

where A represents the diffusing atom, I represents an interstitial atom, and the subscript s is used to denote a substitutional lattice site.

The kick-out mechanism, shown on the bottom of Figure 1.3, involves an interstitial host atom interacting with a substitutional diffusing species. When the host atom is in an interstitial position neighboring the substitutional diffusing species, it can "kick out" the diffusing atom from the substitutional site, occupying the substitutional site itself and leaving the diffusing species in an interstitial position. The diffusing species can then move through the interstitial positions of the lattice until it encounters another substitutional host atom that it may then "kick out", regaining a substitutional position and completing the diffusion step. The atomic interaction during the kick-out mechanism is described by the following reaction:

$$A_s + I \leftrightarrow A_i \qquad (1.6)$$

where A represents the diffusing atom, I represents an interstitial atom, the subscript s is used to denote a substitutional lattice site and the subscript i is used to denote an interstitial lattice site. By comparing Equations 1.5 and 1.6, it is evident that the reactions that occur in these two mechanisms are mathematically equivalent. The only difference is whether a pair is formed (interstitialcy) or a pure interstitial is formed (kick-out). In the kick-out mechanism, the atomic transport occurs while the diffusing species is in the pure interstitial lattice site, resulting in a larger distance traveled per diffusion step and a higher diffusivity than for the interstitialcy mechanism.

15

The two vacancy assisted mechanisms, shown in Figure 1.4, are the vacancy and dissociative mechanisms. The vacancy mechanism involves the interaction of the diffusing atom sitting on a substitutional site with a neighboring vacancy, or vacant lattice site. Since the neighboring site is vacant, the diffusing species can move into the vacant site leaving a vacancy in its previous substitutional position. However, due to the likelihood that the atom will simply reverse the step and return to the now vacant initial

Vacancy mechanism

$$A_s + V \quad \Leftrightarrow \quad AV$$

Dissociative mechanism

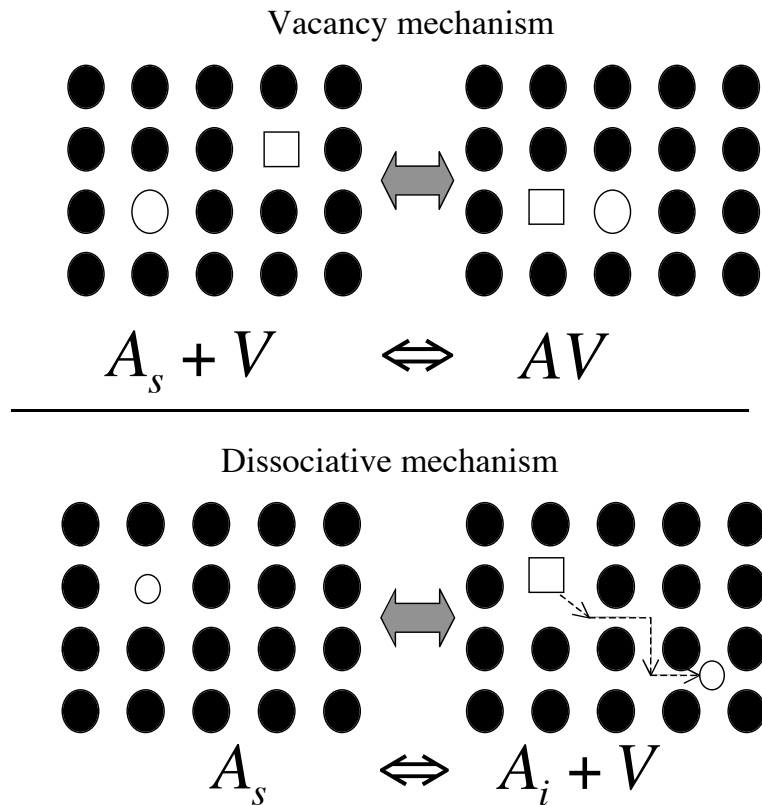$$A_s \quad \Leftrightarrow \quad A_i + V$$

Figure 1.4 Schematic diagram of the vacancy assisted mechanisms, vacancy (top) and dissociative mechanism (bottom). The black circles represent host atoms on the substitutional lattice, the white circles represent the diffusing species, and the white squares represent vacant lattice sites. Dashed arrows are used to indicate motion.

site, the diffusion step is not complete until the vacancy diffuses away a minimum of three nearest neighbors, and approaches via a different route. The reaction that describes the atomic interaction of the vacancy mechanism is given as:

$$A_s + V \leftrightarrow AV \tag{1.7}$$

where A represents the diffusing species, V represents a vacant lattice site, and the subscript s denotes a substitutional lattice position.

The dissociative mechanism, which is depicted schematically at the bottom of Figure 1.4, involves a substitutional atom that dissociates into an interstitial lattice position leaving behind a vacant lattice site. From this interstitial lattice position the diffusing atom is free to move as a pure interstitial until it encounters another lattice vacancy. Upon encountering the vacant lattice site, the interstitial atom can move into the substitutional site, annihilating the vacancy, and completing the diffusion step. As in the case of the kick-out mechanism, atoms diffusing via the dissociative mechanism move while in a pure interstitial position resulting in a larger distance traveled per diffusion step, when compared to the vacancy mechanism. The atomic interactions for the dissociative mechanism are described by the following reaction:

$$A_s \leftrightarrow A_i + V \tag{1.8}$$

where A represents the diffusing species, V represents a vacant lattice site, the subscript s denotes a substitutional lattice position, and the subscript i represents an interstitial lattice position.

<u>Thermodynamic Diffusion Parameters</u>

Diffusion in solids is a thermally activated process; therefore the temperature dependence of the diffusion coefficient can be described in the following form:

$$D = D_o e^{\left(-\frac{H^M}{k_B T}\right)} \qquad (1.9)$$

where D is the diffusion coefficient, H^M is the enthalpy of migration, k_B is Boltzmann's constant, and T is absolute temperature. D_o is a pre-exponential factor defined by the following equation:

$$D_o = g a^2 \nu_o e^{\left(\frac{S^M}{k_B}\right)} \qquad (1.10)$$

where g is a geometric factor, a is the lattice constant of the material, ν_o is the attempt frequency or jump frequency, and S^M is the entropy of migration. The jump frequency is the number of occurrences per unit time that an atom on a substitutional site attempts a jump over to a neighboring site. Therefore, the jump frequency is the vibrational frequency of the atom.

The ν_o term is responsible for the isotope effect in diffusion. The vibrational frequency for a single atom varies as $m^{-1/2}$ for a parabolic potential. The mass dependence of the change in vibrational frequency for two different isotopes is given by [Mullen, 1961; LeClaire, 1966]:

$$\frac{\nu^\alpha - \nu^\beta}{\nu^\beta} = \Delta K \left(\sqrt{\frac{m^\alpha}{m^\beta}} - 1 \right) \qquad (1.11)$$

where ν^α and ν^β are the vibrational frequencies of isotopes α and β with masses m^α and m^β, respectively. ΔK is the fraction of the translational kinetic energy of the isotope on

the substitutional site, given as a dimensionless quantity. The isotope effect is the change

in the diffusivity compared to the change in mass and is defined by [Mullen, 1961]:

$$E_B = \left(\frac{D^\alpha / D^\beta - 1}{\sqrt{m^\alpha / m^\beta} - 1} \right) \tag{1.12}$$

where E_B is the isotope effect, D^α and D^β are the diffusivities of α and β, respectively.

This isotope effect is generally small and therefore is neglected in diffusion studies where

tracers of different isotopic mass are used.

By inserting Equation 1.10 into Equation 1.9 the full description of the diffusion

coefficient can be obtained:

$$D = g a^2 \nu_o e^{\left(\frac{S^M}{k_B} \right)} e^{\left(-\frac{H^M}{k_B T} \right)} \tag{1.13}$$

Since the total free energy of migration, G^M, is given by:

$$G^M = H^M - T S^M \tag{1.14}$$

Equation 1.13 can also be written in a more concise form:

$$D = g a^2 \nu_o e^{\left(-\frac{G^M}{k_B T} \right)} \tag{1.15}$$

where both the entropy and enthalpy terms are included in the free energy. The diffusion

coefficient is most often described in a form similar to Equation 1.15, because only two

parameters, D_o (from Equation 1.10) and G^M, must be determined to fully describe the

temperature dependence of the diffusion coefficient.

The above derivation is for a concentration independent diffusion coefficient. For

the case of native defect assisted diffusion in semiconductors, i.e., for self-diffusion via

the vacancy or interstitialcy mechanism, the diffusion coefficient is dependent on the

19

concentration of native defects. The equilibrium concentration of native defects is thermally activated and is given in normalized form by:

$$\frac{C^{eq}}{C_o} = e^{\left(\frac{S^F}{k_B}\right)} e^{\left(-\frac{H^F}{k_B T}\right)}$$ (1.16)

where C^{eq} is the equilibrium native defect concentration normalized to atomic fraction by C_o, the atomic density. S^F is the entropy of formation and H^F is the enthalpy of formation for the defect.

The total thermal equilibrium self-diffusion coefficient is then given by:

$$D_{tot} = f \cdot \left(C^{eq}\big/ C_o\right) \cdot D$$ (1.17)

where C^{eq}/C_o is given by Equation 1.16, and D is given by Equation 1.13, and f is the correlation factor that accounts for the reversibility of the diffusion reaction. Both f and Equation 1.16 are unit-less, keeping the units of D_{tot} the proper units of diffusivity. Combining Equations 1.13 and 1.16 into Equation 1.17, the following description of the self-diffusion coefficient is obtained:

$$D^{SD} = f \cdot D_o e^{\left(\frac{S^{tot}}{k_B}\right)} e^{\left(-\frac{H^{tot}}{k_B T}\right)}$$ (1.19)

where $S^{SD} = S^F + S^M$ and $H^{SD} = H^F + H^M$. The superscript SD denotes self-diffusion. Using the definition for free energy as shown in Equation 1.14, Equation 1.19 can be placed in a simplified form similar to that of Equation 1.15:

$$D^{SD} = D_o e^{\left(-\frac{H^{SD}}{k_B T}\right)}$$ (1.20)

where $H^{SD} = H^F + H^M$ is the total activation energy for self-diffusion, and D_o now contains the correlation factor. The temperature dependence of the diffusion coefficient can be fully described with two parameters, D_o and H^{SD}.

As mentioned above, the correlation factor describes the probability that a diffusion step, after having occurred, will occur in the opposite direction resulting in no net movement of the diffusing species. The simplest illustration of this is the case of the vacancy diffusion mechanism. As depicted in the top portion of Figure 1.4, after an atom jumps into a neighboring vacancy, the probability that it will jump back into the vacancy it just created is accounted for by the correlation factor. In the case of self-diffusion this probability is determined entirely by the geometry of the system. The following relationship for the correlation factor, f, was derived [Compaan, 1956]:

$$f = \frac{1 + \overline{\cos\theta_{i,i+1}}}{1 - \overline{\cos\theta_{i,i+1}}} \tag{1.21}$$

where $\theta_{i,i+1}$ is the angle between successive jumps during diffusion. For a material with diamond cubic structure the angle between neighboring substitutional sites is 109.5 °, yielding a correlation factor from Equation 1.21 of $f = 0.5$ for diffusion via the vacancy mechanism [Compaan, 1956]. The correlation factor for diffusion via the interstitialcy mechanism in a diamond cubic crystal was calculated to be $f = 0.73$ [Compaan, 1958]. For uncorrelated diffusion, i.e., pure random walk, the correlation factor equals 1.

1.2.2 Self-Diffusion in Silicon and Silicon Germanium

This section offers a brief review of the current understanding of self-diffusion in Si and SiGe. It is intended to set a foundation for the research presented in the chapters to follow. For a more detailed review of diffusion in Si and Ge the reader is encouraged to examine any of the excellent review articles on the subject by [Seeger, 1968], [Frank, 1984], or [Fahey, 1989].

<u>Silicon Self-Diffusion</u>

Self-diffusion in silicon has been studied in detail since the 1960's, but it is only recently that definitive measurements of the Si self-diffusion coefficient have been made over a wide temperature range. The primary reason for the lack of consistent experimental results is the absence of a good tracer for monitoring self-diffusion. Much of the early work on Si self-diffusion relied on the radioactive tracer, ^{31}Si, [Peart, 1966; Masters, 1966; Fairfield, 1967]. Due to the restrictions caused by the short half-life of the radiotracer, ^{31}Si $t_{1/2} = 2.6$ hrs, these experiments were limited to high temperatures to achieve adequate penetration of a sufficient concentration of radiotracer isotopes in the short time frame. Mayer and his co-workers were able to extend the diffusion to lower temperatures by incorporating an ion beam sectioning technique into the analysis of ^{31}Si radiotracer diffusion [Mayer, 1977]. Another approach that was employed in an attempt to overcome the limitations caused by the short half-life of ^{31}Si was the use of the stable isotope ^{30}Si along with neutron activation analysis (NAA) [Ghoshtagore, 1966] or

^{30}Si(p,γ)^{31}Si resonance broadening [Hirvonen, 1979]. The stable isotope was diffused into the natural silicon from the surface for the appropriate time, and then neutron activation analysis or ^{30}Si(p,γ)^{31}Si resonance broadening was used to determine the ^{30}Si diffusion profile. These techniques overcame the limitations of the half-life of ^{31}Si during diffusion; however, the new techniques themselves were limited by the high background concentration of ^{30}Si (3.1%) present in natural Si.

A technique to overcome both the short half-life of ^{31}Si and the high background concentration of ^{30}Si (3.1%) in natural Si was not developed until sizable quantities of isotopically enriched ^{28}Si (99.95% ^{28}Si) became available. By growing an epitaxial layer of isotopically enriched ^{28}Si on top of a natural float zone (FZ) Si substrate via chemical vapor deposition (CVD), Bracht, et al., were able to observe diffusion of the ^{30}Si from the natural layer into the isotopically enriched ^{28}Si layer, depleted of ^{30}Si [Bracht, 1998]. The use of the stable isotope ^{30}Si as the diffusion tracer removed the restrictions of the half-life observed in earlier work and diffusion into an isotopically enriched ^{28}Si layer avoided the problem of high ^{30}Si background concentration.

The SIMS depth profile showing the initial ^{30}Si profile and two subsequent diffusion anneals at 1095 and 1153 °C is presented in Figure 1.5 [Bracht, 1998]. Best-fit analysis to the SIMS depth profile yielded a value for the Si self-diffusion coefficient at the given temperature. By annealing between 855 and 1388 °C, the diffusion coefficient was determined over a temperature range much wider than in previous experiments. The values for the diffusion coefficient determined by Bracht, et al., from the SIMS data are presented in Figure 1.6 in an Arrhenius plot, along with the
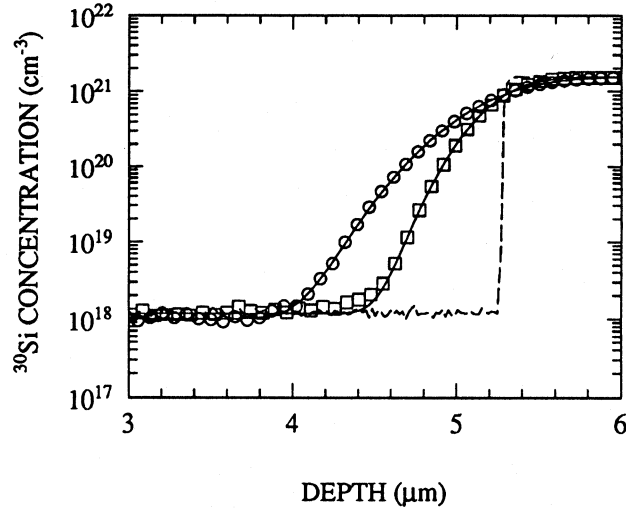
23

Figure 1.5 SIMS depth profile monitoring the ^{30}Si concentration in an epitaxially grown ^{28}Si isotopically enriched layer on top of a float zoned Si substrate of natural isotopic composition. Dashed line shows the as grown ^{30}Si profile. The squares are SIMS data after annealing at 1095 °C for 54.5 hrs, and the circles are the SIMS data after annealing at 1153 °C for 19.5 hrs. Solid lines are best fits to the data. [Bracht, 1998]

diffusion coefficient data of previous work, for comparison. The data generated from the diffusion experiments in the isotopically enriched structure are consistent over 7 orders of magnitude in diffusivity, spanning 500 °C, yielding a value for the temperature dependence of the Si self-diffusion coefficient of [Bracht, 1998]:

$$D_{Si}^{SD} = \left(530_{-170}^{+250}\right)\exp\left(-\frac{\left(4.75 \pm 0.04\right)eV}{k_B T}\right) \ \mathrm{cm^2 s^{-1}} \tag{1.22}$$

where D_{Si}^{SD} is the Si self-diffusion coefficient, k_B is Boltzmann's constant, and T is the absolute temperature in Kelvin. It should be noted that Equation 1.22 is given in the form of Equation 1.20, yielding a D_o value of 530_{-170}^{+250} cm^{2}s^{-1}, and an activation energy, Q, of 4.75 ± 0.04 eV. Equation 1.22 is the most consistent and widely accepted value of the Si self-diffusion coefficient.

24

Also shown in Figure 1.6 are lines representing the values for the diffusion coefficient determined by the experiments discussed earlier. The variation in values for the diffusion coefficient determined by the various researchers can be attributed in part to the limitations of the previous experimental techniques used.
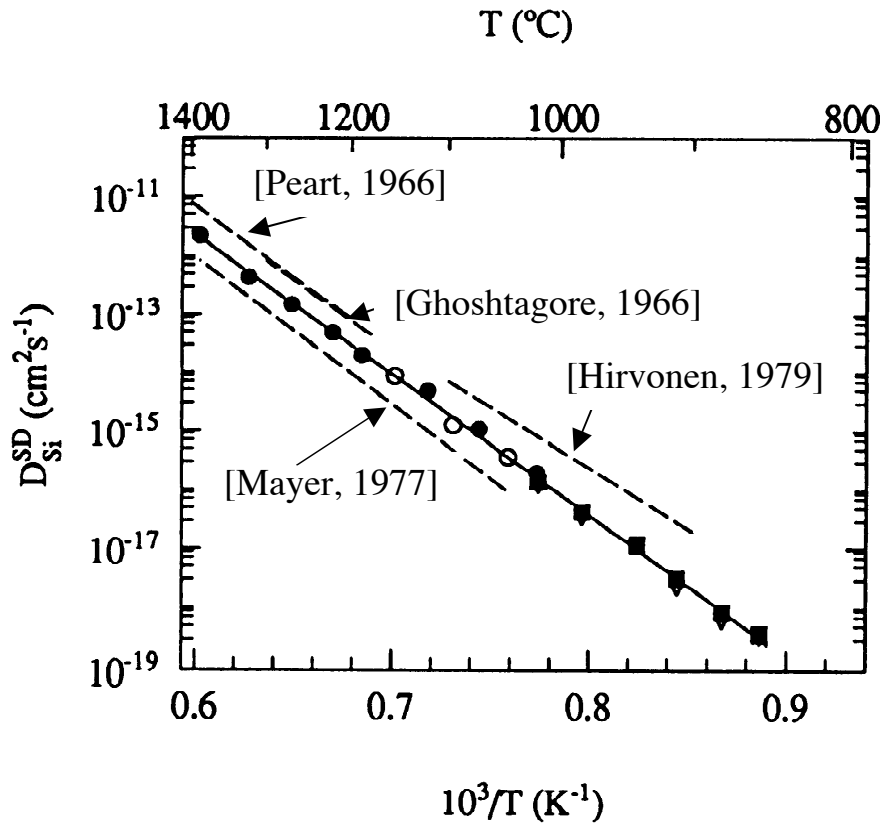

Figure 1.6 Arrhenius plot of the values for the Si self-diffusion coefficient from various authors. Symbols are data points from Bracht, et al., using an epitaxial layer of isotopically enriched ^{28}Si. [Taken from Bracht, 1998]

<u>SiGe Self-Diffusion</u>

Up to this point, there has been very little conclusive evidence as to the behavior of Si and Ge self-diffusion in SiGe alloys with varying compositions. Some of the earliest evidence of the composition dependence of the self-diffusion in SiGe was demonstrated by the work of McVay and DuCharme with their work in polycrystalline SiGe [McVay, 1974; 1975]. Due to the limitations of the half-life of the radiotracer ^{31}Si ($t_{1/2} = 2.6$ hrs), the authors pursued a more suitable tracer. Radioactive ^{71}Ge, with a longer half-life of 11.2 days, was used as a self-diffusion tracer in Si since Ge was shown to have a similar diffusion coefficient to Si in Si [McVay, 1973]. Figure 1.7 is a plot of the activation energy for ^{71}Ge diffusion in polycrystalline SiGe alloys of varying composition [McVay, 1975]. The activation energy drops from 4.65 eV in pure Si, to a composition independent value of 3.1 eV above 31% Ge. The value in pure Si is similar to that measured by Bracht, et al., (4.75 eV, [Bracht, 1998]). The value above 31% Ge matches the consensus value of ~3 eV for Ge diffusion in pure Ge found by various authors ([Seeger, 1968] and references therein; [Werner, 1985]). This transition from a Si self-diffusion activation energy at low Ge content, to a Ge self-diffusion activation energy above 31% Ge, was taken to indicate a shift in the diffusion mechanism from a Si-like interstitially assisted mechanism to a Ge-like vacancy assisted mechanism.

Other, more recent research into self-diffusion in SiGe has observed similar behavior. Ge diffusion in isotopically enriched SiGe layers showed a comparable change in the activation energy from 4.7 eV in pure Si to 3.2 eV at 50% Ge content [Zangenberg, 2001]. While the activation energies are similar to the work of McVay and DuCharme,
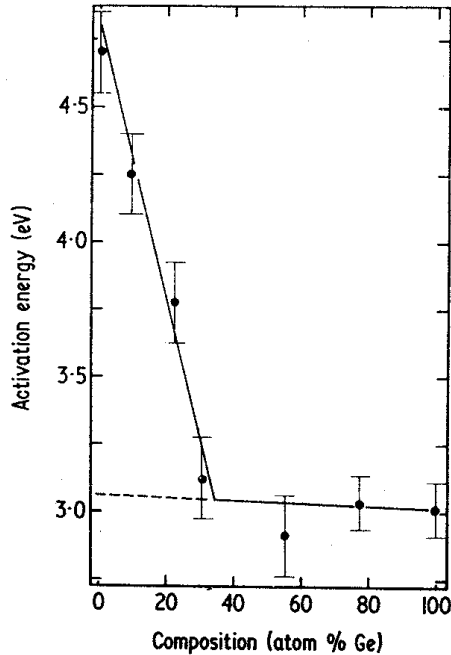
Figure 1.7 Plot of the activation energy of [71]Ge diffusion as a function of Ge content in polycrystalline SiGe samples ranging in composition from pure Si to pure Ge. [McVay, 1975]

the transition point to Ge-like diffusion is different (31% versus 50% Ge). Some of this variation in results can be attributed to the work of McVay and DuCharme being performed on polycrystalline samples, while Zangenberg, et al., used epitaxially grown thin films. Variation in the results on polycrystalline material may be due to enhanced Ge diffusion along the grain boundaries.

Additional recent work on the diffusion of radioactive [71]Ge into SiGe, demonstrated a change in the activation energy at 25% Ge [Strohm, 2001]. Figure 1.8 is a plot of the concentration dependence of the Ge diffusion coefficient at various temperatures, as a function of Si content, from the work of Strohm, et al. A change in the slope of the diffusion coefficient as a function of Si content is observed at 25% Ge.

27

Comparable to the conclusions drawn by McVay and DuCharme, Strohm, et al., assign

this change to a transition from interstitially assisted diffusion below 25% Ge and
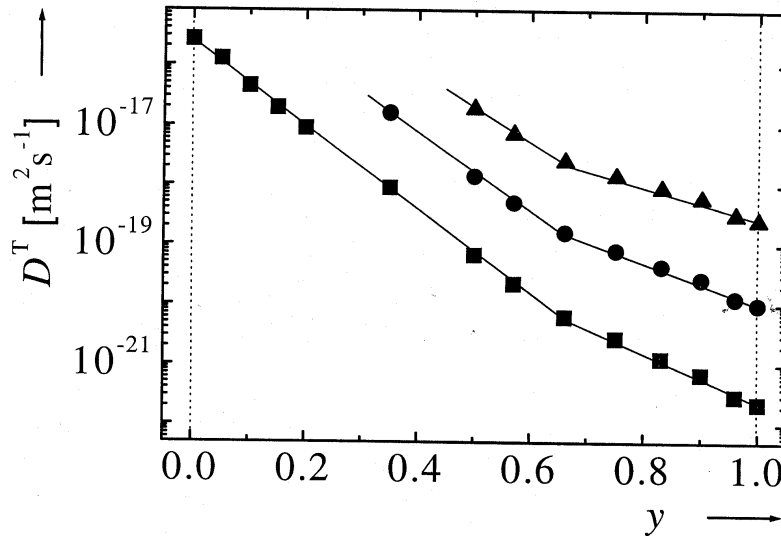
Figure 1.8 A plot of the diffusion coefficient of the radiotracer ^{71}Ge as a function of Si content at 1100 °C (triangles), 1000 °C (circles), and 900 °C (squares). Note the change in slope at 25% Ge. [Strohm, 2001]

vacancy assisted diffusion above 25% Ge.

While there appears to be a general consensus in the literature regarding a

transition in SiGe self-diffusion from a vacancy assisted mechanism at high Ge content to

an interstitially assisted mechanism at high Si content, there is still uncertainty

concerning the precise transition point, as well as the driving force behind the transition.

1.2.3   Dopant Diffusion in Silicon

As illustrated in Figure 1.9, dopants in Si have a wide range of diffusivities. For example, at 1000 °C, the various elements range in diffusivity between $\sim 10^{-4}$ cm^{2}s^{-1} for H to $\sim 10^{-16}$ cm^{2}s^{-1} for As. The reason for this 12 order of magnitude variation in diffusivity at 1000 °C is the different diffusion mechanisms by which the dopants traverse the lattice. For a review of the different diffusion mechanisms, see Section 1.2.1 and Figures 1.2-4.

The fastest diffusing elements, H, Cu, Ni and Fe, are shown in Figure 1.9 as short-dashed lines. These elements, along with Li (not shown in Figure 1.9), diffuse via the pure interstitial mechanism. Due to their small size and the weak interaction with the lattice, these elements are able to diffuse much faster than the other elements. The diffusivity of pure interstitially diffusing atoms is independent of the native defect concentration. It is interesting to observe that O is also listed as a pure interstitially diffusing species, yet it's diffusion coefficient is over six orders of magnitude lower than the other pure interstitial diffusing elements. This relatively low diffusivity is a result of the fact that oxygen is bound in a bond centered interstitial position, requiring the breaking of two bonds for oxygen to move from its position [Corbett, 1964; Watkins, 1982].

The elements that diffuse via the kick-out or dissociative mechanisms are known as the hybrid elements. They are called hybrid elements because they sit on substitutional sites but diffuse via interstitial sites. These elements, like Pt, Au, Zn, and
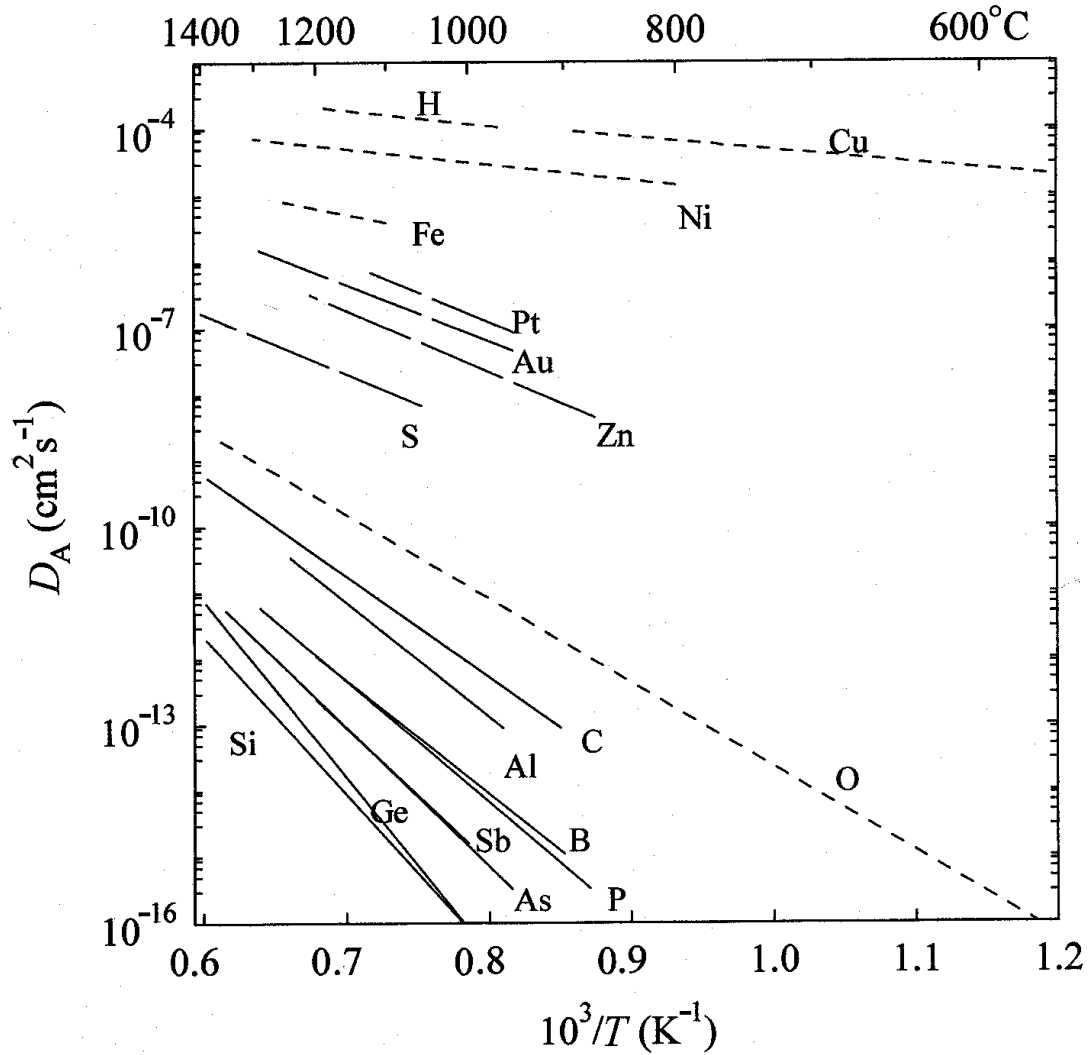
Figure 1.9 Temperature dependence of the diffusion coefficients of various elements in Si. Short dashed lines represent elements that diffuse via the pure interstitial mechanism. Long dashed lines represent hybrid diffusing elements. The solid lines represent the elements that diffuse via the substitutional mechanisms. [Taken from Bracht, 2001a; data from Stolwijk, 1998, and references therein].

S, are shown as the long-dashed lines in Figure 1.9. Similar to the pure interstitially diffusing elements, the hybrid elements diffuse rapidly, as a result of the diffusion via the interstitial sites. However, the diffusivity of the hybrid elements is several orders of magnitude lower than the pure interstitial diffusing elements because some fraction of

their time is spent immobile on substitutional sites, and they must overcome the formation enthalpy to become interstitial.

Elements that diffuse via the substitutional diffusion mechanisms (the vacancy and interstitialcy mechanisms) are much slower than either the pure interstitially diffusing elements or the hybrid diffusing species. These elements comprise most of the common dopants in Si as well as C, Ge, and Si self-diffusion (see Figure 1.9, solid lines). The lower diffusivity is due to the fact that the elements require the presence of native defects, self-interstitials or lattice vacancies, to assist the diffusion process, and unlike the other interstitial diffusing elements, they only move one lattice position per diffusion step. The elements that are smaller than Si, like B or P, are more likely to diffuse via interstitials, while the larger elements, like As or Sb, are more likely to incorporate vacancies in their diffusion due to lattice distortion.

Dopant diffusion via the vacancy and interstitialcy mechanisms is described by a diffusivity of the form of Equation 1.23, for equilibrium native defect concentrations and intrinsic free carrier concentrations.

$$D_A = D_{A_S}^{AV} + D_{A_S}^{AI} = \frac{C_{AV}^{eq} D_{AV}}{C_{A_S}^{eq}} + \frac{C_{AI}^{eq} D_{AI}}{C_{A_S}^{eq}} \qquad (1.23)$$

The total diffusivity of the dopant is represented by D_A in Equation 1.23, which can be written as the sum of the dopant diffusivity due to dopant-vacancy pairs (AV) via the vacancy mechanism, $D_{A_S}^{AV}$, and the dopant diffusivity due to dopant-interstitial pairs (AI) via the interstitialcy mechanism, $D_{A_S}^{AI}$. Each of these diffusivities can be expressed as the ratio of the transport coefficient ($C_{AV}^{eq} D_{AV}$ or $C_{AI}^{eq} D_{AI}$) to the equilibrium dopant concentration, $C_{A_S}^{eq}$. The transport coefficient is the product of the equilibrium defect pair

31

concentration, C_{AV}^{eq} or C_{AI}^{eq}, and the defect pair diffusivity, D^{AV} or D^{AI}. Equation 1.23

illustrates the dependence of the dopant diffusivity on both the dopant and native defect

concentrations under thermal equilibrium conditions.

1.3 Diffusion under Extrinsic Conditions

Up to this point, the discussion of the fundamentals of diffusion has been restricted to systems under intrinsic conditions, that is, either un-doped samples or samples with doping levels below that of the intrinsic free carrier concentration at the diffusion temperature. However, in the case where the sample is extrinsic at the diffusion temperature, the difference in the position of the Fermi level has a profound effect on the formation of charged point defects [Shockley, 1960]. This change in defect formation energy affects both the self- and dopant diffusion.

1.3.1 Fermi Level Effect

Native defects in semiconductors have the ability to capture excess electrons or emit electrons in the same manner as donor and acceptor impurity atoms. This gives rise to an acceptor- or donor-like energy level within the energy band gap for each of the possible charge states of the native defects [Shockley, 1957]. The experimentally determined charge-state energy levels for native defects in Si are presented in Figure 1.10. The four vacancy charge states were determined by electron paramagnetic resonance (EPR) studies at low temperature [Watkins, 1986]. The interstitial charge state was established by analyzing Au diffusion profiles in heavily boron doped Si [Bracht, 1997a; 1997b]. The active charge state for each energy level is determined by the position of the Fermi level. For the case where the Fermi level lies above a given energy

level, the defect exists in the charge state represented in the numerator. When the position of the Fermi level is below a certain energy level, the defect exists in the charge state designated by the symbol in the denominator.

Therefore, different charge states will exist for the native defects under n- and p-type extrinsic conditions. When silicon is doped heavily n-type, the Fermi level moves close to the conduction band edge. From Figure 1.10, it is evident that for a Fermi level position near the conduction band edge, the vacancy will exist in either a singly or doubly negatively charged state, while the interstitial will exist as a neutral defect. Since the ionized n-type dopant is positively charged, it is expected that the movement of the Fermi level would favor the generation of negatively charged native defects to balance the excess charge of the dopant ions. The vacancy obtaining a negative charge under n-type conditions illustrates this concept. At present there is no experimental evidence for the existence of a negatively charged interstitial defect, therefore, one would expect the interstitial to be neutral under n-type doping, as seen in Figure 1.10.
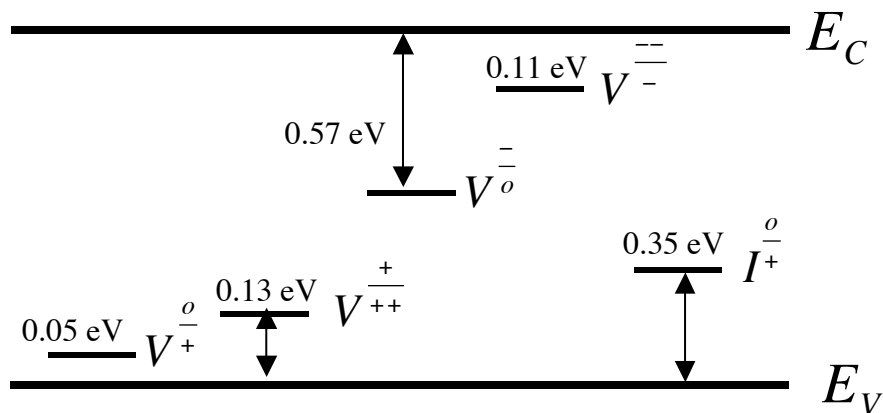

Figure 1.10 Schematic diagram of the known native defect charge states in Si, shown in reference to the conduction (E_C) and valence band (E_V) edges. [Vacancy states from Watkins, 1986; interstitial state from Bracht, 1997a; 1997b]

For heavily p-type doped Si, the Fermi level moves toward the valence band, and yields negatively charged ionized dopants. As seen in Figure 1.10, this results in the existence of positively charged interstitials and either neutral or positively charged vacancies, depending on the precise Fermi level position. As expected, the native defect charge states for p-type doping are exactly the opposite of the native defect charge states for n-type doping. A summary of the possible native defect charge states under extrinsic conditions is presented in Table 1.1.

The effect of the Fermi level shift under extrinsic conditions on diffusion in semiconductors can be seen by examining Figure 1.11. In an intrinsic semiconductor the Fermi level sits at approximately mid-gap. When the material becomes extrinsic, the Fermi level shifts towards the level of the dopant (towards the valence band in Figure 1.11). This shift in the Fermi level results in the interstitial becoming positively charged. It is the energy change, ΔE, of the Fermi level shift that becomes important for diffusion. Recall, from Equation 1.16, that the equilibrium concentration of a given defect is dependent on the formation enthalpy of that defect. The formation enthalpy for the positively charged self-interstitial, shown in Figure 1.11, is decreased by the amount ΔE, thereby increasing the equilibrium concentration of the defect, via Equation 1.16. (from

Table 1.1 Summary of possible native defect charge states under extrinsic conditions, based on energy levels depicted in Figure 1.10

	Dopant Charge State	Native Defect Charge state
Extrinsic n-type	D^+	I^o, V^-, V^{2-}
Extrinsic p-type	A^-	I^+, V^+, V^{2+}

[Shockley, 1957]) This increases the diffusivity of any species whose diffusion is

assisted by that defect (see Equation 1.17).

The Si diffusion research presented in this work will take advantage of the Fermi

level shift under extrinsic conditions and the subsequent alterations to the native defect

population to help discern which native defect charge states are involved in Si self-

diffusion as well as in the diffusion mechanisms of several dopants.

$$E_C$$

$$E_F^{int}$$

$$\Delta E \qquad \overline{} \quad I_+^{\,o}$$
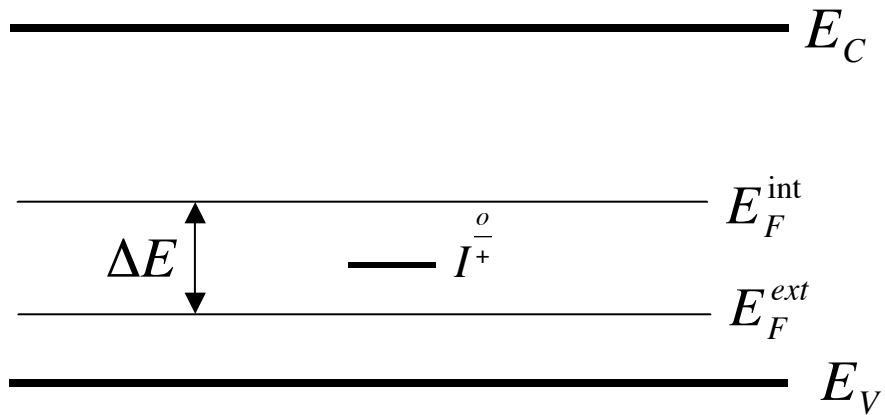
$$E_F^{ext}$$

$$E_V$$

Figure 1.11 Schematic diagram of the shift in the Fermi level under extrinsic p-type
conditions. ΔE represents the energy gained in comparison to intrinsic conditions. The
energy level for the positively charged interstitial is included as a reference point.

2   Simultaneous Dopant and Self-Diffusion

2.1   Experimental Approach

In order to observe the simultaneous self-diffusion of the host atoms and the diffusion of the dopant species, an experimental approach was required which involved a material structure that allowed for the monitoring of the simultaneous dopant and self-diffusion, a depth profiling technique with high mass and depth resolution, and a profile simulation approach that was able to determine the diffusion coefficients of multiple species simultaneously. The remaining sections of this chapter will detail how each of the experimental requirements described above has been met by the design of the current experimental approach.

2.1.1   Stable Isotope Heterostructures

A schematic of the material structure used to observe the simultaneous dopant and self-diffusion in silicon is presented in Figure 2.1. The design of this structure had several requirements in order to achieve the most useful experimental results. First and foremost, the structure was required to have alternating layers of natural and isotopically enriched Si, to facilitate the observation of self-diffusion between the interfaces of theses layers. Additionally, multiple sets of these layers were needed to monitor the changes in self-diffusion with variations in dopant concentration. The dopant concentration varies with depth according to the shape of the dopant diffusion profile. To achieve these

37

design requirements, five sets of alternating layers of natural Si (92.2% [28]Si, 4.7% [29]Si, 3.1% [30]Si) and isotopically enriched [28]Si (99.95% [28]Si) were grown via ultra high vacuum chemical vapor deposition (UHV-CVD) at Lawrence Semiconductor Research Laboratory (Tempe, AZ) on a (100) natural Si substrate. Each of the ten individual layers was grown to a thickness of 120 nm. Additionally, a 200 nm thick natural Si cap layer was grown on top of the isotope multilayer structure. Such thin layers were required to attain dopant diffusion through the entire structure at reasonable times and temperatures.

The second major requirement of the experimental diffusion structure was the introduction of dopants into the structure at high concentrations without altering the equilibrium conditions of the structure, specifically, the introduction of excess native
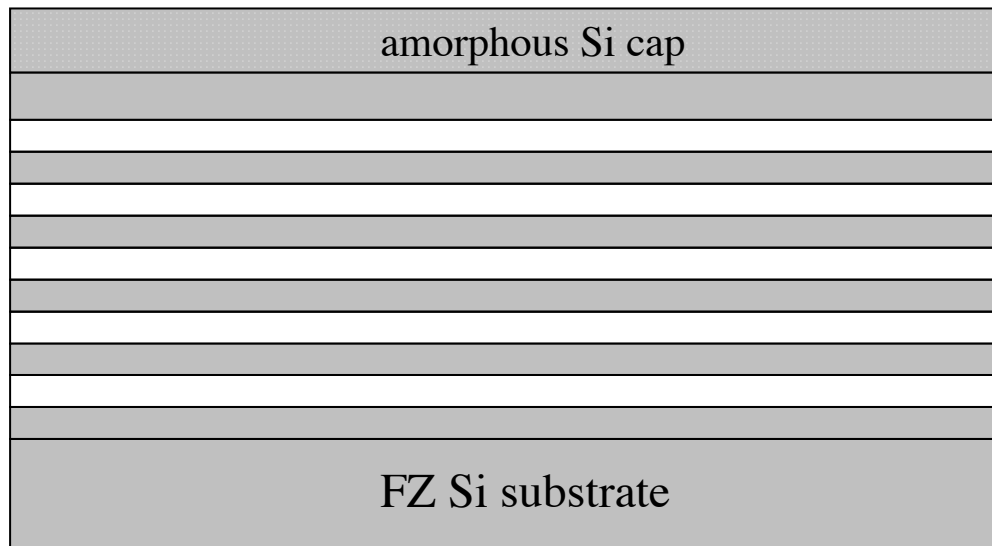

Figure 2.1 Schematic of Si isotope structure used for diffusion experiments. The isotopically enriched [28]Si layers are shown in white while the natural Si layers are gray. The layers of the multilayer structure are each 120 nm thick, while the crystalline Si cap is 200 nm thick and the amorphous Si cap is 250 nm thick.

defects. The presence of excess native defects has been shown to cause transient enhanced diffusion (TED) [Eaglesham, 1994]. The existence of TED in the structure during the diffusion experiments would create an additional level of complexity and inhibit the generation of a concise diffusion model, thus making the prevention of TED a necessity. To achieve this design constraint, a 250 nm thick amorphous natural Si layer was grown via molecular beam epitaxy (MBE) at the University of Aarhus, in Denmark, on top of the crystalline natural Si layer of the isotope structure. This layer could then be ion-implanted with the dopant to be studied to create the dopant diffusion source. Ion implantation allows for the introduction of a high concentration of dopants but also generates excess native defects due to the damage generated by the implanted ions. By implanting into an amorphous cap layer, it was expected that all implantation damage and excess defects would be restricted to the amorphous layer and prevented from translating over to the crystalline isotope structure.

The verification of this implantation damage and native defect isolation technique was achieved by implanting a set of the diffusion structures with Si ions at a dose of 7×10^{15} cm^{-2} at 50 keV and 1×10^{16} cm^{-2} at 65 keV and carrying out a series of diffusion experiments between 900 and 1050 °C. Since Si implantation into Si should have no other effect than generating excess defects due to implantation damage, the diffusion profiles should be precisely those that one would expect from intrinsic Si self-diffusion. Any deviation from intrinsic diffusion would be evidence of transient enhanced diffusion caused by the excess native defects entering the crystalline structure.

Figure 2.2(a) shows the SIMS depth profile from a sample annealed at 1000 °C for 5 hours after Si implantation into the amorphous cap layer. Also plotted in Figure

39

2.2(a) is the ZOMBIE simulation (see Section 2.1.3) for intrinsic Si at 1000 °C. The

close agreement between the simulation and SIMS data is illustrated in Figure 2.2(b),

which is an Arrhenius plot of the diffusion coefficient determined from fitting the SIMS

data. Also included in the plot is a line indicating the temperature dependence of the Si

diffusion coefficient under intrinsic conditions taken from literature [Bracht, 1998]. The

lack of any deviation from the intrinsic diffusion coefficient after Si implantation, as

evident in Figure 2.2, confirms the initial supposition that the amorphous cap layer

prevents the transfer of implantation damage and excess native defects to the crystalline

layers and therefore suppresses TED.
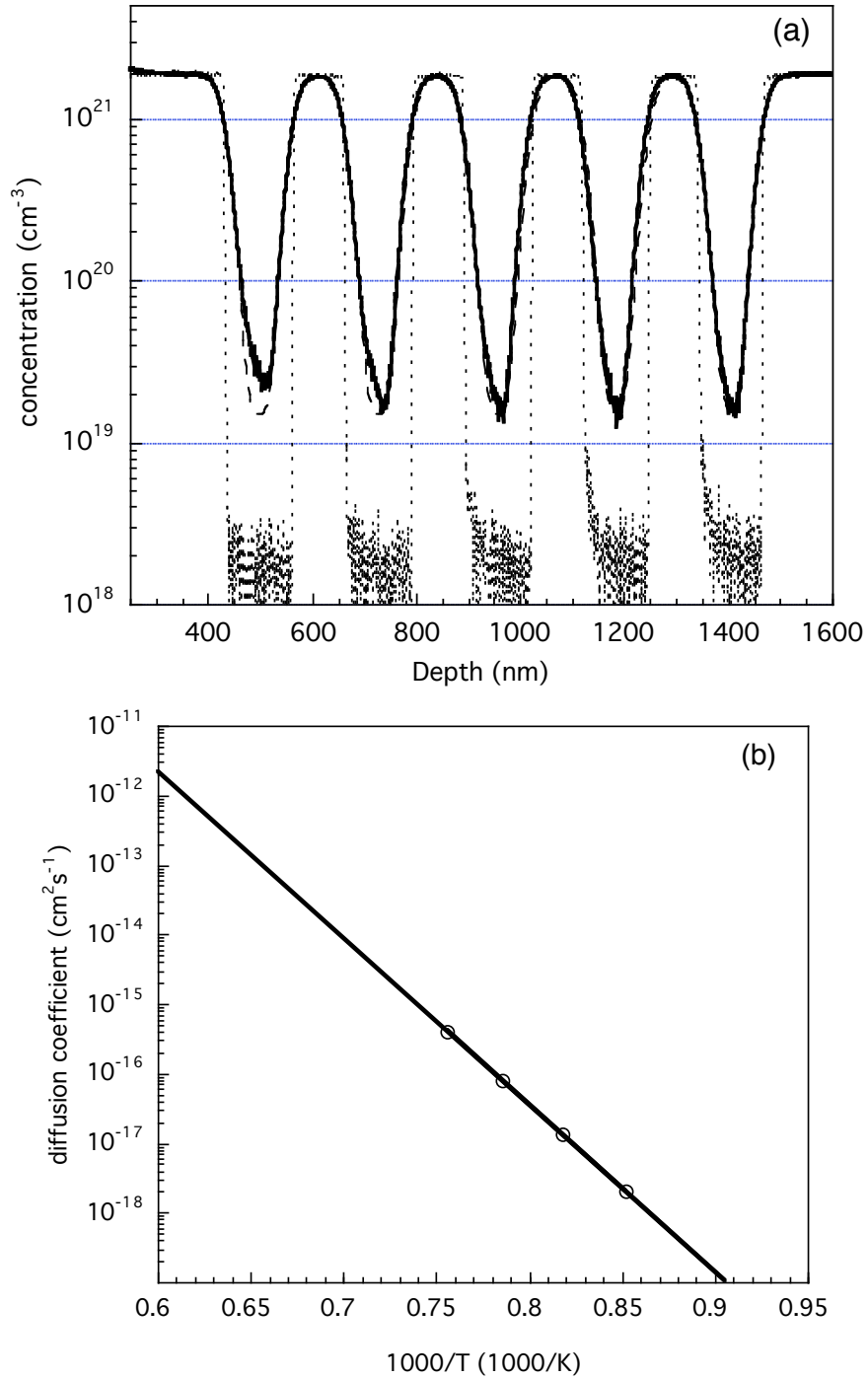
Figure 2.2 a) SIMS depth profile of ^{28}Si enriched isotope heterostructure before annealing (dotted line) and after Si implantation into the amorphous cap layer and annealing at 1000 °C for 5 hours (solid line), and ZOMBIE simulation for intrinsic diffusion (dashed line). The discrepancy between the simulation and SIMS result in the near surface region is attributed to "knock-on" during SIMS analysis. b) Arrhenius plot of the Si diffusion coefficient determined from Profile (see Section 2.1.3) best fit analysis to the SIMS data (open circles). Solid line is the intrinsic Si diffusion coefficient from literature [Bracht, 1998].

2.1.2   Secondary Ion Mass Spectrometry

Secondary Ion Mass Spectrometry (SIMS) was chosen as the analytical technique for generating the depth profiles in the diffusion samples. The primary motivation for the use of SIMS over other depth profiling techniques was the high depth resolution derived from the ion beam used for sectioning. As illustrated in Figure 2.1, the alternating layers of natural and isotopically enriched ^{28}Si in the isotope heterostructure are only 120 nm thick. The high depth resolution required to fully resolve the diffusion profile in a 120 nm thick layer removes from consideration the depth profiling techniques used in previous diffusion experiments such as mechanical [Peart, 1966] or chemical sectioning [Fairfield, 1967; Ghoshtagore, 1966]. The goal of the research is to observe simultaneous diffusion of ^{30}Si self-atoms and the dopant atoms, therefore the depth profiling technique must also be capable of high mass resolution and simultaneous analysis of several species. The high mass resolution is required to distinguish the ^{30}Si not only from the dopant species, but from the other stable Si isotopes present, ^{28}Si and ^{29}Si. The simultaneous analysis of multiple species is necessary to produce diffusion profiles of both ^{30}Si and the dopant species. An additional advantage of SIMS is the wide dynamic range over which it can measure ion concentrations. Depending on the species of interest and the instrumentation of the SIMS, the technique is capable of measuring from 10^{15} to 10^{22} atoms/cm^3.

This section will detail the fundamental aspects of the SIMS depth profiling technique, specifically describing the advantageous features mentioned above. A more

thorough discussion of the technique and its application to the experiments performed here is presented in Appendix A.

Figure 2.3 is a schematic representation of the fundamental components of the SIMS analytical tool. The ion species used to sputter the sample surface is generated in the ion gun. In general a highly reactive and electronegative species like O_2^+ or Cs^+ is chosen to generate a high ion yield from the sample. The ion beam is directed onto the sample by means of an accelerating voltage applied between the sample and source. The sample is held at ground potential, while the source is held at several kV. When the several kV ion beam strikes the sample surface the cascade of collisions caused by the incident ions results in the emission of low energy (~10 eV) secondary elemental and molecular ions from the sample. These secondary ions are directed into a mass spectrometer, where all but the desired mass species is filtered out. The ions passing the mass filter are sent into an ion detector for counting, as illustrated in Figure 2.3. The mass spectrometer is commonly either a bending magnet, or a quadrupole mass spectrometer (see Figure 2.5).

Plotting ion counts measured at the ion detector versus time generates the depth profile. In order to create a more useful profile, plotted in units of concentration and depth, the ion counts are converted into concentrations based on the ion yield measured from a calibrated standard. The time is converted into depth units by measuring the crater depth at the end of the measurement and dividing the crater depth by the total time of the SIMS measurement to obtain a sputter rate. This sputter rate is then used to convert the time data to units of depth. The assumption is made that the sputtering rate during the whole run remains constant. This is an accurate assumption for most

homogenous materials, the exception being those materials systems such as mixed phase

materials and heterostructures of differing matrix elements. A depth profile measured

using SIMS is presented in Figure 2.4. The figure shows a concentration versus depth

plot of the Si isotope heterostructure (seen schematically in Figure 2.1) after As

implantation into the amorphous cap layer.

Depending on the ion species and the sputtering rate, the lower detection limit of

SIMS lies between 10^{12} and 10^{16} atoms/cm^3 and the maximum depth resolution is

between 2 and 30 nm [Brundle, 1992]. The depth resolution is highly dependent on the

incident ion beam energy. The higher the ion beam energy, the more damage is created

on impact and the worse is the depth resolution.
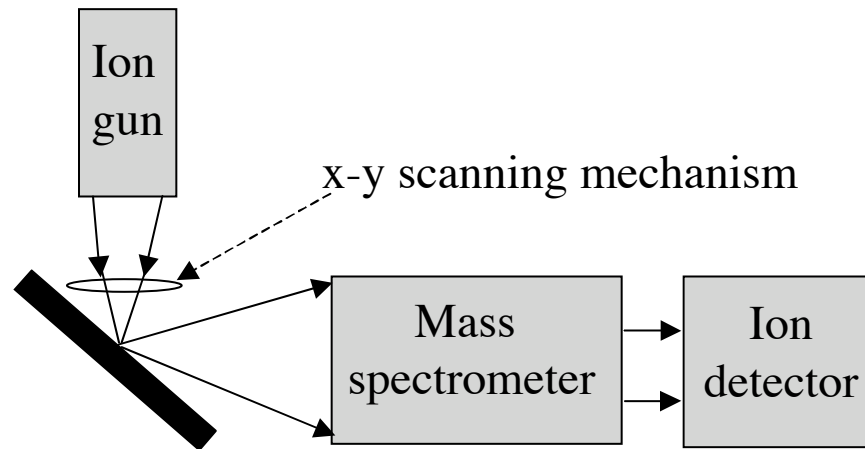
Figure 2.3 Schematic diagram of the fundamental components of a Secondary Ion Mass
Spectrometer. The ions are generated in the ion gun, incident on the sample (black). The
secondary ions are directed into the mass spectrometer where they are filtered, and the
selected ion is sent to the ion detector for counting.
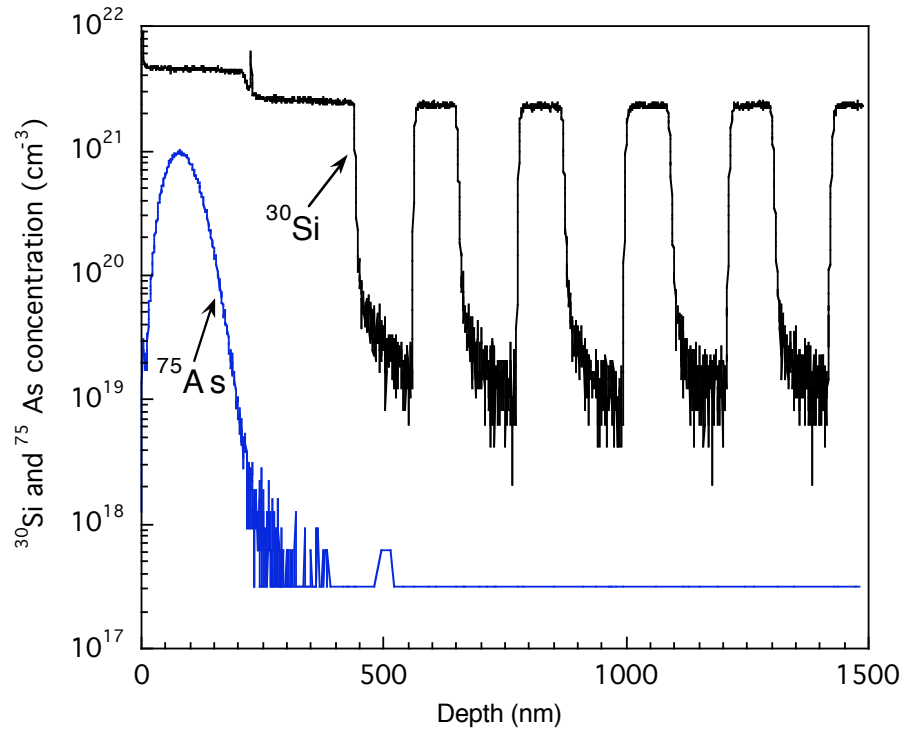
Figure 2.4 SIMS depth profile of Si isotope heterostructure (see section 2.1.1) after As implantation into the amorphous cap layer. Profiles of ^{75}As and ^{30}Si were measured simultaneously. The decrease in ^{30}Si concentration at 250 nm is a result of the change in ion yield between the amorphous Si cap layer and the crystalline Si. The spike in ^{30}Si seen at the a-Si/c-Si interface is due to increased ion yield caused by oxygen at the interface.

A quadrupole mass spectrometer was used for the experiments presented in this work because it allows rapid switching between several selected masses, enabling the simultaneous analysis of multiple species discussed above. As shown on the right side in Figure 2.5, the quadrupole mass spectrometer consists of 4 symmetric rods, with one pair of rods fixed perpendicular to the other pair of rods. Each pair of rods is held at a d.c. voltage with a radio frequency (rf) a.c. voltage superimposed on it. One pair is maintained at a positive d.c. voltage and the other pair is kept at a negative d.c. voltage. The rf voltage on the two pairs of rods are 180 degrees out of phase with one another. As

45

the ion passes down the center of the filter axis, it undergoes oscillations due to the varying rf field. Selection of the proper rf to d.c. voltage ratio results in the ions of the desired mass passing through the instrument un-deflected while ions of all other masses are scattered into the rods (see left side of Figure 2.5). All ions that are below the selected mass are scattered into the positive pair of rods, while all ions above the selected mass are neutralized on the negative pair of rods. Mass selection is dependent only on the voltages applied to the rods; therefore rapid switching between different masses is readily achieved. Mass selection obtained from a magnetic sector spectrometer requires changing the magnetic field for different mass ions. Much larger energies and larger time constants are needed to achieve mass switching than for a quadrupole mass spectrometer.

SIMS using a quadrupole mass spectrometer is the ideal depth profiling technique for thin films like those in the isotope heterostructures used for the current diffusion experiments. Depth resolution of a few nanometers is achievable with high mass resolution and rapid switching of mass selection for the monitoring of several ions simultaneously.
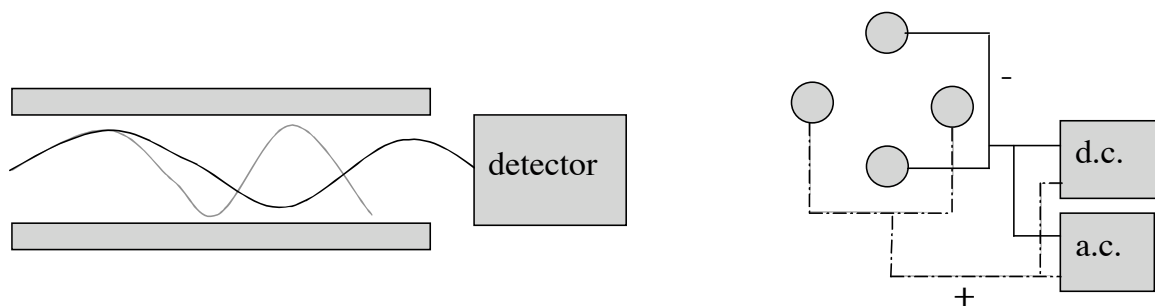
Figure 2.5 Schematic diagram of a quadrupole mass spectrometer (left) showing the path of an ion of the selected mass (black line) and a scattered ion (gray line). Right side shows a diagram of the voltages applied to the four rods.

2.1.3   Modeling and Simulation

In this section the procedure that is used to generate a diffusion model and compare this model to empirical data via computer simulations is described. The modeling and simulation procedures presented are described in greater detail in Appendix B. The approach used is similar to the integrated diffusion model developed by Uematsu [Uematsu, 1997].

In order to determine the appropriate physical model for diffusion under a given set of conditions, the first step is to propose a theoretical model based on the previous work done in the field as well as to gather any information that can be gained from a qualitative review of the experimental diffusion profiles. The second step is to generate a computer simulation of the diffusion using conditions that match the experimental conditions. The appropriate nature of the model is determined in step three when the simulated diffusion profile is recursively compared to the experimental profile until a best fit is achieved. The diffusion coefficient for the species of interest is the fitting parameter in the best-fit analysis.

The model for simultaneous dopant and self-diffusion is based on the diffusion mechanisms by which the species of interest move through the lattice. Si self-diffusion is known to be mediated by both interstitials and vacancies via the interstitialcy and vacancy mechanisms. The diffusion mechanism of the dopant species will vary (see Section 1.2.3). Previous experimental work often yields valuable insight into the appropriate mechanism. For example, in the case of As diffusion, previous work [Fahey,

1989] demonstrated that As diffusion in Si is enhanced when diffusion coincides with oxidation (interstitial injection) or nitridation (vacancy injection) of the sample surface. This is an indication that As diffuses via both interstitials and vacancies. What then remains to be determined in the case of native defect assisted diffusion of dopants is which mode of diffusion is most appropriate, the foreign atom controlled mode of the substitutional pair mechanisms (interstitialcy and vacancy) or the native defect controlled mode of the hybrid mechanisms (kick-out and dissociative). Often several mechanisms must be developed through the whole simulation process and fit to the data to determine the proper choice. Once the appropriate mechanisms are chosen, equations of the form of Equations 1.5 – 1.8 are developed for each diffusing species, i.e., – dopant atom, dopant-defect pair, and Si self-diffusion via vacancy and interstitialcy mechanism.

A one-dimensional equation for Fick's Second Law (see Equation 1.2) is created for each diffusing species. However, as discussed in Section 1.2.3, the hybrid and substitutional mechanisms used by most dopants are not governed by pure random walk diffusion described by Fick's Second Law. Since the atoms spend some fraction of their time on immobile substitutional sites, this must be accounted for in the diffusion equations. As an example, if a dopant atom diffused via the vacancy mechanism defined by Equation 1.7:

$$A_s + V \leftrightarrow AV$$

the Fick's Law diffusion equation must be modified to account for the reaction going forward (creating mobile dopant-defect pairs) and the reverse reaction (the annihilation of mobile pairs). Equation 1.2 for the diffusion of the dopant defect pair, AV, would then be written in one dimension as:

$$\frac{\partial C_{AV}}{\partial t} = \frac{\partial}{\partial x}\left(D_{AV}\left[\frac{\partial C_{AV}}{\partial x}\right]\right) - k_r[AV] + k_f[A_S][V] \qquad (2.1)$$

where C_{AV} and D_{AV} are the concentration and diffusion coefficient of dopant defect pairs, respectively. The forward and reverse reaction rates are represented by k_r and k_f, while [AV], [A_S], and [V] are the concentrations of the dopant-defect pairs, the substitutional dopant atoms, and the vacancies, respectively.

Once a differential equation of the form of Equation 2.1 is generated for each diffusing species in the system under investigation, the model, consisting of the whole set of differential equations along with the appropriate boundary and initial conditions, is input into the partial differential equation solver ZOMBIE [Jüngling, 1985]. Values for the time and temperature corresponding to the experimental data are input into the program as well as approximate values for the diffusion coefficients for each diffusing species. A set of initial simulations is performed and compared qualitatively with the SIMS depth profiles to insure the appropriate model and parameters are being used. This is the second major step in the simulation and modeling process.

The final step in the process involves the use of a best-fit routine to extract the diffusion coefficients from the experimental data. Once the initial simulations give a reasonably accurate match to the experimental data, the mathematical equation solver Profile [Ouwerling, 1989] is used to obtain a best fit. A subroutine for the Profile program runs the ZOMBIE simulation for a set of initial parameters including the diffusion coefficients for each diffusing species. The simulation result is then compared to the experimental SIMS results by the Profile program using the Modified Damped Least Squares non-linear parameter optimization technique. This is an improved variation on the Levenberg-Marquart (lev-mar) method. A new set of diffusion

49

coefficients (the fitting parameters) is generated, which is then re-input into the ZOMBIE program and another simulation is run using the new diffusion coefficients. The new ZOMBIE simulation data is again compared to the experimental SIMS data using the Levenberg-Marquart routine of Profile, and the process is repeated until a best fit is achieved. The diffusion coefficients determined by the best-fit ZOMBIE simulation are then considered to be the values that match the experimental data. By obtaining a best fit of the experimental data, not only are the values of the diffusion coefficient found, but also the suitability of the model chosen in the initial phase of the process is verified. It is in this manner that a physical model and the parameters for diffusion are extracted from the experimental data.

While with the use of a sufficient number of equations and variable parameters a model, that is not unique can be found to fit any diffusion profile, an effort is made during modeling to ensure that the proposed model is consistent with previous experiments and literature. The equations chosen for the model are derived from the diffusion mechanism reactions, and only the minimum number of equations is used to reduce the number of variables. The input values of the variables are chosen to be consistent with previous experimental results and literature values to generate a reasonable and overall consistent model.

3 Dopant and Self-Diffusion Experiments in Silicon

3.1 Diffusion of Boron in Silicon under Extrinsic Conditions

3.1.1 Introduction

Boron was chosen as a dopant for the diffusion experiments in Si because it is known to diffuse primarily via interstitials [Mizuo, 1981]. With the implantation of a high concentration of boron, significant parts of the Si isotope multilayer structure will become p-type and remain extrinsic during diffusion. The concentration of positively charged native defects will be enhanced, altering the boron and Si self-diffusion (see section 1.3.1). We expect that extrinsic boron diffusion experiments into the Si isotope heterostructure should yield information on the role of the positively charged interstitial in both boron and self-diffusion.

Boron was implanted into the amorphous cap layer on top of the Si isotope heterostructure (see section 2.1.1) at a dose of 7×10^{15} cm^{-2} at 32 keV and 1×10^{16} cm^{-2} at 37 keV. Implantation into the amorphous cap layer is performed to prevent the introduction of excess native defects generated by implantation damage into the crystalline isotope structure. A discussion of the necessity for prevention of excess native defect injection and the effectiveness of the amorphous cap layer approach is presented in section 2.1.1 and Figure 2.2.

Figure 3.1(a) shows a SIMS depth profile of the implanted multilayer structure prior to annealing. The implanted sample was diced into 4×4 mm^2 samples for annealing

51

and cleaned in heated xylenes and acetone and room temperature methanol. Oxide was removed from the sample surfaces with a 30 second etch in concentrated HF. Silica ampoules were etched for 5 minutes in 5% HF. The samples were placed in the ampoules and evacuated to a base pressure of $1\text{-}2\times10^{-5}$ Torr. The ampoules were backfilled with Ar to approximately 180 Torr to obtain good thermal transport. Samples were annealed for various times at temperatures between 845 °C and 1098 °C in a Lindberg/Blue resistance-heated tube furnace for appropriate times and temperatures. A type-S, Pt-Rh, thermocouple was used to monitor the temperature. The error in the temperature measurement is considered to be ± 2 Kelvin.

Concentration versus depth data were simultaneously collected for ^{30}Si, ^{28}Si, and ^{11}B using a 1 keV oxygen beam on an ATOMIKA 4500 SIMS instrument at Accurel Systems (Sunnyvale, CA). The differential equations governing diffusion in this system were solved using a specially adapted version of the partial differential equation solver ZOMBIE [Jüngling, 1985] as described in section 2.1.3 and Appendix B.

3.1.2 Experimental Approach and Results

Two interstitial-mediated diffusion mechanisms, the kick-out mechanism [Cowern, 1999] (Equation 3.1) and the interstitialcy mechanism [Sadigh, 1999; Windl, 1999] (Equation 3.2) have been proposed for B diffusion in Si:

$$B_i \leftrightarrow B_s + I \tag{3.1}$$

$$[BI] \leftrightarrow B_s + I \tag{3.2}$$

where the subscripts *s* and *i* refer to substitutional and interstitial boron, respectively, and *I* refers to self-interstitial atoms. Additional equations for both of these general mechanisms exist which take into account defect charge states mediating self- and dopant diffusion.

A variety of simulations were conducted for various combinations of defect charge states and reaction mechanisms. Figure 3.1(b) shows the ^{30}Si and ^{11}B SIMS concentration profiles along with ZOMBIE simulated diffusion profiles for the two species. The simulation results revealed self- and dopant diffusion to be mediated by neutral and singly positively charged self-interstitials, via the mechanisms given by Eqs. 3.3 and 3.4:

$$B_i^0 \leftrightarrow B_s^- + I^0 + h \tag{3.3}$$

$$B_i^0 \leftrightarrow B_s^- + I^+ \tag{3.4}$$

where the superscripts represent the charge states of the given defect and h represents a positively charged hole required for charge neutrality.

No significant contribution to Si and B diffusion from vacancies (*V*) was observed. This is a consequence of the B diffusion process, which creates a supersaturation of self-interstitials resulting in an undersaturation of vacancies. Accordingly, the contribution of vacancies to Si and B diffusion is suppressed. This effect of the B diffusion is seen in the simulation results of Figure 3.2. The interstitial concentration is above its equilibrium value throughout the sample while the vacancy concentration is held below its equilibrium value.
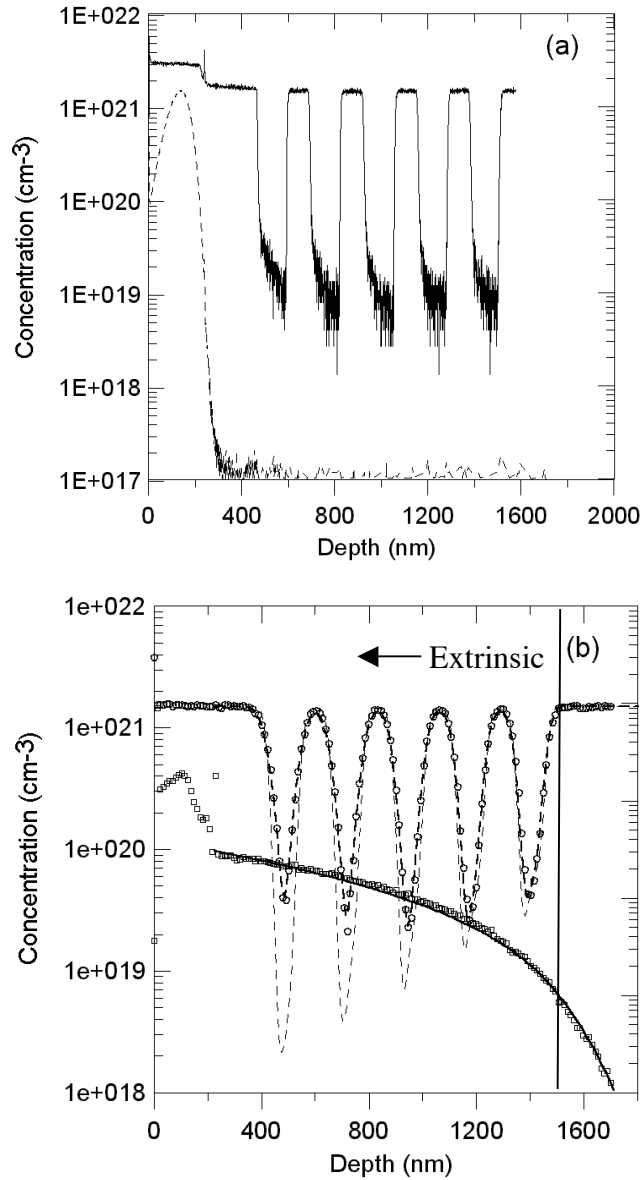
Figure 3.1 (a) SIMS ^{30}Si (solid line) and ^{11}B (dashed line) profiles of a B implanted Si isotope multilayer structure prior to annealing. The decrease in ^{30}Si concentration at 250 nm is a result of the change in ion yield between the amorphous Si cap layer and the crystalline Si. The spike in ^{30}Si seen at the a-Si/c-Si interface is due to increased ion yield caused by oxygen at the interface. (b) SIMS ^{30}Si (○) and B (▫) profiles after annealing for 4 hours 55 minutes at 1000 °C. Only every twentieth data point is shown for clarity. Simulation results for ^{30}Si (bold dashed line) and ^{11}B (bold solid line) are in close agreement with experimental data. Comparison of the data to the simulated intrinsic diffusion profile (dashed line) reveals greater diffusion enhancement at higher B concentrations. The solid vertical line is drawn to demonstrate the extent of the material that is extrinsic at the diffusion temperature.

In the case that the interstitialcy mechanism mediates B diffusion, the diffusion of the [BI]^0 pair also contributes to Si self-diffusion. However, simulation of the B and Si diffusion profiles using a model that includes a differential equation for the [BI]^0 pair does not yield a significant contribution of [BI]^0 to Si self-diffusion. Hence, either the kick-out mechanism controls B diffusion or the correlation factor for Si diffusion via [BI]^0 pairs is equal to or less than 0.3. Since such a low correlation factor is rather unlikely, B diffusion is considered to be mediated by the kick-out mechanism. For a discussion of the correlation factor and its role in diffusion see Section 1.2.1.
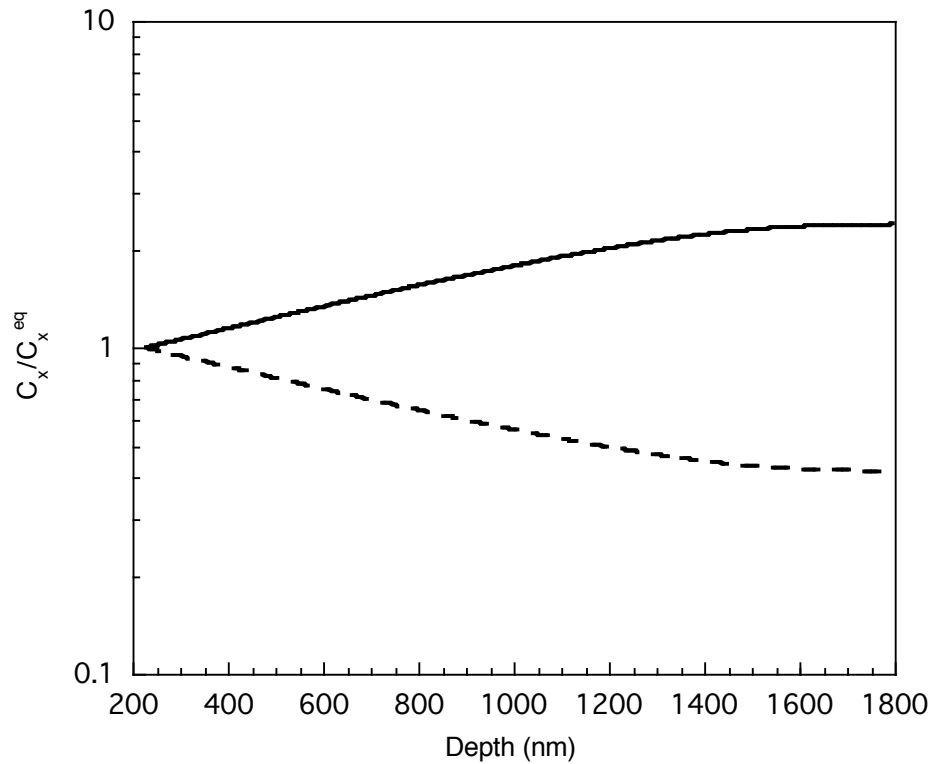
Figure 3.2 ZOMBIE simulation results for the normalized concentration of I$^+$ and I^0 (solid line) and V$^+$ and V^0 (dashed line) after diffusion in the boron implanted Si isotope heterostructure. The deviation from equilibrium extends to the upper boundary for the simulation, which was set at 4000 nm with a reflecting boundary condition. The concentration of each species has been normalized to its equilibrium concentration at that depth.

Self- and dopant diffusivity enhancements increased with increasing B doping due to I^0 and I^+ supersaturation from B diffusion and I^+ concentration enhancement due to the Fermi level effect. As expected, the contribution of I^0 is independent of the Fermi level and the contribution of I^+ increases as the Fermi level moves towards the valence band edge.

As discussed in the implant damage isolation and TED suppression technique of Section 2.1.1, no self-diffusion enhancement was observed in Si implanted multilayer structures after annealing. Therefore, the experimentally observed enhanced self-diffusion is due to the Fermi level effect and self-interstitial supersaturation rather than transient effects resulting from implantation damage.

3.1.3   Analysis

Figure 3.3 shows a plot of the self- and B diffusion coefficients as a function of reciprocal temperature. Extrinsic self- and dopant diffusion coefficients are reported for the maximum B concentration (i.e., at the amorphous/crystalline interface) at each temperature. Since the interface acts as a nearly ideal source and sink for native defects, the data in Figure 3.3 represent the pure Fermi level diffusion enhancement, independent of supersaturation effects.

To compare the B diffusivity data to literature values, the diffusion coefficients were reduced to intrinsic conditions by applying:

$$D_B(n_i) = D_B(p) \cdot n_i \big/ C_B^{eq} \qquad (3.5)$$

where n_i represents the intrinsic carrier concentration at the diffusion temperature and C_B^{eq} is the B concentration at the amorphous/crystalline interface. The diffusion coefficients of B reduced to intrinsic conditions are consistent with corresponding data reported in the literature [Antoniadis, 1978]. This reaffirms that in our experiments B and Si diffusion are not enhanced by transient diffusion phenomena that may be associated with crystallization of the B implanted amorphous Si layer or implantation damage.

Comparison of simulation results to experimental data revealed that the interstitialcy mechanism is not possible for $[BI]^0$ correlation factors greater than 0.3. Although the experimental results may be explained using the reaction mechanism given by Equation 3.2, such a low correlation factor renders the interstitialcy mechanism very unlikely. A theoretical calculation of the $[BI]^0$ correlation factor will be necessary to positively confirm this conclusion.

Figure 3.4(a) illustrates that the Si self-diffusion coefficient under heavy B doping, $D_{Si}(p)$ is clearly enhanced compared to the Si self-diffusion coefficient under intrinsic conditions, $D_{Si}(n_i)$. The neutral and singly positively charged interstitial contributions to the overall self-diffusion coefficient as a function of temperature are also shown in this figure. Singly positively charged interstitials are responsible for the enhancement of Si self-diffusion. Figure 3.4(b) shows the defect diffusivities reduced to intrinsic conditions.
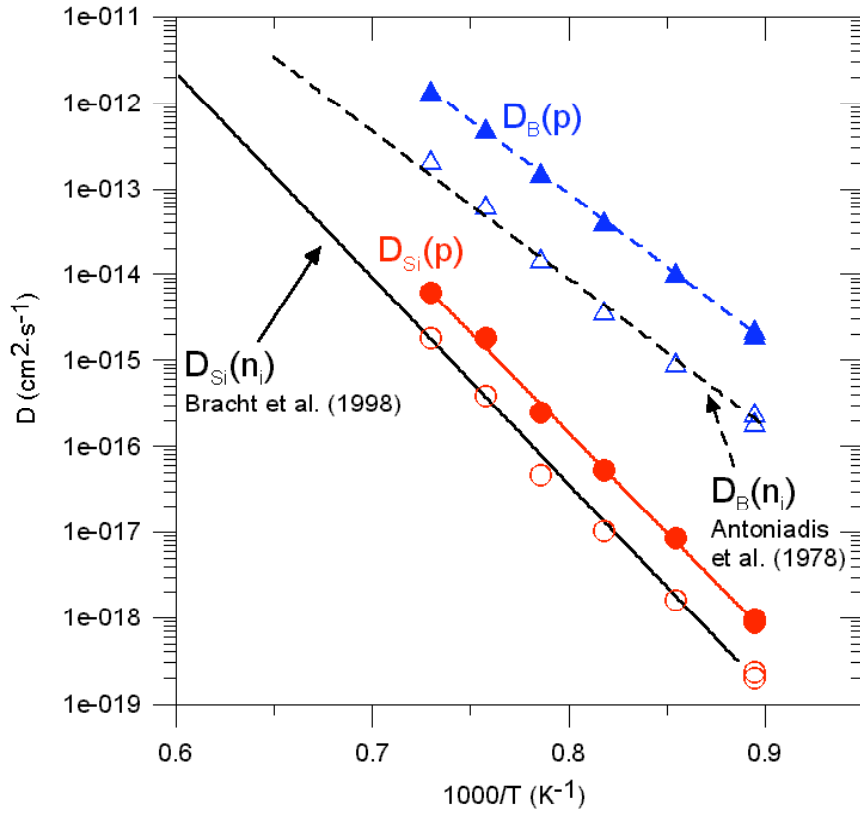
Figure 3.3 Extrinsic B(▲) and Si (●) diffusivities as a function of reciprocal temperature show a clear enhancement over literature values for intrinsic B [Antoniadis, 1978] and Si [Bracht, 1998] diffusion. B diffusivity data, reduced to intrinsic conditions (Δ), are in excellent agreement with intrinsic B diffusivities reported by Antoniadis et al. [Antoniadis, 1978]. The Si diffusivity data reduced to intrinsic conditions, (◯), are in excellent agreement with literature [Bracht, 1998].
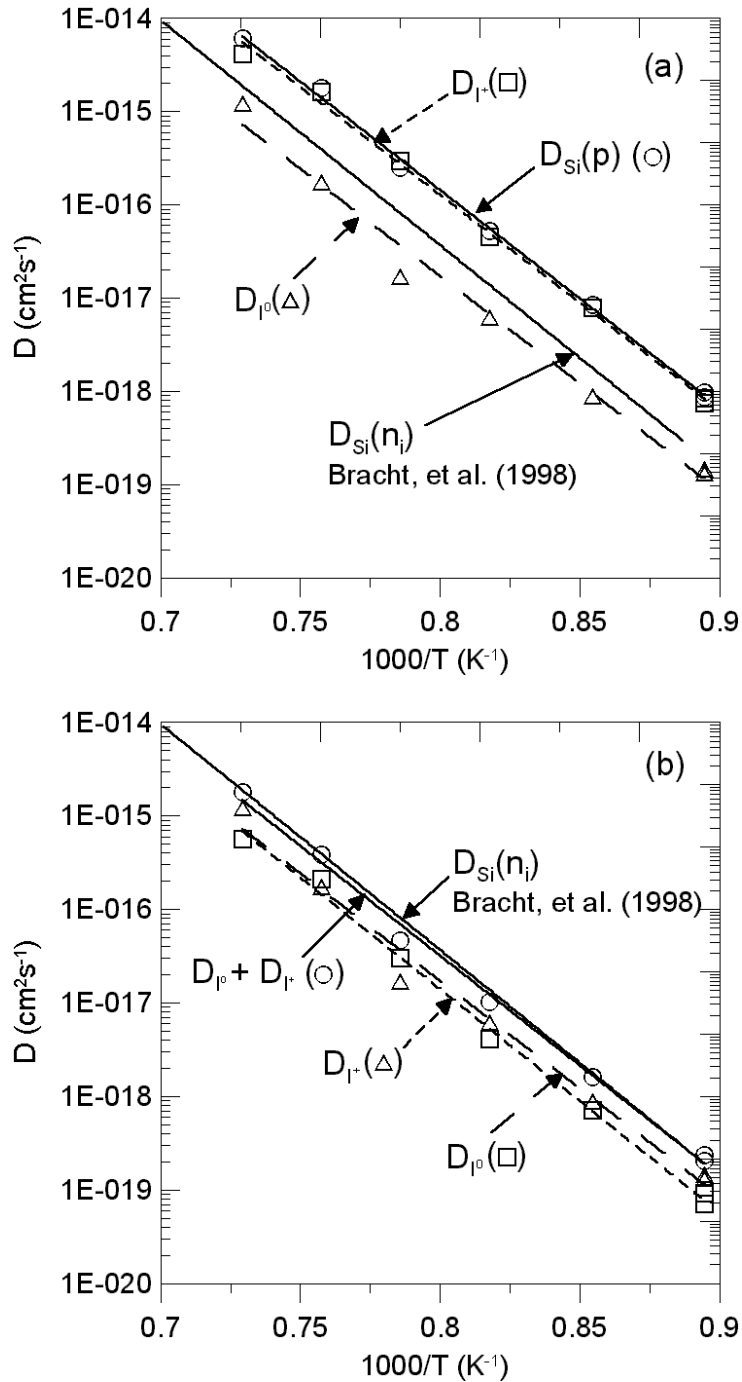
Figure 3.4 Individual contributions of neutral and singly positively charged self-interstitials to the Si self-diffusion coefficient and the sums of those contributions for (a) extrinsic and (b) intrinsic conditions. The data for figure (b) are obtained by reducing the extrinsic diffusivities obtained from the simulation to intrinsic conditions. This method allowed for the calculation of the individual Arrhenius parameters for I^0 and I^+ in intrinsic Si.

The temperature dependences of the reduced diffusivities of neutral and singly positively charged interstitials are described by the following Arrhenius expressions:

$$DI^0(n_i) = (44^{+379}_{-39})\exp\left(-(4.56 \pm 0.241\,\text{eV})/kT\right)\ \text{cm}^2\,\text{s}^{-1} \tag{3.6}$$

$$DI^+(n_i) = (177^{+434}_{-126})\exp\left(-(4.74 \pm 0.13\,\text{eV})/kT\right)\ \text{cm}^2\,\text{s}^{-1} \tag{3.7}$$

The sum of the contributions of D_I^0 and D_I^+ to Si self-diffusion is shown in Figure 3.4(b). The sum is in close agreement with data for Si diffusion under intrinsic conditions [Bracht, 1998]. The overall consistency of the Si and B intrinsic diffusion data with corresponding data in the literature supports the diffusion reaction mechanisms (Equations 3.3 and 3.4) considered for simultaneous diffusion of B and Si.

In conclusion, the results presented in this work demonstrate that B diffusion occurs via the kick-out mechanism and that the interstitialcy mechanism is highly unlikely. A theoretical calculation of the correlation factor of the $[BI]^0$ pair would be helpful in ultimately discerning the diffusion mechanism. It has also been determined that neutral and singly positively charged self- interstitials mediate self- and dopant diffusion. Observed diffusion enhancements under extrinsic conditions arise from increased singly positively charged interstitial concentrations due to the Fermi level effect and interstitial supersaturation due to B diffusion. Substantial vacancy contributions to diffusion were not observed. The Arrhenius expressions for the individual diffusion coefficients of neutral and singly positively charged interstitials in intrinsic Si were obtained from reduction of extrinsic data to intrinsic conditions.

1.2 Diffusion of Arsenic in Silicon under Extrinsic Conditions

1.2.1 Introduction

Arsenic was chosen as a dopant for the simultaneous self- and dopant diffusion studies because it is an n-type dopant; therefore it will shift the Fermi level toward the conduction band, enhancing the formation and concentration of negatively charged native defects (see Table 1.1). Arsenic diffusion has been demonstrated to be mediated by both interstitials and vacancies by observation of enhanced As diffusion during oxidization (interstitial injection) and nitridation (vacancy injection) [Fahey, 1989]. Therefore, experiments using As should yield information on the contribution of both native defects to self- and dopant diffusion. Unlike B diffusion discussed in Section 3.1, As diffusion does not generate a supersaturation of native defects during diffusion. Therefore any diffusion enhancement seen under As doping can be attributed entirely to the Fermi level effect.

To create the heavily doped arsenic diffusion source, sequential implants of arsenic were performed at 130 keV with a dose of 0.7×10^{16} cm^{-2} and 160 keV at 1.0×10^{16} cm^{-2} into the amorphous cap layer. After implantation, the samples were diced into 4×4 mm^2 pieces. Then each individual sample was sealed in a silica ampoule under 0.5 atm Ar, to aid thermal transport, and annealed in a Lindberg/Blue resistance-heated tube furnace for appropriate times and temperatures. A type-S, Pt-Rh, thermocouple was used to monitor the temperature.   The ampoules were quenched in water to terminate the

diffusion. Depth profiles for ^{30}Si and ^{75}As were measured via Secondary Ion Mass Spectrometry (SIMS) on an Atomika 4500 at Accurel Systems (Sunnyvale, CA). A 1.5 keV Cs$^+$ beam was used for the SIMS analysis.

1.2.2 Experimental Approach and Results

Arsenic implanted samples were annealed at temperatures between 900 and 1100 °C. Figure 3.5 illustrates the concentration versus depth profiles of ^{75}As and ^{30}Si after annealing at 950 °C for 122 hrs. Since arsenic diffusion is known to take place via interactions with vacancies and interstitials, it was modeled as a combination of the vacancy and interstitialcy mechanisms (see section 1.2.1). The experimental As and Si profiles are mainly described by the reactions:

$$\left(AsV\right)^o \leftrightarrow As_s^+ + V^o + e^- \tag{3.8}$$

$$\left(AsI\right)^o \leftrightarrow As_s^+ + I^- \tag{3.9}$$

where e$^-$ is an electron required to satisfy charge neutrality and AsV and AsI are the arsenic-vacancy and arsenic-interstitial pairs, respectively. The superscripts in Equations 3.8 and 3.9 indicate the charge states determined from the experimental results.

In order to demonstrate the sensitivity of the experimental profiles on the charge state of the native defects, the As and Si profiles were also calculated assuming neutral and doubly negatively charged defects. It is evident from Figure 3.5 that the enhanced Si self-diffusion within the two near-surface ^{28}Si layers is caused by a singly negatively charged native defect. Note, the As diffusion profile alone is not sensitive to the charge states of the native defects involved. Different charge states for the native defects
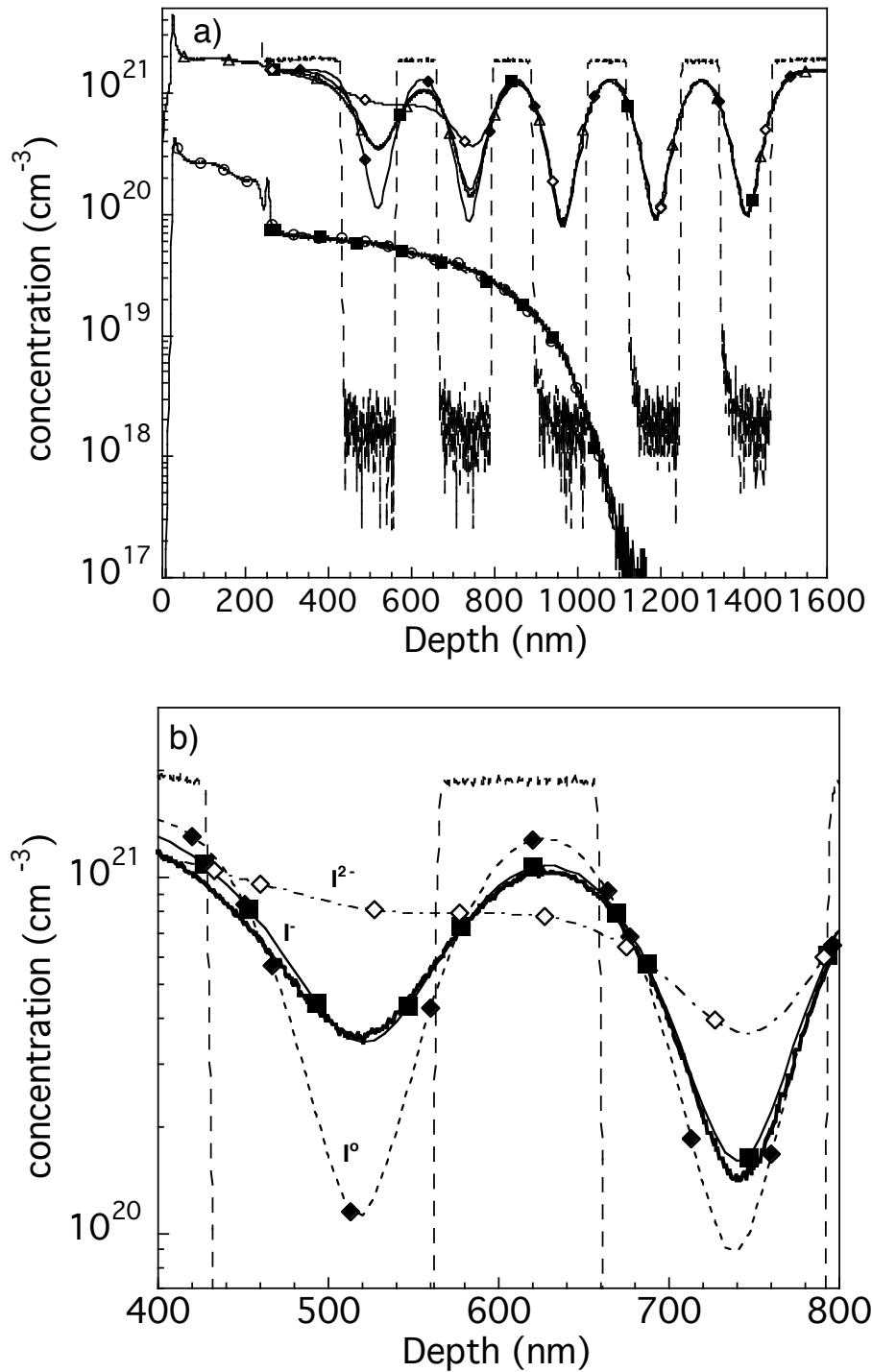
Figure 3.5 a) Concentration versus depth profile for an As implanted Si isotope heterostructure after annealing at 950 °C for 122 hours. Plot shows pre-anneal ^{30}Si profile (dashed line) along with the annealed profile. b) Enlarged view of the region of enhanced Si diffusion. Simulated diffusion profiles of different native defect charge states are included to show variation of the simulation with the charge state. The singly negatively charged defect is shown to lead to the best fit to the data (solid line).

assumed in the simulation all result in similar As diffusion profiles. This demonstrates that the simultaneous diffusion of dopant- and self-atoms provide a better insight into the mechanisms of dopant diffusion than the analysis of dopant profiles alone.

Arsenic diffusion is not associated with a supersaturation or under-saturation of native point defects which would affect Si self-diffusion. Instead, As diffuses under thermal equilibrium conditions, i.e., the concentration of vacancies and self-interstitials is close to the thermal equilibrium value for the given experimental conditions. This is evident in the plot of the ZOMBIE simulation results for concentration of native defects versus depth referenced to the equilibrium concentration at the given depth, presented in Figure 3.6. In contrast to Figure 3.2 for boron diffusion, there is no supersaturation or undersaturation visible in the simulation results of Figure 3.6.

Therefore, the enhanced Si diffusion, which is evident from Figure 3.5 in the region where the As concentration is high, is due to the increased concentration of negatively charged native defects caused by the Fermi level shift. As discussed in Section 1.3.1, the introduction of the positively charged As ions shifts the Fermi level towards the conduction band, resulting in a lowering of the formation energy for negatively charged defects and an increasing defect concentration.
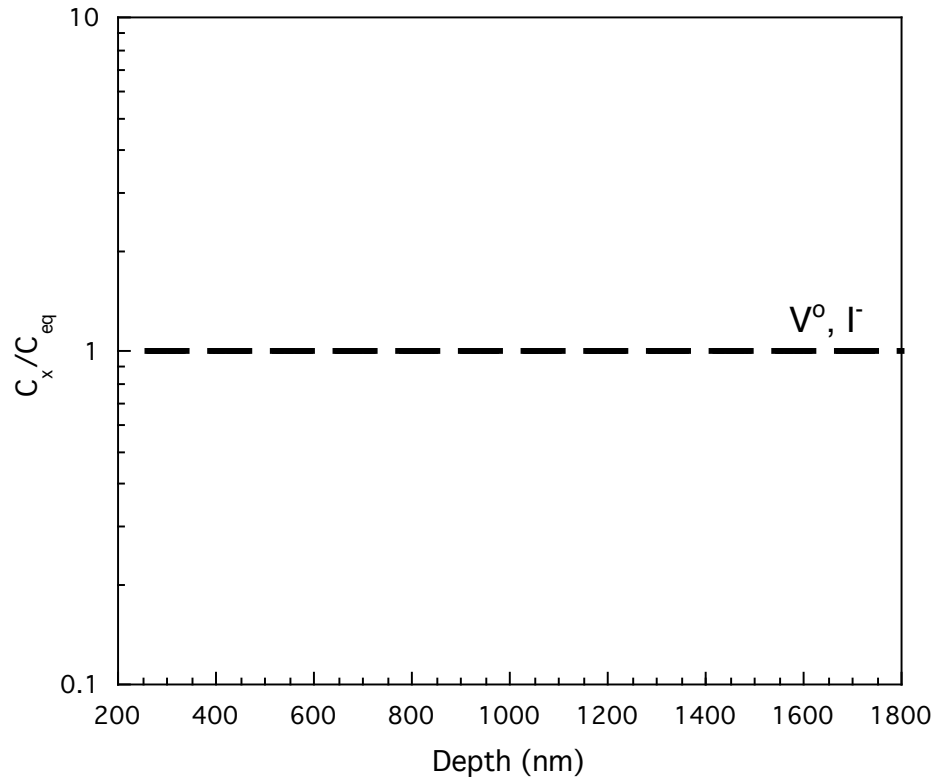
Figure 3.6 ZOMBIE simulation results for the normalized concentration of V^o and I^- (dashed line) after diffusion in the arsenic implanted Si isotope heterostructure. The concentration of each species has been normalized to its equilibrium concentration at that depth.

Finally, it is noted that the experimental As and Si profiles are also accurately described assuming I^o and V^- in reactions 3.8 and 3.9, respectively, as the equations are mathematically identical upon swapping the charge state of the interstitial and vacancy. However, from the P diffusion results presented in Section 3.3, it is clear that the appropriate charge state assignment is V^o and I^-, a neutral vacancy and singly negatively charged self-interstitial.

65

1.2.3   Analysis

The enhancement of diffusion of both the Si and As under extrinsic conditions is shown in Figure 3.7(a) in comparison to data for intrinsic conditions (Si:[Bracht, 1998]; As:[Masters, 1969]). Similar enhancements of Si diffusion under high n-type doping have been reported in the literature [Nakabayashi, 2001; Ural, 2001]. The As diffusion coefficients for extrinsic conditions can be reduced to intrinsic conditions via [Uematsu, 1997]:

$$D_{As}(n_i) = D_{As}(ext) \cdot \frac{n_i}{C_{As_s}^{eq}}$$

(3.10)

where n_i represents the intrinsic carrier concentration [Morin, 1954] and $C_{As_s}^{eq}$ is the concentration of As at the amorphous crystalline interface. The values for $D_{As}(n_i)$ obtained by Equation (3.10) are in good agreement with data for $D_{As}(n_i)$ reported in the literature [Masters, 1969]. This agreement is considered to be a consistency check for the diffusion models which were used to describe the As diffusion. The Si diffusion coefficients under extrinsic n-type conditions are mainly determined by the contribution of the negatively charged interstitial.

The individual contributions of the negatively charged interstitial and the neutral interstitial to Si self-diffusion under intrinsic conditions as well as their sum are shown in Figure 3.7(b). The closed circles in Figure 3.7(b) represent data from previous diffusion experiments where the total Si self-diffusion coefficient was determined [Bracht, 1998]. The data given by the open symbols represent the contribution of the singly negatively charged self-interstitial and the neutral interstitial as well as the contribution of the singly
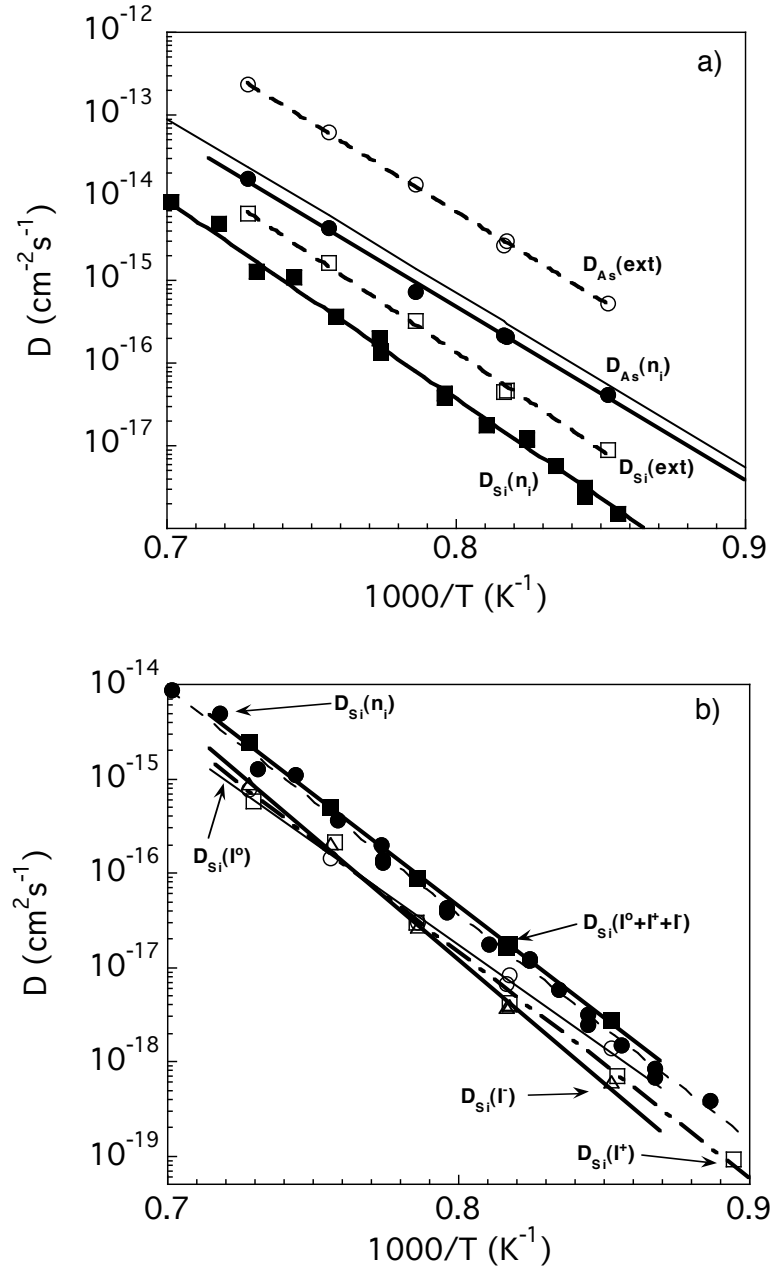
Figure 3.7 a) Diffusion coefficient versus 1000/T for As (circles) and Si (squares), under intrinsic conditions (solid lines, solid symbols) and extrinsic conditions (dashed lines, open symbols). The thin solid line represents the intrinsic As diffusion from literature [Masters, 1969] b) Plot of diffusion coefficient versus 1000/T for Si self-diffusion under intrinsic conditions. The open symbols represent the individual contributions of native defects. The solid squares are the sum of the contributions of the native defects at each temperature. The solid circles and thin dashed line represent the total self-diffusion values from [Bracht, 1998] for comparison.

positively charged self-interstitial determined from B diffusion experiments [Sharp, 2002].

The temperature dependence of the individual contributions to Si self-diffusion and the sum of all contributions follows an Arrhenius expression. The corresponding pre-exponential factors, D_o, and activation enthalpies, Q, are listed in Table 3.1. Also included in Table 3.1 are the values for the total Si self-diffusion determined recently [Bracht, 1998].

The simultaneous diffusion of As and Si in the isotope multilayer structure is accurately described on the basis of the interstitialcy and vacancy mechanisms. The simulations yield data on the contribution of I^- to Si self-diffusion. There is no evidence of a V^{2-} component to As diffusion. The total Si self-diffusion was determined from the sum of the I^o and I^- contributions and the I^+ contribution obtained from B diffusion experiments. This total Si self-diffusion coefficient is in good agreement with data for Si self-diffusion reported recently.

The enhancement of Si self-diffusion during the in-diffusion of As is considered to be associated with the increase in the equilibrium concentration of singly negatively charged self-interstitials. Negatively charged interstitials are energetically favored when the Fermi level moves towards the conduction band with increasing As doping.

Table 3.1 Pre-factor, D_o, and activation energy, Q, for individual native defect contributions to Si self-diffusion and their sum, along with the total Si self-diffusion (column 6) determined from [Bracht, 1998].

	I^o	I^+	I^-	D_{sum}	D_{Si}
ln $(D_o$/cm^{2}s$^{-1})$	1.49 ± 1.37	5.18 ± 1.24	9.18 ± 1.19	6.01 ± 0.76	6.27 ± 0.39
Q (eV)	4.32 ± 0.15	4.74 ± 0.13	5.18 ± 0.13	4.70 ± 0.08	4.75 ± 0.04

The present study yields an activation enthalpy of Si diffusion via negatively charged interstitials of 5.18 eV. As previously noted, the results deduced for I^- and V^o may also correspond to V^- and I^o because the simulations of the As and Si diffusion profiles can not distinguish between these native defects. However, the experiments on the simultaneous diffusion of P and Si, presented in the following section, allow for the identification of the negatively charged native defect under n-type doping conditions to be the singly negatively charged self-interstitial.

1.3 Diffusion of Phosphorus in Silicon under Extrinsic Conditions

1.3.1 Introduction

Phosphorus was chosen as the final dopant to be investigated for the simultaneous self- and dopant diffusion studies because it will help to clarify the role, if any, of the singly negatively charged Si self-interstitial. From Table 1.1, it is evident that the donor P will shift the Fermi level toward the conduction band, enhancing the formation and concentration of negatively charged native defects. Figure 1.10 details the known native defect charge states in Si. Absent from Figure 1.10 is any information on the singly negatively charged self-interstitial because no experimental evidence of its existence has yet been observed.

Intrinsic phosphorus diffusion has been demonstrated to be retarded under nitridation (vacancy injection) conditions [Mizuo, 1983; Fahey, 1985a]. From this retardation, it was concluded that the intrinsic P diffusion was entirely interstitially mediated [Tan, 1985]. For heavy P doping yielding extrinsic conditions, the retardation of P diffusion under nitridation was observed to decrease, signifying an increased contribution of vacancies to the diffusion [Fahey, 1985b]. Additionally, the P diffusivity was found to be proportional to the square of the P concentration for high P concentrations, indicating that the vacancy mechanism, involving a negatively charged PV pair and a doubly negatively charged vacancy (V^{-2}), is the dominant diffusion mechanism at high P concentrations [Fair, 1977]. Therefore, using P as the dopant in

simultaneous dopant and self-diffusion experiments should yield information on the

contribution of both the negatively charged self-interstitial and the negatively charged

vacancy to self- and dopant diffusion. This should help clear up the ambiguity over the

charge states of the defects during As diffusion discussed in Section 3.2.3. It will also

determine the contribution of these native defect charge states to Si self-diffusion.

To create the heavily doped phosphorus diffusion source, sequential implants of

phosphorus were performed at 65 keV with a dose of 7×10^{15} cm^{-2} and 75 keV at 7×10^{15}

cm^{-2} into the amorphous cap layer. After implantation, the samples were diced into 4×4

mm^2 pieces. Then each individual sample was sealed in a silica ampoule under 0.5 atm

Ar to aid thermal transport and to prevent oxidation and annealed in a Lindberg/Blue

resistance-heated tube furnace for appropriate times and temperatures. A type-S, Pt-Rh,

thermocouple was used to monitor the temperature. The ampoules were quenched in

water to terminate the diffusion. Depth profiles for ^{30}Si and ^{31}P were measured via SIMS

on a Cameca 4f at Accurel Systems (Sunnyvale, CA).

1.3.2   Experimental Approach and Results

The P diffusion samples were annealed at temperatures ranging from 850 to 1100

°C. After the thermal treatments, the surface of the amorphous cap layer had become

very rough. The surface of the samples also appeared to have a red or green tint after the

thermal treatments. Atomic Force Microscopy (AFM) was performed at the Lawrence

Berkeley National Laboratory by Ian Sharp to determine precisely the surface roughness

of the samples. The AFM images of a phosphorus implanted Si sample annealed at 1000

°C for 4 hours are presented in Figure 3.8. The surface was covered with raised features approximately 100 nm high and 400 nm wide. The root mean square (rms) surface roughness was calculated from Figure 3.8a to be 28 nm. This large surface roughness resulted in tremendous errors in the SIMS depth profiles since the surface roughness can be a limiting factor in the depth resolution of the SIMS measurement. Several methods were utilized in an attempt to remove or prevent the roughening of the surface during heat treatment. Chemical etching after annealing failed to remove the surface roughness, and the use of a Si proximity cap during annealing failed to prevent the formation of the surface features. The mechanical polishing of the surface after heat treatment to remove the amorphous cap layer was a successful approach to improving the quality of the surface. After the heat treatments are complete, the cap layer, which has the primary function of a dopant source, is no longer needed and can be sacrificed during polishing.

The mechanical polishing was performed on a Logitech PM5 polishing machine using Syton HT 50 colloidal silica as the slurry on a MD-Chem cloth polishing pad. The samples were polished for 20-second intervals and cleaned and inspected for removal of the red or green color of the surface. This process was repeated until the color was removed. The total polishing time for each sample was between 1 and 2 minutes. After polishing, AFM measurements were repeated to determine the improvement in the surface quality. Figure 3.8b is an AFM image of the sample after polishing. The surface roughness had improved to an rms value of 10 nm, which was acceptable for the SIMS measurement. All samples were polished to an rms surface roughness of 10 nm or less. Figure 3.9 shows the SIMS concentration profiles before and after polishing. The source of the Si surface roughness after annealing was not conclusively resolved.
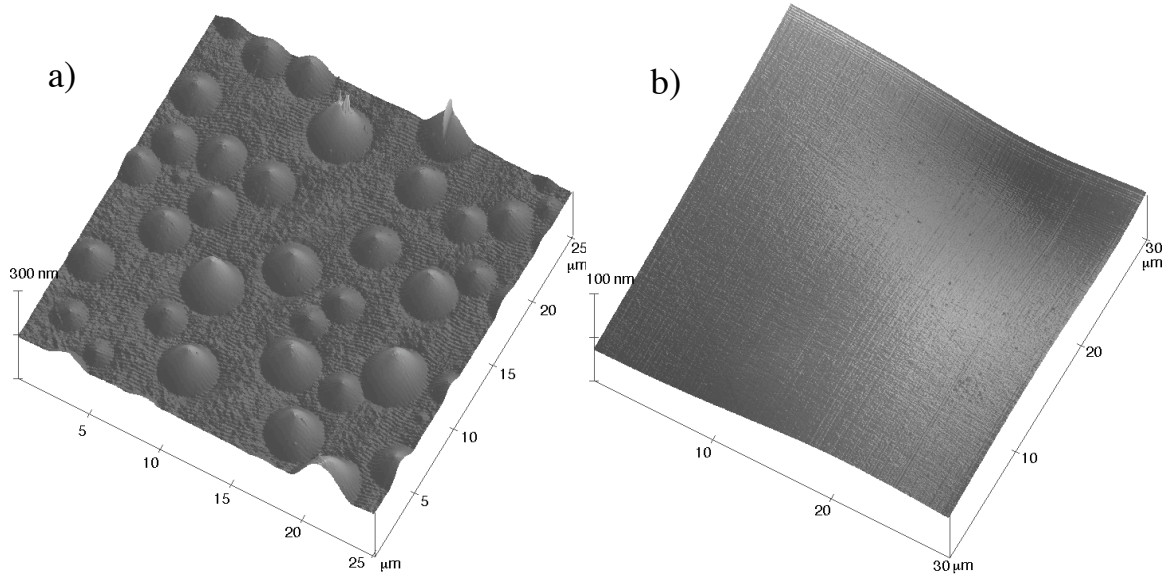
Figure 3.8 Atomic Force Microscopy (AFM) images of a phosphorus implanted silicon isotope structure after annealing at 1000 °C for 4 hours. a) The as-annealed surface showing the raised features and rms roughness of 28 nm. b) The sample surface after polishing of the cap layer. The raised features have been removed and the surface roughness has improved to 10 nm.
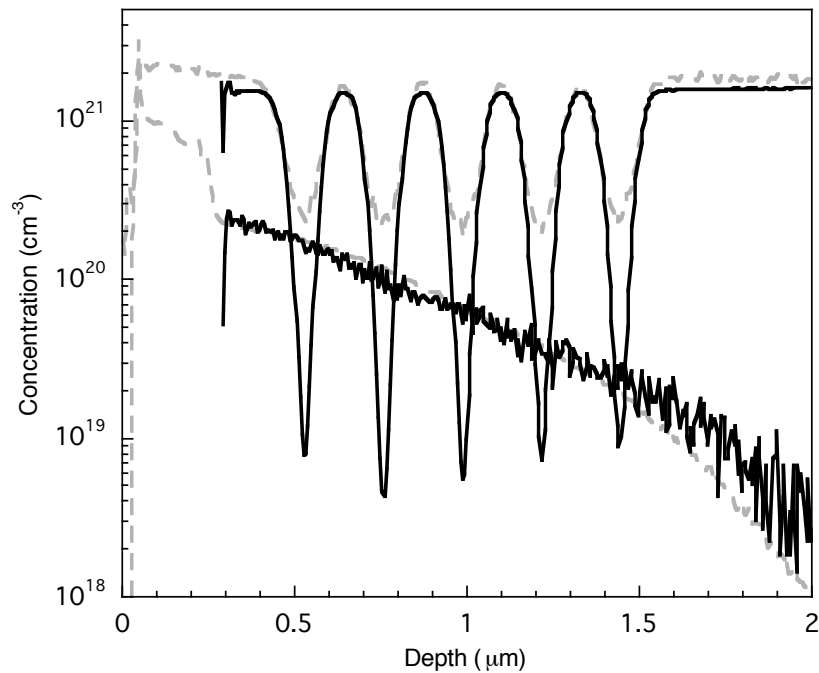

Figure 3.9 SIMS concentration profiles of Si and P in the isotope heterostructure after annealing at 1000 °C for 4 hours. The as-annealed profiles are shown as gray dashed lines. The profiles after polishing off the cap layer, which show improved depth resolution, are black solid lines.

73

It is evident from Figure 3.9 that the surface roughness prior to polishing greatly diminished the depth resolution of the SIMS measurement. It is also clear that the technique of polishing the surface improved the depth resolution by almost 2 orders of magnitude. It is worthwhile to note that the surface roughness had little effect on the phosphorus depth profile. This is a result of the smaller gradient in the phosphorus profile causing the impact of reduced depth resolution to be less significant.

From the accurate SIMS profiles generated after sample polishing, a model for simultaneous P and Si diffusion was generated based on the following reactions:

$$PI^{o}(P_{i}^{o}) \Leftrightarrow P_{s}^{+} + I^{o} + e \qquad\qquad (3.11)$$

$$PI^{o}(P_{i}^{o}) \Leftrightarrow P_{s}^{+} + I^{-} \qquad\qquad (3.12)$$

$$PI^{o}(P_{i}^{o}) + V^{o} \Leftrightarrow P_{s}^{+} + e \qquad\qquad (3.13)$$

$$PI^{+}(P_{i}^{+}) \Leftrightarrow P_{s}^{+} + I^{o} \qquad\qquad (3.14)$$

$$PI^{+}(P_{i}^{+}) + V^{o} \Leftrightarrow P_{s}^{+} \qquad\qquad (3.15)$$

where PI and P_i represent the phosphorus-interstitial pair and interstitial phosphorus atom, respectively, for the given charge states. The vacancy and interstitial of the corresponding charge state are represented by V and I, while e represents electrons used in the reaction for charge neutrality. The interstitial phosphorus representation is given in each equation along with PI because the model has only been generated for PI and therefore, strictly from a modeling standpoint, P_i cannot be ruled out as a possible replacement for PI in the above equations without further modeling.

Figure 3.10 is a plot of the SIMS data for a sample annealed at 1100 °C for 30 minutes along with the best-fit simulation of the above reactions to the data set. From the
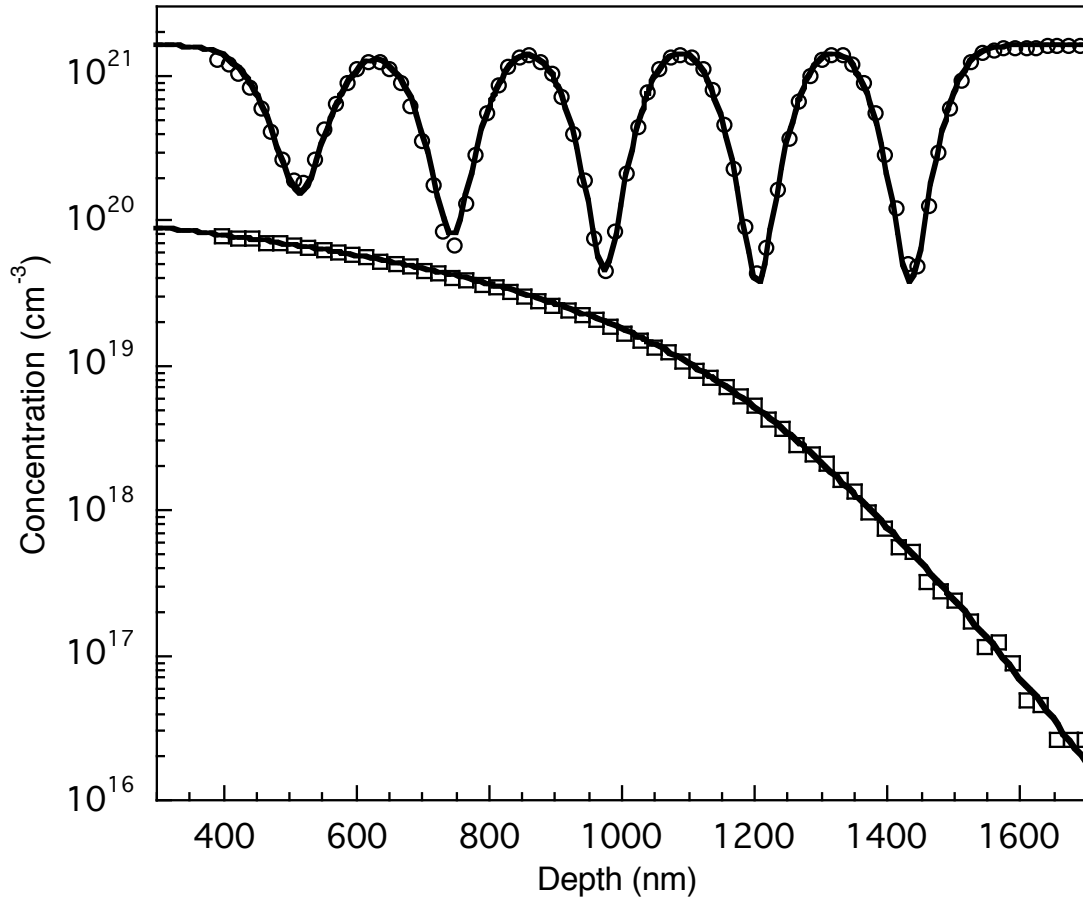
Figure 3.10 Plot of the SIMS depth profile of ^{31}P (squares) and ^{30}Si (circles) in a Si isotope structure annealed at 1100 °C for 30 minutes. Also shown in the figure is the best fit simulation (lines) to the profiles generated from Equations 3.11 to 3.15. Every third data point is displayed for clarity.

figure it is evident that the model described by the reactions in Equations 3.11 to 3.15

accurately describe both P and Si diffusion simultaneously.

1.3.3 Analysis

The reactions described by Equations 3.11, 3.12, and 3.14 represent either the interstitialcy or kick-out mechanism, depending on whether the P defect is a PI pair (interstitialcy) or interstitial P atom (kick-out). To accurately describe the experimental profiles, the interstitial mediated reactions required the involvement of both neutral and singly negatively charged self-interstitials, I^o and I^-, along with neutral and singly positively charged mobile P species. The two vacancy mediated reactions, 3.13 and 3.15, can either be represented as the pair assisted annihilation mechanism or the dissociative mechanism depending on the identity of the mobile P species which may be resolved by further modeling. The defects required in these reactions for accurate model fitting are the neutral vacancy, V^o, and the neutral or singly positively charged mobile P species.

The model proposed here differs from that of the most widely accepted model of the reactions involved in P diffusion. The model proposed by Uematsu, [Uematsu, 1997], is based on a kick-out mechanism of interstitial diffusion involving a neutral interstitial, I^o, and a vacancy mechanism for vacancy mediated diffusion involving a singly and doubly negatively charged vacancy, V^{-2} and V^-. In the model proposed in this work, no contribution from a vacancy mechanism is required and no evidence of the involvement of a doubly negatively charged native defect is observed, while a negatively charged interstitial is required along with a positively charged P species. It should be noted that, in contrast to the present work, the experimental data upon which Uematsu formed his model contained no Si self-diffusion profile. The model was based on fitting

to a set of P diffusion profiles only. To check the accuracy of the Uematsu model for

fitting both Si and P diffusion simultaneously, the model of Uematsu was applied to the

same data set as shown in Figure 3.10, a Si isotope heterostructure annealed at 1100 °C

for 30 minutes. The results of the fit of the Uematsu model to the simultaneous Si and P

diffusion from this work are presented in Figure 3.11 along with the reaction equations of

the Uematsu model. The dashed line in Figure 3.11 represents the best-fit of the P data to

the experimental results. It is clear that under the model proposed by Uematsu, the P

diffusion profiles generated in this work can be accurately described. However, the

simultaneous modeling of the Si self-diffusion profile along with the best-fit of the P

using the Uematsu model does not yield an accurate description of the Si self-diffusion.

The solid line in Figure 3.11 represents an attempt to generate a best-fit of the Si profile

from the simultaneous Si and P data using the Uematsu model. An accurate

representation of the Si profile can be generated, but the P profile generated by that fit is

no longer appropriate. Therefore it appears that the model proposed by Uematsu, while

accurate for the description of P diffusion, cannot describe the simultaneous diffusion of

Si and P.

From the fitting of the experimental data to the model given in Equations 3.11 to

3.15, diffusion coefficients for Si diffusion via interstitials and P diffusion over the

temperature range of 950 °C to 1100 °C were generated. The temperature dependence of

these values is plotted as an Arrhenius relation in Figure 3.12. Also plotted in Figure

3.12 are lines representing the previous results for intrinsic P diffusion [Makris, 1973]

and the previous results for Si diffusion via a negatively charged self-interstitial, from
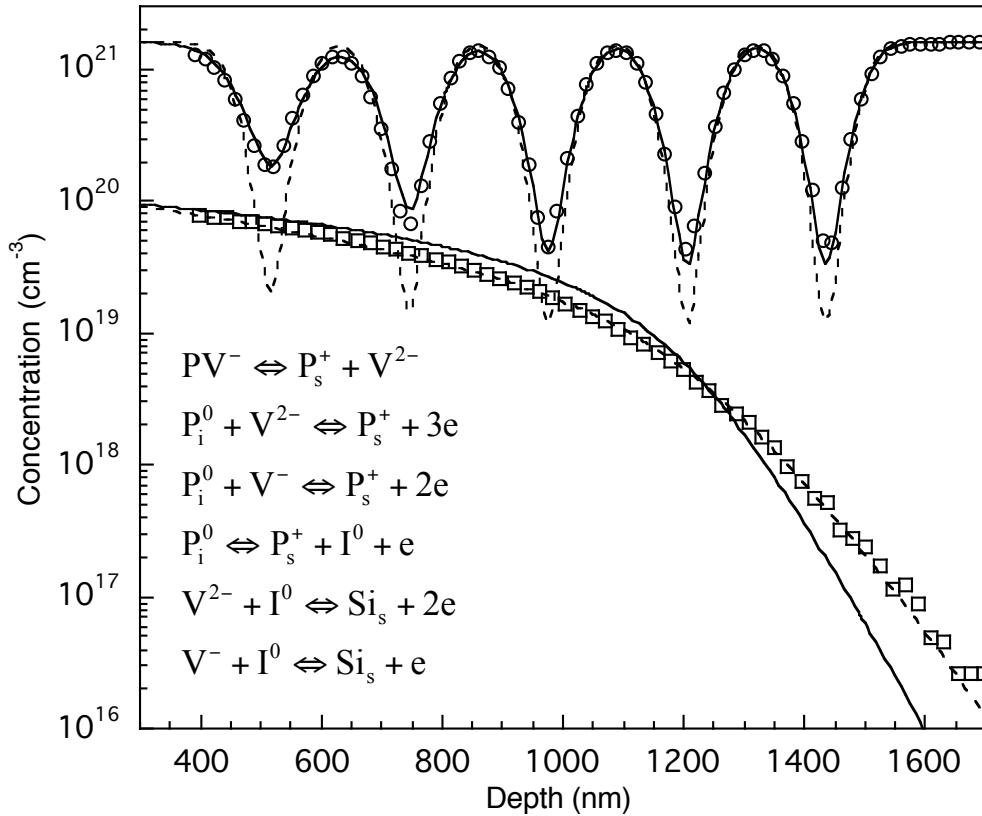
Figure 3.11 SIMS concentration profiles of ^{30}Si (circles) and ^{31}P (squares) for a sample annealed at 1100 °C for 30 minutes, along with simulations for the model proposed by Uematsu [Uematsu, 1997]. The dashed line represents best fit of Uematsu's model to the P profile yielding a poor fit to the Si profile, while the solid line is the best fit of Uematsu's model to the Si profile, which does not accurately describe the P profile. Only every third SIMS data point is shown for clarity. The diffusion reactions proposed by Uematsu are inset [Uematsu, 1997].

Section 3.2.3. The temperature dependence of the data was derived from exponential fits to the diffusivity values. Close agreement is observed between the literature values for P diffusion in Si of Makris and Masters and the present work. The agreement of the diffusion coefficient for the negatively charged self-interstitial between the As and P results is considered to be a check of consistency of the technique of simultaneous dopant and self-diffusion in Si isotope heterostructures.

78
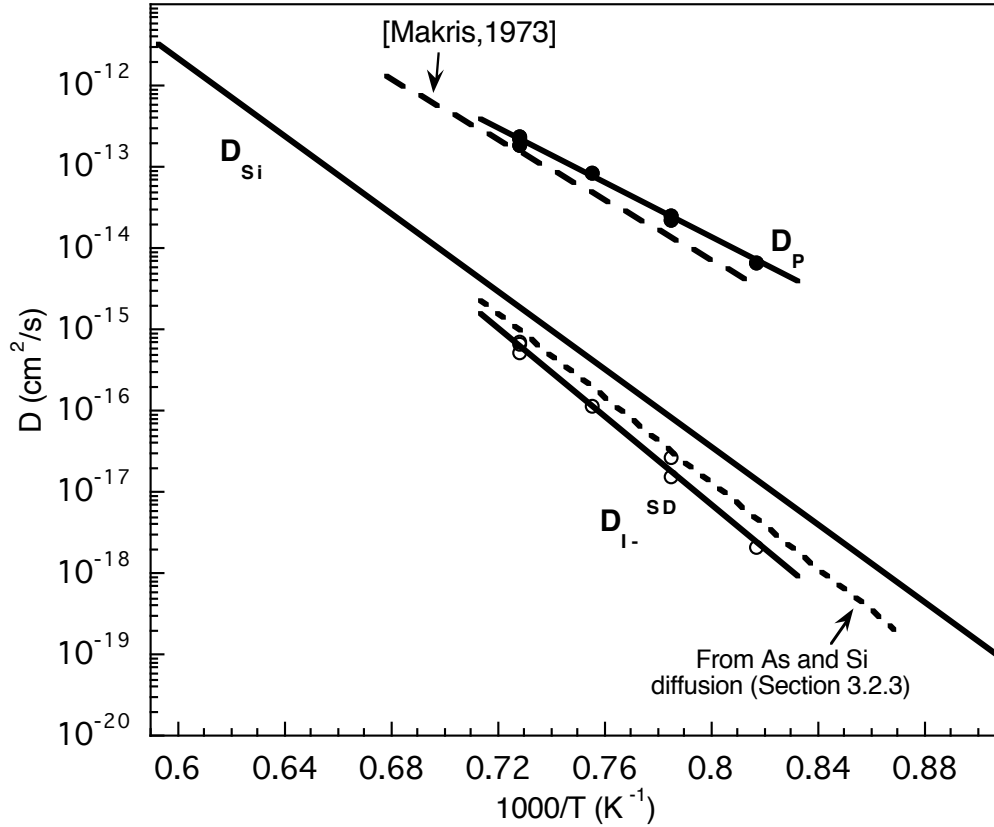
Figure 3.12 Plot of the diffusion coefficient for P and Si as a function of inverse absolute temperature. The contribution of the negatively charged self-interstitial derived from simultaneous Si and P diffusion (open circles, solid line) is shown in close agreement with the results for simultaneous As and Si diffusion from Section 3.2.3 (short dashed line). The values for the intrinsic P diffusion from this work (close circles, solid line) are plotted along with the values from literature (long dashed line). The Arrhenius dependence of the total Si self-diffusion, D_{Si} [Bracht, 1998], is also shown for reference.

The temperature dependence of the P and I^- contribution to self-diffusion are

given by the following expressions:

$$D_P = 0.36^{+0.64}_{-0.23} \cdot \exp\left(-\frac{(3.33 \pm 0.11)eV}{kT}\right) cm^2 s^{-1} \tag{3.16}$$

$$D^{SD}_{I^-} = \left(4.3^{+32.0}_{-3.8}\right) \cdot 10^4 \cdot \exp\left(-\frac{(5.40 \pm 0.24)eV}{kT}\right) cm^2 s^{-1} \tag{3.17}$$

79

where k is Boltzmann's constant and T is the temperature in Kelvin. The values for the activation energy, Q, from these expressions confirm the agreement with previous results for P (Q = 3.69 eV [Makris, 1973]) and the negatively charged Si interstitial contribution (Q = 5.18 eV [Table 3.1 (this work)]).

The proposed model has several implications for the mechanisms and properties of P diffusion in Si. First, it indicates that interstitials are more important than vacancies for P diffusion below the P concentration of 2×10^{20} cm^{-3}, which was the highest concentration observed in this study. Secondly, this model requires the existence of a singly negatively charged Si self-interstitial defect and a singly positively charged P mobile species. No doubly negatively charged defect or a vacancy mechanism was needed for accurate fitting of the profiles. Finally, it should be noted that the tail in the P diffusion SIMS profile, seen in Figures 3.10 and 3.11, could not be modeled solely by the interstitial supersaturation generated from P diffusion, as in the case of B diffusion (Section 3.1.3). For the P diffusion profiles, the extended tail could only be fit by the additional incorporation of the positively charged mobile P species, which would lead to a more extended tail than a neutral P defect, as a result of charge repulsion from the ionized substitutional P species. It is this result that leads to the conclusion of the existence of a positively charged mobile P species.

4 Diffusion of Silicon in Germanium

4.1 Introduction

For the initial step in the study of the self-diffusion of Si and Ge in $Si_{1-x}Ge_x$ alloys, the diffusion coefficient of Si in Ge will be determined from a buried layer Si grown into an epitaxial Ge layer. This will allow the accurate representation of the end point (x = 1) of the compositional dependence of diffusion of Si in a $Si_{1-x}Ge_x$ alloy.

As discussed in Section 1.2.2, the germanium radioactive isotope, [71]Ge, has been used for decades as a self-diffusion tracer in silicon due to the similarity in diffusion of the two species and the much longer half-life of [71]Ge (11.2 days) compared to [31]Si (2.6 hours). As a result, there is a large amount of data on the diffusion of Ge in Si [Stolwijk, 1998]. There is very little data, however, on the diffusion of Si in Ge. One of the first reports of the diffusion coefficient of Si in Ge dates back to1981. The researchers used implanted [30]Si into germanium, along with the [30]Si(p,γ)[31]Si resonance broadening technique to measure the diffusion profiles. In the temperature range of 650 to 900 °C, they found an activation enthalpy for Si diffusion in Ge of 2.9 eV and an exponential pre-factor of 0.24 cm[2]/s [Räisänen, 1981]. More recently, Si diffusion in Ge in the temperature range of 650 to 950 °C was measured via SIMS from a Si surface layer deposited on a Ge wafer. These authors found an activation enthalpy of 3.47±0.07 eV and a pre-factor of 140±50 cm[2]/s [Södervall, 1997]. Using the implantation of the radiotracer, [31]Si, into Ge and in-situ annealing and ion beam sectioning to determine the depth profiles, Strohm, et al., found an activation energy of 3.19 eV and a pre-factor of

43 cm^2/s [Strohm, 2002]. Si implantation into Ge and SIMS analysis was also performed in the temperature range of 750 to 890 °C by Uppal, who found an activation energy of 3.18 eV and pre-factor of 9.7 cm^2/s [Uppal, 2003].

While the above results yield fairly consistent values for the activation energy of Si diffusion in Ge, they were obtained from experiments involving either diffusion from the surface or from an implanted source. Since surfaces and implantation are known to affect the equilibrium concentrations of native defects, a measurement technique independent of these possible factors is desirable in order to help determine precisely the diffusion coefficient of Si in Ge.

4.2   Experimental Approach and Results

To establish the diffusion coefficient of Si in Ge, the diffusion structure had to be designed in such a way as to allow for the measurement of the diffusion of Si in Ge under equilibrium conditions. This meant a structure that would prevent the surface from affecting the diffusion and a structure that did not require implantation to introduce the Si tracers. A Ge structure containing a buried layer of Si would be able to meet these requirements. This was achieved by the growth of a 700 nm thick epitaxial layer of natural germanium on a germanium substrate via MBE at the University of Aarhus in Denmark by the group of Arne Nylandsted Larsen. During growth, a 150 nm thick spike of natural Si with a concentration of $\sim 10^{20}$ cm^{-3} was incorporated into the epitaxial Ge layer. Figure 4.1 is a SIMS depth profile of the ^{28}Si concentration in the as-grown Ge epilayer.
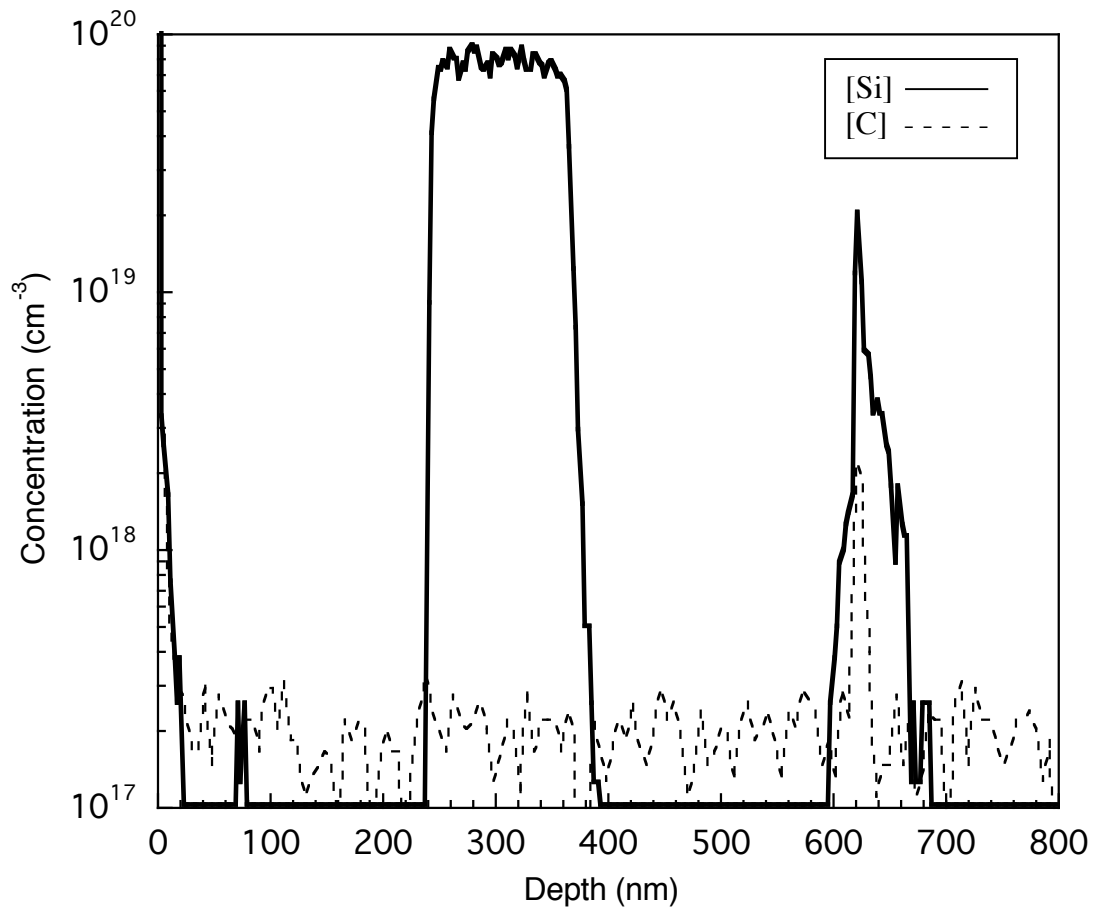
Figure 4.1 SIMS depth profile of the as-grown MBE Ge epilayer showing the concentration of ^{28}Si (solid line) and C (dashed line). The Ge epilayer/substrate interface occurs at a depth of 700 nm and carbon and Si contamination at the interface has resulted in the trapping of Si at the interface and the formation of a second Si peak. The primary MBE grown natural Si doped layer has a ^{28}Si concentration of 8×10^{19} cm^{-3}.

The as-grown Ge epilayer shown in Figure 4.1 revealed an unintended Si peak at the Ge epilayer/substrate interface. In an effort to determine the cause of the extraneous Si peak, subsequent SIMS analysis revealed a carbon peak at the interface. Also shown in Figure 4.1 is the SIMS depth profile of carbon in the Ge epilayer, which shows that carbon is only present, in detectable levels, at the interface. This can be explained by

contamination of the Ge surface with both C and Si during the initialization of the MBE growth process. While this Si peak was unintended it still retained the possibility of revealing further information about Si diffusion in Ge, therefore diffusion experiments were carried out in these Ge structures.

Diffusion experiments were performed over the temperature range of 550 °C to 900 °C. The samples were diced into 5×5 mm^2 pieces. Each individual sample was sealed in a silica ampoule under 0.5 atm Ar, to aid thermal transport and to prevent oxidation, and annealed in a Lindberg/Blue resistance-heated tube furnace. A type-S, Pt-Rh, thermocouple was used to monitor the temperature. The ampoules were quenched in water to terminate the diffusion. Depth profiles for ^{28}Si and C were measured via SIMS on a Cameca 4f at MAS Inc using a primary beam of O_2^+ ions. (Sunnyvale, CA).

The diffusion coefficient of Si in Ge was determined by fitting a numerical simulation of a single one-dimensional Fick's Law diffusion equation using the as-grown SIMS profile as the initial Si distribution. The numerical simulation was performed using the partial differential equation solver ZOMBIE [Jüngling, 1985] with a concentration independent diffusion coefficient. Fitting of the simulation to the experimental SIMS data was achieved by a Modified Damped Least Squares non-linear parameter optimization technique (Levenberg-Marquart method) that was performed by the mathematical equation solver Profile [Ouwerling, 1989]. The fitting parameter was the Si diffusion coefficient.

Due to the decomposition of the Ge surface at high temperatures, all samples annealed above 700 °C were capped with a 50 nm thick layer of SiO$_2$. The SiO$_2$ cap layer was deposited via CVD at 450 °C in the Microlab at the University of California,

Berkeley by graduate student, Joanna Lai. AFM results after SiO_2 deposition and after annealing showed no significant increase in surface roughness. In order to reduce the complexity of the SIMS analysis, the SiO_2 cap layers were etched off prior to SIMS using a 49% HF solution for 1 minute. The HF etch did not affect the Ge surface.

Several interesting features were revealed in the SIMS depth profiles of the diffusion samples. Figure 4.2(a) and (b) presents the SIMS depth profiles of samples annealed at temperatures of 550 °C and 900 °C, respectively, along with best fit simulations of each profile.

From Figure 4.2(b) it appears that the Si peak at the Ge substrate/epilayer interface is trapped at that interface as the peak height is not affected by diffusion even at 900 °C. All of the diffusion profiles over the temperature range of 550 °C to 900 °C showed a Si peak at the Ge substrate/epilayer interface with the same height as the as-grown Si peak at that interface providing more evidence of Si trapping at that interface. The SIMS depth profile of carbon in the samples presented in Figure 4.1 shows a carbon peak at the Ge substrate/epilayer interface. The SIMS profiles of the annealed samples revealed that this carbon peak is unaffected by the diffusion anneals as well and may be responsible for the trapped Si at the Ge substrate/epilayer interface.
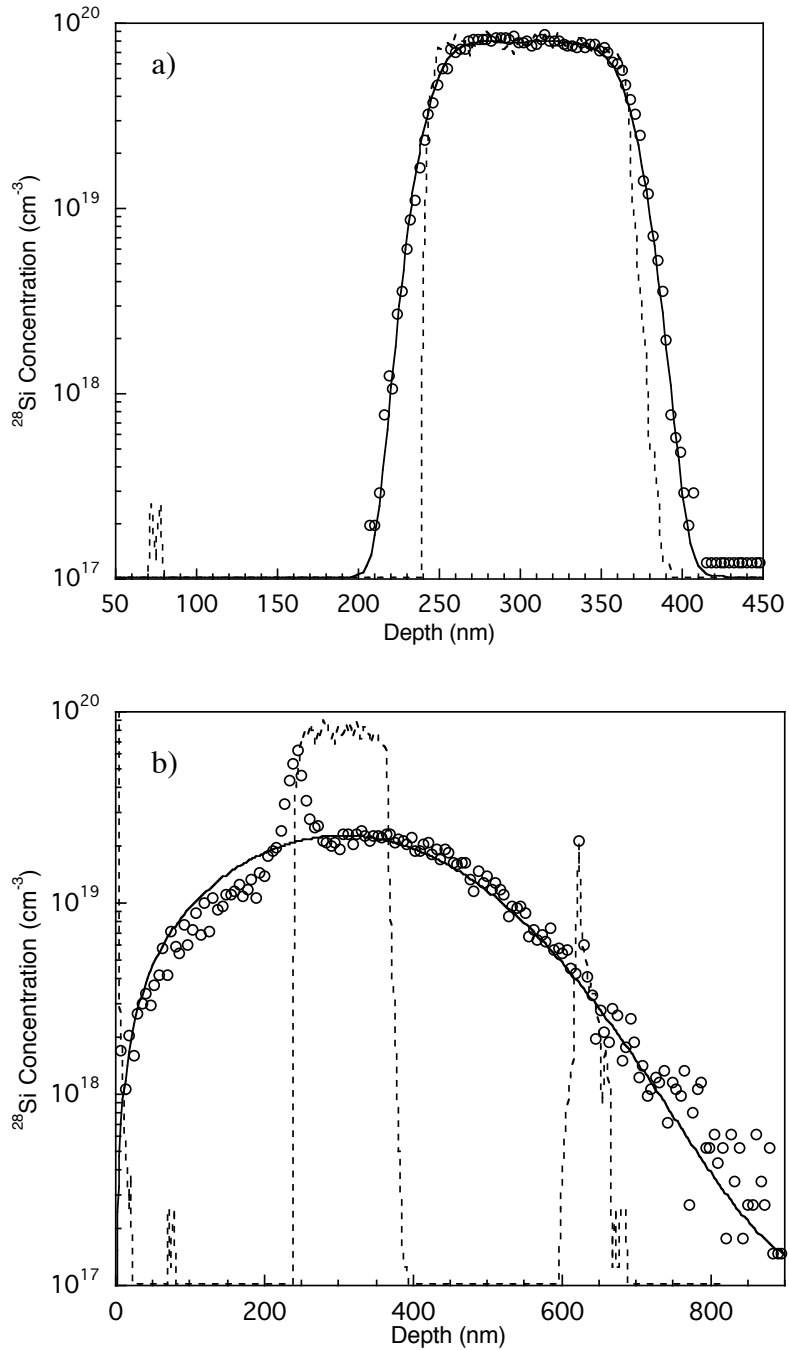
Figure 4.2 SIMS depth profiles of the Si doped Ge epilayer showing the as-grown structure (dashed line), the ^{28}Si SIMS concentration data (open circles), and best fit simulation (solid line). a) SIMS depth profile of sample annealed at 550 °C for 30 days, the substrate epilayer peak is not shown to allow detail of the primary profile. b) SIMS depth profile of sample annealed at 900 °C for 8 minutes, every second data point is shown for clarity.

Another interesting feature of Figure 4.2(b) is that of the Si spike present at a depth of 240 nm, which coincides with the top of the Si doped region, in the annealed sample. It appears that in this region as well, there is some amount of immobile Si that remains at the interface. From the fit to the 900 °C profile, the SIMS concentration data reveals a diffusion profile between this peak and the surface which is at a lower concentration than would be expected by the simulation, due to this region of immobile Si. This extraneous Si peak at the top of the Si doped region is observed in the samples annealed between 900 °C and 700 °C and is not observed in samples annealed at lower temperatures. The SIMS depth profiles in the samples showed no evidence of carbon at this interface. As can be seen from Figure 4.2, good fits of the simulation to the SIMS data using a single equilibrium diffusion coefficient are achievable, even with the extraneous Si peak.

Cross-sectional Transmission Electron Microscopy (TEM) experiments were performed at the National Center for Electron Microscopy, NCEM, at the Lawrence Berkeley National Laboratory by the group of Zuzanna Liliental-Weber, in an effort to determine if some crystal defects - dislocations, precipitates, etc. – are responsible for this extraneous Si peak. TEM images of an as-grown sample are shown in Figure 4.3. From Figure 4.3(a) it is evident that there are no structural defects present in the region around 240 nm below the sample surface, indicating that this peak is not caused by Si trapping at structural defects generated from the growth process. However, there are some dislocations present at the growth interface as illustrated by the white lines in the bright field TEM image. A high resolution TEM image of the growth interface, Figure 4.3(b), was taken to investigate the possible sources of Si trapping at this lower interface. Small clusters can be seen at the growth interface in the high-resolution image. Based on the

SIMS results showing Si and C at this interface that are highly immobile during diffusion we conclude that these clusters are most likely Si or SiC. Whatever the exact nature of these structures, the lattice plane images are continuous across the defects.

The SIMS depth profiles for C and the TEM of the as-grown structure have ruled out carbon contamination and structural defects as the cause of the Si trapping at the front of the Si buried layer (depth = 240 nm). Another possible cause for the trapped Si could be oxygen diffusion from the surface. The oxygen could be as a result of the SiO_2 cap layer or from residual oxygen in the ampoule during annealing. Discussions with Prof. Jan Talbot of UC – San Diego led to a simple diffusion calculation to examine the possibility of oxygen diffusion being the cause of the trapped Si. The diffusivity of O in Ge at 900 °C was calculated from the temperature dependence given in literature [Corbett, 1964] to be 4.66×10^{-10} cm^2/s, yielding a diffusion length of 4.7 µm for the sample annealed at 900 °C for 8 minutes. Therefore, if O were present, it certainly would reach the Si layer at 240 nm. As a result of the large diffusion length of O in Ge at this temperature, one may assume that in the 240 nm distance from the surface to the Si layer a steady-state diffusion of O is maintained and Fick's First Law may be used (see Equation 1.1 of Section 1.1). If all of the oxygen is assumed to be trapped at the Si interface and the surface concentration is assumed to be the solubility of O in Ge during vacuum growth, 6×10^{-16} cm^{-3} [Thurmond, 1956], the concentration gradient across this region can be calculated. This yields a flux of 1.2×10^{12} atoms/$cm^2 \cdot$s at the Si layer interface. For the 8-minute anneal, a total of 5.6×10^{14} oxygen atoms/cm^2 would reach the Si layer. A calculation of the area under the trapped Si peak in Figure 4.2(b) yields a value of 2.7×10^{14} silicon atoms/cm^2 trapped at this interface. The close agreement

88

between the amount of trapped silicon and the amount of oxygen that could diffuse from the surface gives an indication that oxygen may be responsible for the Si trapped at a depth of 240 nm. Further SIMS experiments on O in the structures would be required to confirm this analysis.
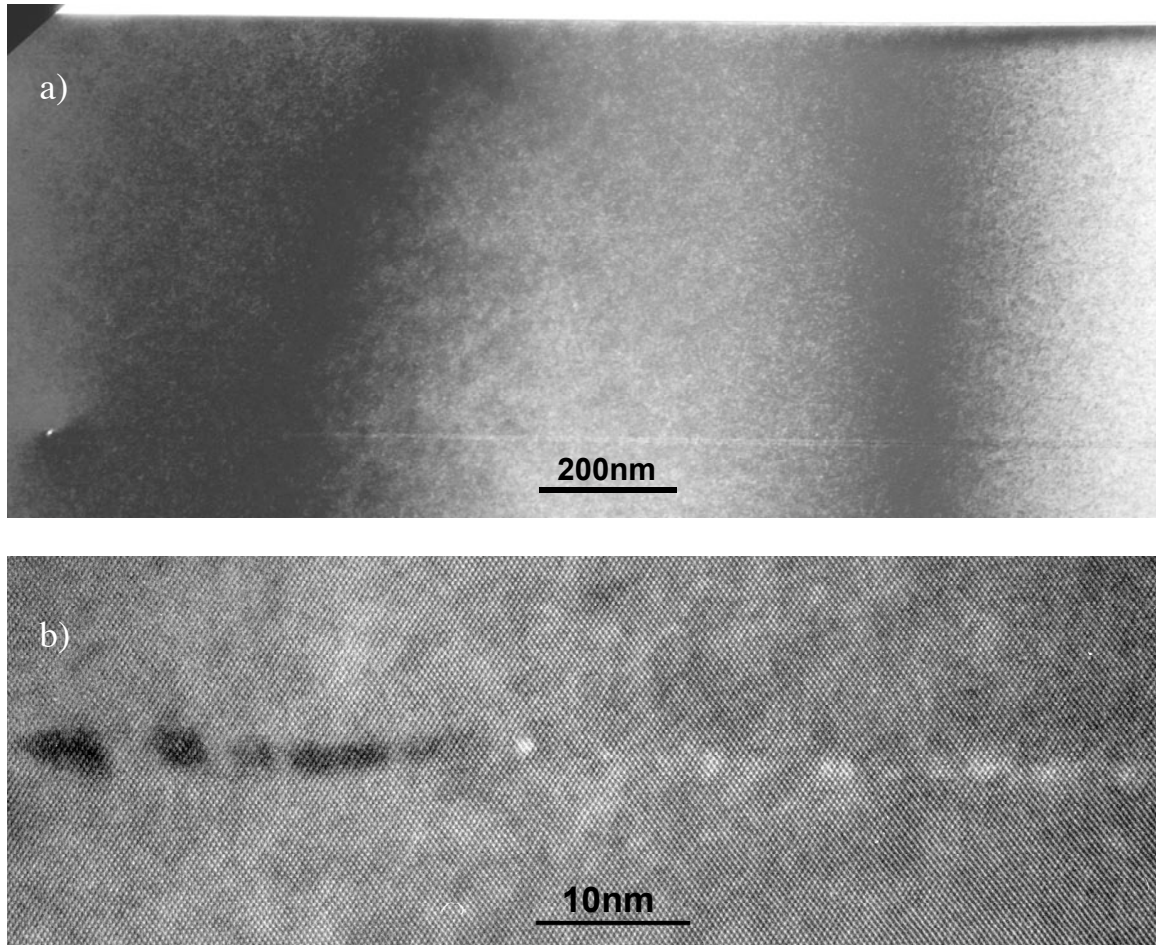
Figure 4.3 Cross-sectional Transmission Electron Microscopy (TEM) images of an as-grown Ge epilayer containing a buried Si doped layer. a) a bright field image of the epilayer with sample surface at the top of the image and the growth interface indicated by the dislocation lines (white). The lack of any structural defects beyond the growth interface excludes structural defects as the source of the Si SIMS peak at 240 nm. b) a high resolution TEM image of the growth interface showing the presence of clusters at the growth interface. [Courtesy of Z. Liliental-Weber and D. Zakharov]

The diffusion coefficients of Si in Ge, determined from the best-fit simulations of the

SIMS data, are plotted as a function of inverse temperature in Figure 4.4. Also included

in Figure 4.4 are lines representing the temperature dependencies of previous

measurements of the diffusion coefficient of Si in Ge from literature.

Figure 4.4 Plot of the diffusion coefficient as a function of inverse temperature. The open circles are data points from current work; the solid line is a fit to the data points. Dashed lines represent temperature dependencies reported in literature over the appropriate temperature ranges.

From the above plot, it is clear that the results from the current set of experiments exceed the temperature range over which diffusion coefficients of Si in Ge have been reported in the literature. The range of values of the diffusion coefficient exceeds the published values by 2 orders of magni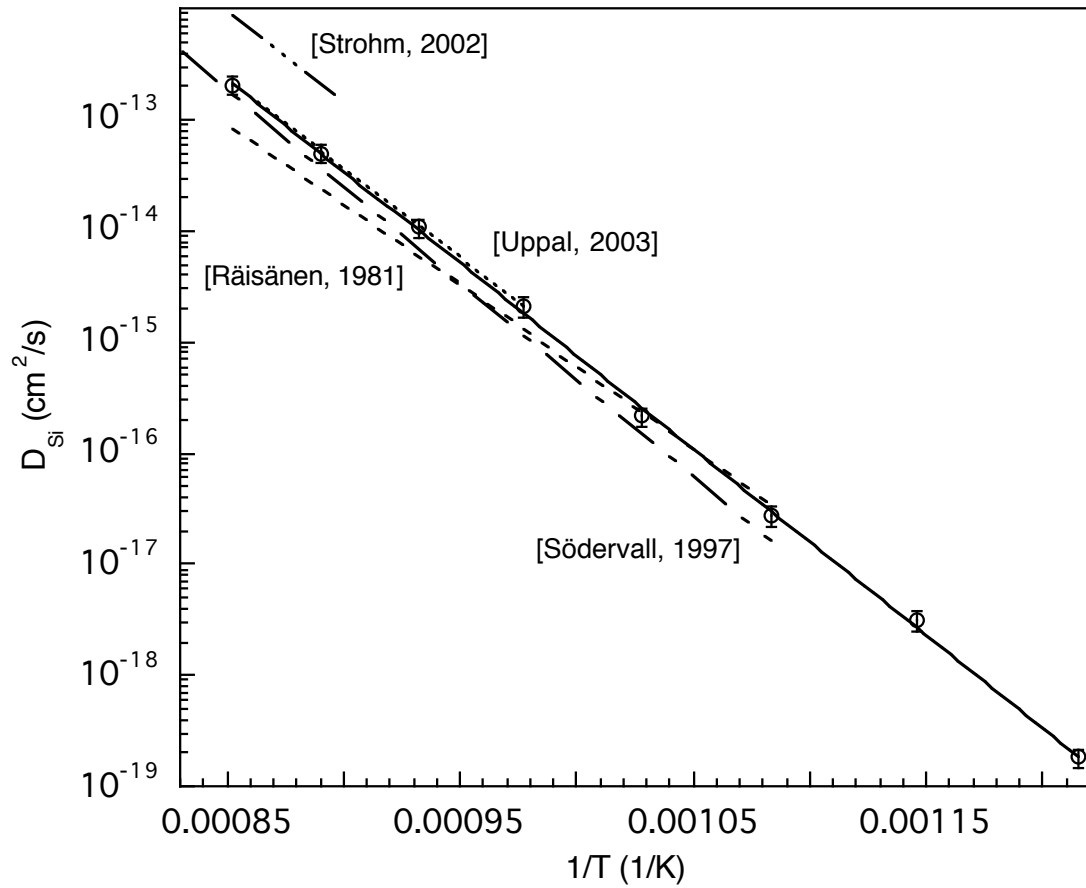tude. The temperature dependence of the Si diffusion coefficient in Ge was found from this work to have an activation energy of 3.32 ± 0.1 eV and a pre-factor, D_o, of $38_{-27.4}^{+71.5}$ cm^2/s. A comparison of the values from the current work and those of previous experiments is presented in Table 4.1. The pre-factor and activation energy agree reasonably well with the values from literature with the current activation energy value of 3.32 eV falling in between the values determined previously. One of the primary motivations for employing a buried Si layer in the experimental approach is to prevent any non-equilibrium effects that could result from implantation or sputter deposition. It should be noted that all of the activation energies that fall below the present value were achieved from implanted sources, leaving open the possibility that implantation damage has caused an enhancement in the diffusion coefficient, resulting in a lower activation energy. However, the present value and literature values are all consistent within the errors presented by the authors.

Table 4.1 Comparison of the values for the temperature dependence of Si diffusion in Ge from literature and present work. Values are also plotted in Figure 4.4.

Temperature range (°C)	D_o (cm^2/s)	E_a (eV)	Experimental technique	Reference
650-900	0.24	2.9	Implantation, (p,γ) resonance	[Räisänen, 1981]
650-930	140	3.47	Sputter deposition, SIMS	[Södervall, 1997]
843-904	43	3.19	Radiotracer, ion beam sectioning	[Strohm, 2002]
750-890	9.7	3.18	Implantation, SIMS	[Uppal, 2003]
550-900	38	3.32	Buried Si, SIMS	present work

Finally, in comparing the diffusion coefficient of Si in Ge with Ge self-diffusion, one finds the both the pre-factor and activation energies to be reasonably close to that of Ge self-diffusion (D_o = 13.6 cm^2/s, E_A = 3.09) [Werner, 1985]. This leads to the conclusion that the mechanism of Si diffusion in Ge is similar to that of Ge self-diffusion, i.e., – vacancy mediated. In looking toward how these results fit into the SiGe alloy system it is noteworthy that for pure Si, the activation energy of Ge in Si (4.65 eV [McVay, 1975]) is lower than that of Si self-diffusion (4.75 eV) while for pure Ge the activation energy of Si in Ge (3.32 eV, present work) is greater than the activation energy for Ge self-diffusion (3.09 eV [Werner, 1985]). The observation of a higher activation energy for Si diffusion in both Ge and Si compared to that of Ge diffusion is most likely due to the larger bond strength of Si compared to Ge resulting in a greater energy required for the formation of a mobile Si species.

The establishing of the end point value (x=1) for diffusion of Si in the $Si_{1-x}Ge_x$ alloy system is an important first step in the study of the mechanisms of diffusion in SiGe. The future work on this project will yield simultaneous Si and Ge self-diffusion in SiGe throughout the composition range, and how these values vary in comparison to the end points of diffusion in pure Si and pure Ge will help to determine the mechanisms of diffusion.

5   Conclusions

5.1   Summary

An isotopically enriched heterostructure of natural and ^{28}Si has been used to
observe and measure simultaneous self- and dopant diffusion in Si. The dopants B, As,
and P were chosen for this study as a means to alter the native defect charge state under
extrinsic doping (n- and p-type) and to investigate the role of the native defects in the
mechanisms of diffusion for the chosen dopants. This technique of simultaneous dopant
and self-diffusion presents a unique approach to the study of native defect properties and
diffusion mechanisms in semiconductors.

The simultaneous diffusion of B and Si in the Si isotope heterostructure yielded a
model for B diffusion based on the kick-out mechanism involving neutral B interstitials
and both neutral and singly positively charged Si self-interstitials. The interstitialcy
mechanism for B diffusion was ruled out due to the low value of the correlation factor (f_{BI}
≤ 0.3) that would be required by the model for an accurate fit. These experiments also
revealed the contribution of the positively charged self-interstitial to Si self-diffusion.

The experiments on the simultaneous diffusion of As and Si in the Si isotope
heterostructure generated a model for As diffusion via the interstitialcy and vacancy
mechanisms involving a neutral and a singly negatively charged native defect and neutral
arsenic-vacancy and arsenic interstitial pairs. While the model for As diffusion could not
conclusively determine whether the singly negatively charged defect was a vacancy or
interstitial defect, the close agreement of the activation energy of the defect from As

93

diffusion and the singly negatively charged self-interstitial derived from the P diffusion experiments revealed that it was indeed the I⁻ defect involved in the As diffusion, along with a neutral vacancy. A consistent contribution of the I⁻ defect to Si self-diffusion was derived from both the As and P diffusion experiments. No evidence of the involvement of a doubly negatively charged native defect could be obtained from the model.

The simultaneous P and Si diffusion experiments produced a model for P diffusion in Si involving neutral and singly negatively charged interstitials in a kick-out or interstitialcy mechanism and neutral vacancies in a dissociative or pair diffusion mechanism. The model requires the existence of a singly positively charged mobile P species along with a neutral P species to properly reproduce the experimental profiles. As in the case of the simultaneous As and Si diffusion experiments, the model for P and Si simultaneous diffusion yields no evidence for the involvement of a doubly negatively charged native defect.

From the experiments on the simultaneous diffusion of Si and the dopants B, As, and P, the total Si self-diffusion due to interstitials was accurately reproduced by the sum of the contributions of the neutral (B, P experiments), singly positively charged (B experiment), and singly negatively charged (As, P experiments) self-interstitials.

As an initial phase in the study of self-diffusion in SiGe alloys, the diffusion coefficient of Si in Ge was determined using a buried Si-doped layer in a MBE grown Ge epilayer over the temperature range of 550 °C to 900 °C. An activation energy of 3.32 eV for Si diffusion in Ge was found to be within the range of previous literature values; however, the temperature range over which the value was determined exceeded any

94

previous experiments, yielding a measured variation in the diffusion coefficient with temperature of six orders of magnitude.

5.2 Future Work

While the research on dopant and self-diffusion in Si has fulfilled the goal of determining the mechanisms of diffusion of the dopants as well as the contributions of the various native defect charge states, the measurement of the diffusion coefficient of silicon in germanium (described in Chapter 4) is only in the initial phase of an extensive research collaboration to study the diffusion in SiGe alloys. The collaboration will involve the growth of various isotopically enriched $Si_{1-x}Ge_x$ structures by the research group of Arne Nylandsted Larsen at the University of Aarhus in Denmark. The research group in Berkeley, along with the group of Dr. Hartmut Bracht at the University of Münster in Germany, and the group in Denmark will perform the diffusion experiments and analysis jointly. The primary goal of the collaboration on SiGe diffusion is to determine the physics of the mechanisms dominating self- and dopant diffusion in $Si_{1-x}Ge_x$ over the full composition range for relaxed as well as strained layers. To that end, a series of isotopically enriched multilayer structures have been proposed to study the various properties of diffusion in $Si_{1-x}Ge_x$.

After having established the diffusion coefficient of silicon in germanium in this thesis, which represents Si diffusion in a $Si_{1-x}Ge_x$ alloy with x = 1, the plan is to evaluate silicon and germanium self-diffusion in relaxed $Si_{1-x}Ge_x$ alloys over the whole composition range. In order to attain this goal, a sequence of $Si_{1-x}Ge_x$ layers will be grown via MBE to form the structure shown in schematically in Figure 5.1.

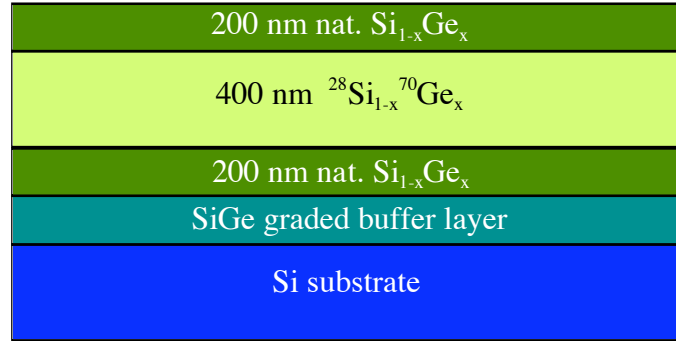**Figure 5.1** Diagram of the proposed structure for measuring the simultaneous diffusion of Si and Ge in $Si_{1-x}Ge_x$ alloys. The structure consists of MBE grown epilayers ($^{nat}Si^{nat}Ge$ (200 nm)/$^{28}Si^{70}Ge$ (400 nm)/$^{nat}Si^{nat}Ge$ (200 nm)) on a Si substrate. The $Si_{1-x}Ge_x$ layers are grown on a SiGe graded buffer layer to obtain relaxed structures.

The enriched $^{28}Si^{70}Ge$ layer in the middle of the structure is depleted of the isotopes ^{29}Si, ^{30}Si, ^{72}Ge, ^{73}Ge, ^{74}Ge and ^{76}Ge allowing for the simultaneous measurement of silicon and germanium diffusion in $Si_{1-x}Ge_x$ alloys over a wide temperature range by monitoring the diffusion of any of the aforementioned Si and Ge isotopes from the two natural composition layers into the $^{28}Si^{70}Ge$ enriched layer. As with the previous experiments described in this work, the diffusion profiles will be measured experimentally via Secondary Ion Mass Spectrometry (SIMS). Since one of the project goals is to determine the composition dependence of the diffusion properties in $Si_{1-x}Ge_x$ alloys, experiments with structures where $x = 0.05, 0.15, 0.25, 0.35, 0.45, 0.55, 0.70$ and 0.85 are planned. The epilayers will be deposited on a Si substrate using graded buffer layers to form stress-free, relaxed structures.

The next phase in the SiGe diffusion research will be to use the Si and Ge self-diffusion results to aid in the analysis of simultaneous dopant and self-diffusion experiments in $Si_{1-x}Ge_x$ alloys. This work will be similar to the simultaneous dopant and Si self-diffusion work presented in Chapter 3, and should yield information on the type

and charge state of the native defects involved in dopant diffusion. A multilayer

structure, like that depicted in Figure 5.2, consisting of 5 pairs of enriched and natural $\text{Si}_{1-x}\text{Ge}_x$ layers will be grown via a SiGe graded buffer layer on a Si substrate. The thickness

of the individual $^{nat}\text{Si}^{nat}\text{Ge}$ and $^{28}\text{Si}^{70}\text{Ge}$ layers will be 100 nm. A 200 nm thick

amorphous natural SiGe cap will be deposited on top of the structure. The acceptor

dopant boron and donor dopants phosphorus and arsenic will be introduced into the

amorphous SiGe cap layer via ion implantation. This method of dopant introduction has

been shown in Section 2.1.1 not to influence the equilibrium native defect concentrations

through implantation damage. The same set of compositions as those listed for Si and Ge

self-diffusion in $\text{Si}_{1-x}\text{Ge}_x$ will be studied. The end point composition of $x = 1$ (pure

germanium) will be explored in order to obtain accurate dopant and self-diffusion data in

germanium.

200 nm amorphous SiGe cap

100 nm $^{28}\text{Si}_{1-x}^{70}\text{Ge}_x$

100 nm nat. $\text{Si}_{1-x}\text{Ge}_x$

SiGe graded buffer layer

Si substrate

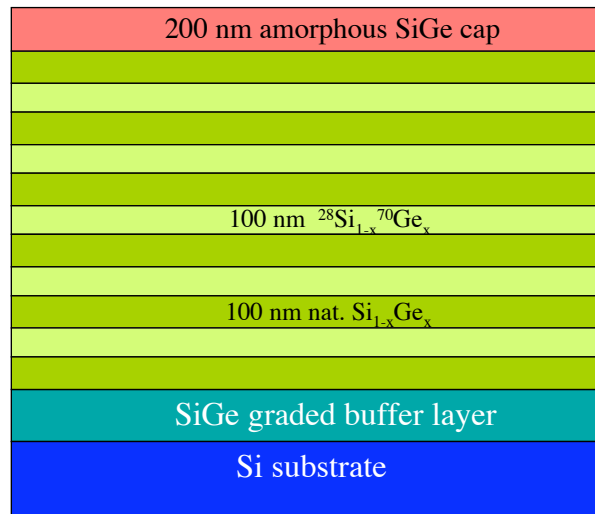**Figure 5.2** Diagram of the proposed structure for observing simultaneous dopant and self-diffusion in $\text{Si}_{1-x}\text{Ge}_x$ alloys. The structure contains alternating 100 nm thick layers of natural and enriched $\text{Si}_{1-x}\text{Ge}_x$, grown on a Si substrate using a SiGe graded buffer layer. The amorphous SiGe cap layer is to allow introduction of dopants via implantation without generation of excess native defects.

The final aspect of diffusion in $Si_{1-x}Ge_x$ alloys to be investigated is the effect of strain on dopant and self-diffusion. The theoretical understanding is very limited, and it is expected that the high quality of experimental data achievable using stable isotope structures may yield the development of an appropriate theory describing the effects of strain on diffusion in $Si_{1-x}Ge_x$ alloys. As an initial experiment, the proposed research calls for the measurement of the self-diffusion of Si and Ge in strained $Si_{1-x}Ge_x$ layers with varying compositions. The proposed structure is shown in Figure 5.3 and will consist of a 200 nm thick enriched $^{28}Si_{1-x}^{70}Ge_x$ layer, grown between two 100 nm natural composition $Si_{1-y}Ge_y$ layers. The isotopically enriched layer will have x larger or smaller than y in the adjacent layers. This will lead to compressive strain for $x-y < 0$ and to tensile strain for $x-y > 0$. The difference in composition between the layers will be kept to 5% since too large a strain would cause relaxation of the films. The structure will be grown on a graded SiGe buffer layer to eliminate stress from the underlying Si substrate. The investigation of the following combinations of composition, in percent, are proposed: (x, y) = (15, 10); (15, 20); (35, 30); (35, 40); (55, 50); (55, 60); (75, 70) and (75, 80).

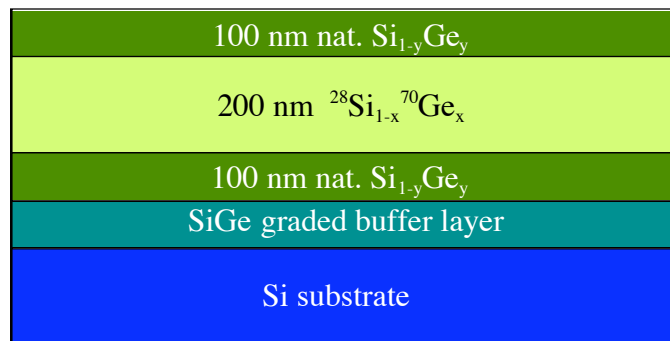| 100 nm nat. $Si_{1-y}Ge_y$ |
| :---: |
| 200 nm $^{28}Si_{1-x}^{70}Ge_x$ |
| 100 nm nat. $Si_{1-y}Ge_y$ |
| SiGe graded buffer layer |
| Si substrate |

Figure 5.3 Diagram of the proposed structure for measuring the effect of strain on Si and Ge self-diffusion in $Si_{1-x}Ge_x$ alloys. The difference in composition between x and y will lead to compressive strain for $x-y < 0$ and to tensile strain for $x-y > 0$.

Appendices

Appendix A: Secondary Ion Mass Spectrometry

A.1 Introduction

The purpose of this appendix is to introduce the reader to the fundamental aspects of Secondary Ion Mass Spectrometry (SIMS). First, the physical phenomena that occur during SIMS will be discussed, followed by the theoretical models used to describe the SIMS process. The instrumentation used in modern SIMS instruments will be detailed and finally, the specific requirements of the application of SIMS to depth profiling will be presented.

Most of the details of this appendix are taken from *Secondary Ion Mass Spectrometry: Principles and Applications* by Vickerman, Brown, and Reed [Vickerman, 1989]. For more information on the SIMS technique the reader may also wish to consult the book by Benninghoven, et al. [Benninghoven, 1987].

SIMS is a characterization technique that utilizes an energetic source of primary ions to bombard a surface, generating secondary ions from the surface. These secondary ions are then mass analyzed to determine the elemental species and composition of the surface layer of the material. Depth profiles of a material can be generated by allowing the ion bombardment to continue, causing the removal of material, and subsequently analyzing the secondary ions as a function of the depth of the crater formed by the ion sputtering.

J.J. Thomson first observed the emission of positive secondary ions from a metal surface in a vacuum tube in 1910 [Thomson, 1910]. But it was not until 1949 that the first SIMS instrument was built and recorded secondary ion mass spectra from metals and oxides [Herzog, 1949]. The first instruments were all designed for dynamic SIMS, or the continual removal of material for depth profiling; this was highly destructive to the sample surface. The development of static SIMS as a sensitive surface analysis technique capable of determining surface chemistry was enabled by the work of Benninghoven, who used a very low current density primary ion beam to increase the surface monolayer lifetime [Benninghoven, 1970]. Advances in instrumentation, which will be discussed further in Section A.4, improved the sensitivity of the various SIMS techniques.

A.2 Experimental Parameters of SIMS

The basic phenomenon of the SIMS process involves the impact of the primary ions on the surface and the penetration of the primary ion into the material transferring energy to the matrix atoms in a series of collisions until the primary ion loses all its kinetic energy. The series of collisions of matrix atoms, initiated by the penetration of the primary ion, propagates to the surface as well as into the bulk of the material. It is this collision cascade that is responsible for the emission of low energy secondary ions and particles from the surface of the material. Figure A.1 is a schematic diagram of the SIMS process showing the penetration of the ion, the collision cascade and the emission of secondary ions and clusters of ions and neutrals.
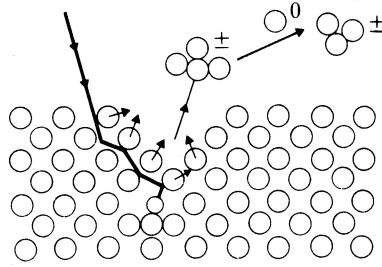
Figure A.1 A diagram of the SIMS process illustrating the collisions that occur upon primary ion impact and the resulting surface emission of secondary ions, clusters and neutral particles.

In this section the experimental parameters of the SIMS process; sputter rate, ionization probability, and surface charging; will be discussed. The subsequent section, Section A.3, will focus on the theoretical models used to describe the emission of secondary ions from a surface.

<u>Sputter Rate</u>

The primary parameter for determining the sputter rate is the monolayer lifetime of the surface [Vickerman, 1989]:

$$t_m = \frac{N_S}{\left(6.2 \times 10^{18}\right)I_p Y} \tag{A.1}$$

where t_m is the monolayer lifetime, N_S is the density of atoms on the surface, I_p is the primary ion current, and Y is the sputter rate or the number of secondary ions removed per primary ion impact. The value of 6.2×10^{18} is 1/e, where e is the charge of an electron, equal to 1.6×10^{-19} C.

The sputter rate, Y, is dependent on both the parameters of the primary beam and the target material. The sputter rate increases with the energy and particle mass of the

primary beam, however for most materials there is a maximum of 1 to 10 secondary particles emitted for every primary particle impact at high energies. The angle of incidence of the primary beam also affects the sputter rate. The maximum sputter rate is achieved for an angle of 70° with respect to the sample normal. This is a result of most of the energy being deposited in the surface layers for such a large angle of incidence. The charge of the ions in the primary beam plays little role in the sputter rate of metals, since charged ions will be neutralized at impact. However, for poor conductors, like semiconductors and insulators, charged ions in the primary beam will increase the sputter rate.

There are many aspects of the target material that will affect the sputter rate. The crystallinity and orientation of the sample affect the sputter rate due to channeling of the ion beam. Close-packed planes show a higher ion yield than do planes such as (100) and (110) [Roosendaal, 1981]. A high surface roughness, comparable with that of the ion cascade, leads to a higher yield than for flat samples [Littmark, 1978]. For multi-element samples, a preferential loss of one component may be observed. In general the species with the highest ion yield in elemental form will have the highest ion yield as a component.

Ionization Probability

The sputter yield from the surface described in the previous section is an important parameter, however SIMS measures the yield of secondary ions, so the ionization probability of a sputtered particle is even more important for a technique such

as SIMS. The current of secondary ions from the surface is related to the sputter rate and

ionization probability by the equation [Vickerman, 1989]:

$$i_s^M = I_p Y \alpha^+ \theta_M \eta \qquad (A.2)$$

where i_s^M is the secondary ion current of the species M, I_p is the primary ion flux, α^+ is

the ionization probability, θ_M is the fractional concentration of M in the surface layer,

and η is the transmission of the system, which is an instrumental parameter dependent on

the type of mass analyzer used.

There is an inverse dependence between the ion yield, which is the product $Y\alpha^+$,

and the ionization potential of the element. The ionization potential increases along the

periods (left to right) of the Periodic Table. Therefore, the ion yield of Al is greater than

that of Si.

Positive ion yields are increased by the presence of electronegative species such

as oxygen on the surface. This is due to an increase in the work function of the surface

and the increased probability of positive ion escape from the surface as a result. The ion

yield of positive Si ions from a Si surface has been shown to increase under flowing

oxygen during analysis [Maul, 1975]. The increased ion yield will lead to greater

sensitivity. Due to this greater sensitivity, oxygen is an often used primary beam species,

either as O^- or O_2^+. The oxygen primary beam will react with the surface and increase the

ion yield for positive ions. The reactive species, Cs^+ is used if a large negative ion yield

is desired due to its high electropositivity.

Surface Charging

In general, the SIMS process involves the bombardment of a surface with positive ions, resulting in the emission of secondary ions, neutral particles, and secondary electrons. In the case of SIMS analysis of insulating materials, the large difference in the number of neutral particles and secondary electrons emitted compared to secondary ions will result in the surface of the material becoming positively charged. This can cause problems for SIMS analysis since the positive surface will give a larger accelerating potential to the positively charged secondary ions, accelerating the ions past the energy range of the analyzer. The emission of negatively charged ions can be retarded by a positively charged surface. To overcome this problem, electron bombardment of the surface from a low energy electron beam (10 eV) is often performed in conjunction with the SIMS analysis, to lower the surface potential.

There are many other experimental aspects of SIMS analysis that are specific to the use of dynamic SIMS for depth profiling. These parameters will be discussed in Section A.5, which is assigned to the description of SIMS for depth profiling.

A.3 SIMS Theory

A general description of the SIMS process involves primary energetic ions striking a sample surface. Some ion energy will be lost to electronic excitation, but most is lost via a nuclear stopping mechanism. Collision cascades occur in the near surface region due to the hard-sphere collisions of the nuclear stopping mechanism. A fraction of the collision cascades will return to the surface, resulting in the emission of secondary

ions, and sputtering of the surface. The emission cascades occur within the first 1-2 nm of the surface while lattice damage due to collisions can extend 10-25 nm below the surface as depicted in the illustration in Figure A.2. The two primary processes occurring during SIMS are emission and ionization of the secondary particles. In this section, some of the theoretical models used to describe the emission and ionization processes under primary ion bombardment are presented.
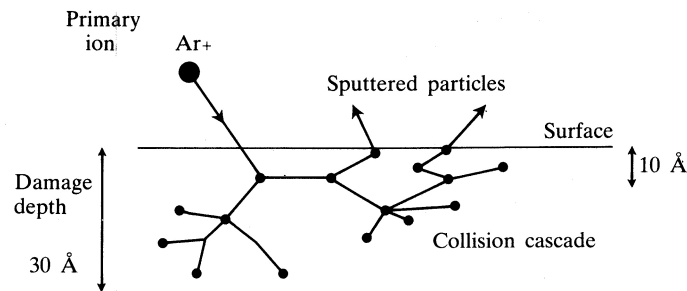
Figure A.2 An illustration of the SIMS process, showing the primary ion impact, the depth of ion beam damage, the induced collision cascades and the secondary ions emitted from the surface. [Vickerman, 1989]

Sputtering Models

The models used to describe sputtering are very complex due to the many-body problem of energetic incident ions bombarding a sample surface and displacing the matrix atoms in a series of collisions. The simplest model for sputtering is to interpret it as a series of hard-sphere collisions. In this approach, the classical energy transfer equations are used and no assumptions are made regarding the structure or geometry of the solid. The linear collision cascade theory is one such approach for modeling the sputtering process. In the linear collision cascade theory only the elastic collisions of primary ions interacting with the nuclei of the solid are taken into account. The inelastic interactions of the primary ions with the electrons of the solid are neglected. Finally, a

106

surface barrier energy, U, is used to describe the energy required to remove an atom from the surface. This energy barrier is usually related to the sublimation energy of the material. The energy of the primary ion must be substantially larger (~4U) than the surface barrier energy in order for sputtering to occur. Below this threshold energy, the collision cascade induced by the primary ion impact will not generate secondary particles with enough energy to escape the surface.

Ionization

Due to the impact of the primary ion beam in the near surface region, the crystalline structure of the solid becomes disordered. Therefore models for the ionization of particles from the surface should use a continuum of energy states associated with an amorphous material rather than the band structure of a crystalline solid.

The perturbation model of ionization takes into account the atom surface coupling. Much in the same way that the linear cascade theory described above makes use of a surface barrier energy for sputtering that is proportional to the sublimation energy, the perturbation model for ionization makes use of the difference between the ionization potential and the work function as the barrier for ionization. Accordingly, the ionization probability is given by the following expression [Blaise, 1979; Nørskov, 1979]:

$$\alpha^+ \propto e^{\left(-\frac{I-\psi}{Cv}\right)}$$ (A.3)

where α^+ is the ionization probability, I is the ionization potential, and ψ is the work function of the material. The velocity of the departing atom is represented by v, and C is a constant.

Although the models presented here are rather simple, they are effective in describing the SIMS process, and yield a framework to enable quantitative analysis of the parameters involved during SIMS.

A.4 SIMS Instrumentation

As illustrated in Figure 2.3 of Section 2.1.2, the primary components of a SIMS instrument are the ion gun and the mass spectrometer. In this section the types of ion guns and mass spectrometers used in SIMS will be described. The advantages of particular types of components for specific applications will also be presented.

An additional important component to the SIMS instrument is a vacuum system. The SIMS process must occur under vacuum for two reasons, first and foremost to prevent scattering of the ion beams. The pressure in the chamber must be low enough such that the mean free path for an ion is longer than the beam path. A pressure of 10^{-5} mbar is usually sufficient to achieve this condition. The second reason for a vacuum system is to prevent adsorption of gases on the sample surface during analysis. Since static SIMS is designed as a very sensitive method to measure the atoms on the surface of a material, a very low base pressure is needed, $\sim 10^{-10}$ mbar. Dynamic SIMS, on the other hand, sputters the surface more rapidly so it is less sensitive to adsorbed gases, and therefore has less rigorous pressure requirements. The exception for dynamic SIMS occurs when the detection of an element that exists both in the material and in the residual gas, is desired, i.e., – H, O, N. A high residual gas pressure in the system will

yield a high background concentration of the desired species and reduce the sensitivity of the measurement.

Ion guns

The appropriate design of the ion gun depends on the primary beam requirements of the desired application. In static SIMS, the ion beam should be relatively broad, with a beam diameter of 1 mm to 1 cm and a current of 10^{-10} to 10^{-8} A at a primary particle energy between 0.5 and 5 keV. This results in a monolayer lifetime on the order of 100 s, allowing for sensitive analysis of the sample surface. For dynamic SIMS, the monolayer lifetime should be less than 1 second to allow for reasonable etch rates. This requires a beam current on the order of 10^{-6} A with energy near 5 keV.

Regardless of the SIMS application, all ion guns consist of two primary components, an ion source, and a lens to extract the ions. The ion beam energy is determined by the potential difference between sample and the ion source. Generally the sample is held at ground potential and the source is floated to the appropriate potential to generate the desired ion beam energy. In many cases a lens is added after the extraction of the ions to focus the beam on the sample. If rastering of the beam on the sample surface is desired, x-y scanning plates can be added to the ion gun.

There are several types of ion guns that are useful in a variety of applications. The electron bombardment plasma source uses a filament and generates electrons from the filament either by thermionic emission or positive ion bombardment. The electrons generated by the cathode filament are accelerated to the anode in the presence of the feed gas from which the ion beam is desired. A plasma is produced by the interaction of the

energetic electrons and the gas. An electric field is used to extract the ions from the plasma to form the ion beam. The use of inert gases in the source, i.e., – Ar or Xe, along with a heated filament, creates an ion gun capable of static SIMS. If dynamic SIMS for depth profiling is required, then a reactive ion such as O_2^+ or Cs^+ is needed, and the ion bombardment cold cathode is used, given that a hot filament would react with the gas.

Another type of ion source is the field ionization or surface ionization source. These instruments make use of electron tunneling that will occur from atoms on or near a metal surface with a high electric field. To increase the field and therefore increase the rate of electron emission and ion production, the metal surface is usually fashioned into a fine tip. The ions are generated from the tip region. Liquid metals, like Ga, in contact with the tip will produce ions, as will gas sources which adsorb atoms on the metal tip surface.

Mass spectrometers

After the ion beam has been generated by the source and impacts the sample surface producing secondary ions, the next major component of the SIMS instrument is the mass spectrometer. The mass spectrometer consists of the mass analyzer followed by an ion detector to count the ions selected by the analyzer. The ion detector in most cases is an electron multiplier, however, if imaging is required a channel plate and phosphor screen can be used.

The mass analyzer is generally either a quadrupole or a magnetic sector instrument. The quadrupole mass analyzer functions by setting the ion in an oscillatory motion down the length of the analyzer, by virtue of the electric fields in the system. A

110

schematic illustrating the principles of a quadrupole mass analyzer is reproduced from

Section 2.1.2, as Figure A.3. A quadrupole mass spectrometer consists of 4 symmetric

rods, with one pair of rods fixed perpendicular to the other pair of rods. Each pair of rods

is held at a d.c. voltage with a radio frequency (rf) a.c. voltage superimposed on it. One

pair is maintained at a positive d.c. voltage and the other pair is kept at a negative d.c.

voltage. The rf voltage on the two pairs of rods are 180 degrees out of phase with one

another. As the ion passes down the center of the analyzer axis, it undergoes oscillations

due to the varying rf field. Selection of the proper rf to d.c. voltage ratio results in the

ions of the desired mass passing through the instrument un-deflected while ions of all

other masses are scattered into the rods (see left side of Figure A.3). All ions that are

below the selected mass are scattered into the positive pair of rods, while all ions above

the selected mass are neutralized on the negative pair of rods. Mass selection is

dependent only on the voltages applied to the rods; therefore rapid switching between

different masses is readily achieved. Mass selection obtained from a magnetic sector

spectrometer requires changing the magnetic field for different mass ions. Therefore,

larger energies and time constants are needed to achieve mass switching in a magnetic

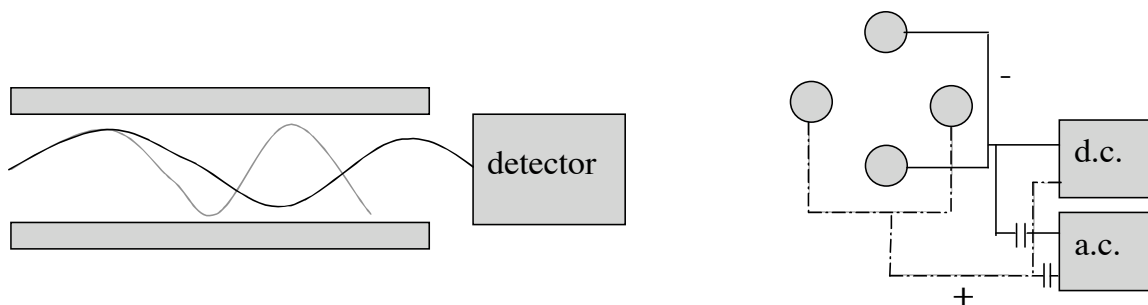sector than for a quadrupole mass spectrometer.

Figure A.3 A schematic diagram of a quadrupole mass spectrometer (left) showing the path of an ion of the selected mass (black line) and a scattered ion (gray line). The right side shows a diagram of the voltages applied to the four rods.

The magnetic sector mass analyzer functions on the motion of a charged particle in a magnetic field. The charged particle will experience the Lorentz force, $\vec{F} = q\left(\vec{v} \times \vec{B}\right)$, where the force is perpendicular to the direction of the charge particle velocity, v, and the magnetic field, B. The particle is then deflected by the force and undergoes a circular orbit with a radius of orbit dependent on the velocity of the particle. If all ions are accelerated to the same potential before entering the analyzer then the velocity and resulting path radius are dependent on the mass/charge ratio of the ion. This relationship is described by Equation A.4:

$$R = \frac{1}{B}\left(\frac{2mV}{z}\right)^{1/2} \tag{A.4}$$

where R is the radius of the ion path, B is the magnitude of the magnetic field, V is the accelerating potential, and m/z is the mass/charge ratio. As is evident from Equation A.4, since the accelerating potential and magnetic field are parameters of the system that can be set, it is the mass/charge ratio that determines the radius of the ion path. The ions can then be spatially separated by mass by the amount of deflection they undergo in a given

magnetic field. The placement of an aperture at the end of the analyzer in front of the ion

detector will create a single fixed radius for passage through the analyzer. Any ion not

traveling on the proper deflection path will not pass through the aperture, as can be seen

in the diagram depicting a magnetic sector mass analyzer in Figure A.4. This allows for

the use of the magnetic field of the analyzer as the selection tool for the proper

mass/charge ratio of the ion to be detected. Higher mass resolution is achieved by the use

of a longer path and therefore requires a larger magnet.
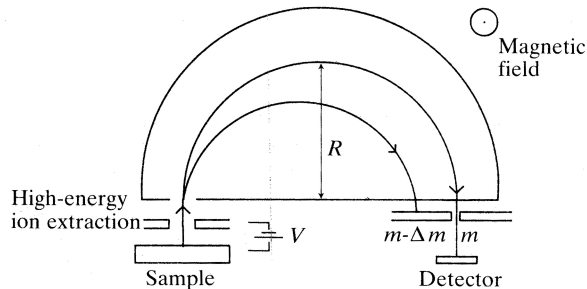

Figure A.4 Diagram of the mechanism by which a magnetic sector mass analyzer
separates ions of varying mass. In a perpendicular magnetic field, only the ions of mass,
m, will undergo a path of radius, R, in accordance with Equation A.4, and exit the
analyzer through the aperture. All ions of mass, $m \pm \Delta m$, will be deflected into the walls
of the analyzer. [Vickerman, 1989]

A.5 SIMS Depth Profiling

The primary application of SIMS that is of interest in this work is the use of the dynamic SIMS technique for the depth profiling of semiconductors. The application of SIMS to the depth profiling of semiconductors seems a natural extension of the SIMS process. The primary ion beam can be used to sputter the surface continually and the mass spectrometer and ion detector will measure the species of interest as a function of time. For a constant sputter rate, the time can be converted to depth, and with appropriate standards, the ion counts can be converted to concentrations. This is useful in the area of semiconductor research and development for the determination of dopant distributions, including diffusion or implant profiles. The energy of the ion beam controls the sputter rate and the depth resolution. Because it is a mass spectrometry technique SIMS can detect all elements of the Periodic Table, as well as the individual isotopes of the elements. The important experimental issues specific to depth profiling with SIMS will be discussed in this section.

<u>Depth Resolution</u>

The depth resolution is one of the more important parameters of depth profiling. There are several aspects of the SIMS measurement that will affect the depth resolution. The primary cause for a limitation of the depth resolution is the depth of origin of the secondary ions that are measured. The SIMS crater bottom is never completely flat due to the fact that secondary ion emission can occur from the top few monolayers of the material. This causes a minimum crater roughness of a few nanometers. However, any

additional surface roughness present in the sample surface prior to SIMS analysis will also limit the depth resolution. As an example, if the sample to be measured has a surface roughness of 1 micron, then as the primary ion beam sputters the surface and generates the crater, secondary ions will be emitted from depths of up to 1 micron deeper than the sputter depth of the crater, causing errors in the measurement of the concentration present at the crater depth. The impact of surface roughness on SIMS depth profiles is evident in the P diffusion profiles in Si presented in Figure 3.9 of Section 3.3.2.

Another aspect of the SIMS process that affects the depth of origin of secondary ions, and consequently the depth resolution, is the mixing of atoms induced by the primary ion beam impact and sputtering. The primary ion will penetrate the surface to a depth of several nanometers below the crater bottom, resulting in implantation damage and the collision cascades that generate the secondary ions. Randomization and disorder are generated in the region of primary ion beam impact leading to the formation of a mixing layer below the crater bottom, in which atoms of several adjacent layers are mixed together. As the depth profiling proceeds, secondary ions are generated by atoms that have been displaced by several nanometers, above or below, their original positions. This process of atom mixing below the crater bottom is depicted in the diagrams of Figure A.5. The depth to which the mixing layer extends is a limitation of the depth resolution. However since the mixing layer is formed from the disorder produced by the primary ion beam impact, reducing the incident ion beam energy will decrease the mixing layer depth and improve the depth resolution. Depending on the ion beam energy the depth resolution due to mixing can range from a few to tens of nanometers.
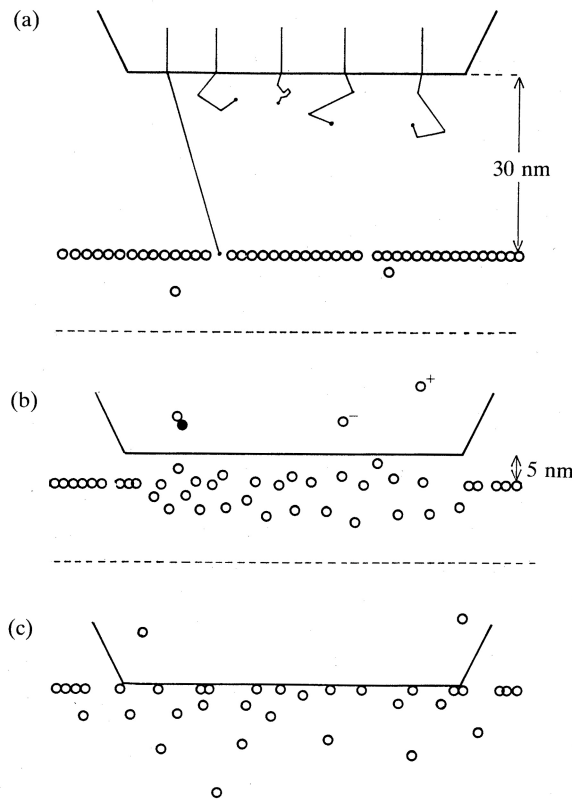
Figure A.5 Diagram representing the effect of the primary ion beam on depth resolution via the creation of a mixing layer. (a) the SIMS crater surface is greater than 30 nm from a layer of tracer atoms, there is little effect on the atoms. (b) the crater surface is within 5 nm of the tracer atom layer, primary ion beam impacts below the surface create a mixing layer, disordering the atoms in several layers. (c) the crater surface reaches the tracer atom layer many of the atoms have been scattered, reducing the measured tracer atom concentration at that depth. [Vickerman, 1989]

An additional error in SIMS analysis as a result of the formation of the mixing layer is the production of asymmetric concentration profiles due to so called "knock-on" effects. A certain fraction of the scattered atoms from the mixing layer are driven to a greater depth from the surface, i.e., are "knocked on" deeper into the sample. This causes a problem in the analysis of a concentration gradient from a region of high concentration to a region of low concentration, as a result of some of the atoms in the high

116

concentration region being driven into the low concentration region; where they are measured. This leads to an artificially high concentration measured in the low concentration region. The opposite effect, driving atoms from a low concentration region into a high concentration region would only cause errors in the case of a very small concentration gradient. The "knock-on" phenomenon is most often seen in steep symmetric profiles like those of ion implantation, where the leading edge (low to high concentration) of the Gaussian distribution is unaffected, but the trailing edge (high to low concentration) is artificially broadened by the SIMS analysis yielding an asymmetric peak in the SIMS depth profile. As with the case of the mixing layer, "knock-on" effects can be limited by reducing the incident ion beam energy.

Secondary Ion Collection

Scanning the ion beam across the sample surface generates the SIMS crater. For depth profiling, a reactive ion species like O_2^+ or Cs^+ is chosen to increase the secondary ion yield from the sample. The primary ion beam is scanned over a square area on the order of 200 μm per side. The large area is necessary to be able to collect sufficient ion counts from the sample. The ion beam is scanned over the area to produce uniform erosion of the sample surface. For accurate depth profiling, care must be taken to insure that the secondary ions collected and analyzed by the mass spectrometer are emitted from the bottom of the crater only. If the ion beam sputters secondary ions from the crater walls as it scans the crater area, ions will be collected both from the crater bottom and from the crater wall, at a depth closer to the surface, leading to ambiguity as to the ion origin and errors in depth resolution. To prevent these "edge-effect" errors from

117

occurring, a gate is used to allow only ions that are generated from the center of the crater to be collected. An electronic gate functions by disabling the ion counting when the scanning beam is outside the center of the crater area, thereby preventing crater wall ions from being counted. An optical gate reduces the field of view of the ion optics, which collects the secondary ions and directs them into the mass analyzer, to only the center of the crater.
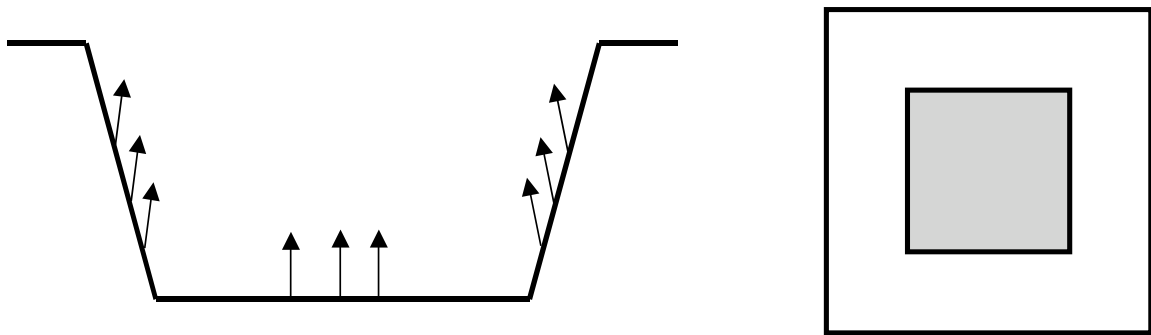
Figure A.6 An illustration of the cross-section of a SIMS crater showing the possible points of origin (arrows) of secondary ions due to the ion beam scanning of the crater area (left); an illustration of the top view of a SIMS crater showing the total area (white) and the gated collection area (gray) that enables analysis of only those ions produced by the crater bottom, and prevents edge effects (right).

Mass interferences can also significantly affect the ability to produce accurate depth profiles by generating ion counts from the mass analyzer that do not originate from the species of interest. Instead they arise from the presence of some other species or ion cluster with a similar mass. In this way, artificially high concentrations may be observed or the profile may indicate the presence of a species that does not in fact exist in the sample. One common source of mass interference that can affect a SIMS measurement is the residual vacuum. The vacuum in a SIMS analysis chamber is on the order of 10^{-6}

Torr, meaning that residual species in the vacuum may be adsorbed onto the surface and sputtered by the primary beam. Contaminants like C, H, N, and O, are likely to be present as a result of the residual vacuum. These contaminants can lead to mass interference due to cluster ions, for example in the analysis of Si, a $^{30}SiH^+$ ion would have the same mass as P, causing an artificially high P concentration to be measured. Similarly, carbon monoxide, CO, has the same mass as ^{28}Si, and could cause errors in the measurement of this matrix element. To prevent this type of mass interference, SIMS should be performed under a higher vacuum, thereby reducing the contaminants in the residual vacuum.

Multilayer Analysis

If the sample to be analyzed via SIMS contains multiple layers of varying matrix materials, such as semiconductor thin film heterostructures, then care must be taken to ensure that the variation in sputter rate and secondary ion yield between the materials is accounted for in the data analysis. The sputter rates of layers in a heterostructure will vary due to the different matrix compositions. For most SIMS measurements in a single matrix sample, the sputter rate is considered constant and the depth profile is determined from the total crater depth and the sputtering time. However, if the sputter rate is not constant, due to a change of matrix composition, then the calculation of the depth scale is no longer simple. The sputter rate of each layer in the heterostructure must be determined independently by sputtering a new crater through each layer, and the time and depth of that measurement is used to calculate the sputter rate for that layer. Since the ion yield of the species of interest will also vary with matrix composition, accurate

concentration measurements require a separate calibration standard for each species in

each matrix of the heterostructure.

Appendix B: Modeling and Simulation

B.1 Modeling of Simultaneous Self- and Dopant Diffusion

The computer modeling for the simultaneous dopant and self-diffusion results presented in Sections 3.1, 3.2, and 3.3 was developed and performed by Dr. Hartmut Bracht at the University of Münster, Germany. What follows in this section of the appendix is a summary of the modeling process used to fit the experimental data.

As discussed in Section 1.2.1, the diffusion of self- and dopant atoms in semiconductors is mediated by native point defects such as vacancies (V) and self-interstitials (I). The vacancy (Equation B.1), interstitialcy (Equation B.2), and kick-out (Equation B.3) mechanisms all possess a similar reaction scheme.

$$AV \leftrightarrow A_S + V \qquad\qquad (B.1)$$

$$AI \leftrightarrow A_S + I \qquad\qquad (B.2)$$

$$A_i \leftrightarrow A_S + I \qquad\qquad (B.3)$$

The equations representing these mechanisms were given in Equations 1.5 to 1.7 of Section 1.2.1, and are reproduced here for clarity. In the above equations, A represents the diffusing species, V represents a vacant lattice site, I represents an interstitial host atom, the subscript s denotes a substitutional lattice position, and the subscript i denotes an interstitial lattice position. Because of the similarity in reaction scheme, the mathematical formulation of the vacancy mechanism, Equation B.1, is also representative for reactions B.2 and B.3. The dissociative mechanism $A_i + V \leftrightarrow A_S$ describes another reaction scheme whose mathematical formulation is different from that of the vacancy

mechanism (see Section1.2.1). In this appendix, the modelling technique is illustrated using the vacancy mechanism. Equation B.4 is a more generalized form of the vacancy mechanism reaction represented by Equation B.1.

$$AV^j + (j - m - k)e^- \leftrightarrow A_s^m + V^k \tag{B.4}$$
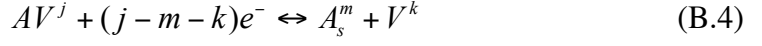
The superscripts denote the charge states j, m, and k of the point defects involved. The electrons, e^-, are included to insure charge neutrality of the equation. The following system of differential equations describes the diffusion of the dopant A via reaction B.4:

$$\frac{\partial \overline{C}_{A_s^m}}{\partial t} = \frac{\partial}{\partial x}\left(D_{A_s^m} \frac{\partial \overline{C}_{A_s^m}}{\partial x} + m \frac{\overline{C}_{A_s^m} D_{A_s^m}}{\overline{n}(x)} \frac{\partial \overline{n}(x)}{\partial x} \right) + k_- C_{V^k}^{eq}(\overline{C}_{AV^j}\overline{n}^{-(j-m-k)} - \overline{C}_{A_s^m}\overline{C}_{V^k}) \tag{B.5}$$

$$\frac{C_{AV^j}^{eq}}{C_{A_s^m}^{eq}}\frac{\partial \overline{C}_{AV^j}}{\partial t} = \frac{\partial}{\partial x}\left(D_{AV^j}^* \frac{\partial \overline{C}_{AV^j}}{\partial x} + j \frac{\overline{C}_{AV^j} D_{AV^j}}{\overline{n}(x)} \frac{\partial \overline{n}(x)}{\partial x} \right) - k_- C_{V^k}^{eq}(\overline{C}_{AV^j}\overline{n}^{-(j-m-k)} - \overline{C}_{A_s^m}\overline{C}_{V^k})$$

$$\tag{B.6}$$

$$\frac{C_{V^k}^{eq}}{C_{A_s^m}^{eq}}\frac{\partial \overline{C}_{V^k}}{\partial t} = \frac{\partial}{\partial x}\left(D_{V^k}^* \frac{\partial \overline{C}_{V^k}}{\partial x} + k \frac{\overline{C}_{V^k} D_{V^k}}{\overline{n}(x)} \frac{\partial \overline{n}(x)}{\partial x} \right) + k_- C_{V^k}^{eq}(\overline{C}_{AV^j}\overline{n}^{-(j-m-k)} - \overline{C}_{A_s^m}\overline{C}_{V^k}) \tag{B.7}$$

In this equation system, k_- is the backward rate constant of reaction B.4 which is interrelated with the forward rate constant k_+ via the equation:

$$\frac{k_+}{k_-} = \frac{C_{A_s^m}^{eq} C_{V^k}^{eq}}{C_{AV^j}^{eq}(n^{eq})^{(j-m-k)}} \tag{B.8}$$

which results from the law of mass action. The concentration of the point defect under thermal equilibrium conditions is represented by C^{eq} in Equation B.8, where n^{eq} is the corresponding electron concentration. In the equation system of B.5 to B.7, the normalized concentration of the point defect is given by $\overline{C} = C/C^{eq}$ and $\overline{n} = n/n^{eq}$ is the normalized free electron concentration. The reduced diffusivity is denoted by

$D^* = C^{eq} D / C^{eq}_{A^m_s}$. The simulations are relatively insensitive to the input values for the

concentration ratios of the point defects, so long as the point defect concentration is much

less than the dopant concentration. This is clearly the case for the extrinsic doping

presented in this work. The initial diffusivity values that are input into the equations are

chosen to be consistent with previous experiments and values found in literature. This

differential equation system with normalized concentrations and reduced diffusivities is

advantageous for solving the diffusion equations numerically. This system is the full set

of equations needed to calculate the concentration profiles of all defects involved in

reaction B.4 for specific initial and boundary conditions.

For modelling the simultaneous diffusion of dopant- and self-atoms, the self-

diffusion equation must be incorporated into the system of differential equations. The

self-diffusion of the host atom Z is described by:

$$\frac{\partial C_Z}{\partial t} = \frac{\partial}{\partial x} D_Z \frac{\partial C_Z}{\partial x} \tag{B.9}$$

where the self-diffusion coefficient is given by D_Z. Taking into account the contributions

of the native defects and native defect pairs, V, I, AV, and AI to self-diffusion, the self-

diffusion coefficient can be written as:

$$D_Z = \left(\sum_k f_V C_{V^k} D_{V^k} + \sum_u f_I C_{I^u} D_{I^u} + \sum_j f_{AV} C_{AV^j} D_{AV^j} + \sum_v f_{AI} C_{AI^v} D_{AI^v} \right) \frac{1}{C_o} \tag{B.10}$$

The sum reflects the contributions of the various charged defects with diffusion

correlation factors, f_V, f_I, f_{AV}, f_{AI}, which are assumed to be independent of the charge

state. The role of correlation factors in the diffusivity was described in Section 1.2.1.

The self-atom density, C_o, is 5×10^{22} cm^{-3} for silicon.

123

Introducing the normalized concentrations and reduced diffusivities give the self-diffusion coefficient of the form:

$$D_Z = \left(\sum_k f_V D^*_{V^k} \overline{C}_{V^k} + \sum_u f_I D^*_{I^u} \overline{C}_{I^u} + \sum_j f_{AV} D^*_{AV^j} \overline{C}_{AV^j} + \sum_v f_{AI} D^*_{AI^v} \overline{C}_{AI^v} \right) \frac{C^{eq}_{A^m_s}}{C_o} \qquad (B.11)$$

This equation for the self-diffusion coefficient is advantageous for solving numerically the differential equations for the simultaneous diffusion of self- and dopant atoms because Equation B.11 contains the same model parameters D^* and concentration variables $\overline{C}$ that also enter Equations B.5 to B.7.

In order to identify the mechanisms that control dopant- and self-atom diffusion in semiconductors, extensive computer simulations have to be performed on the basis of the possible diffusion mechanisms. This is achieved with the use of the partial differential equation solver ZOMBIE [Jüngling, 1985]. The model, consisting of the whole set of differential equations, along with the appropriate boundary and initial conditions, is input into the differential equation solver. The SIMS concentration profile of the as-grown structure is used as the initial concentration profile to which the system of differential equations is applied to generate a simulated diffusion profile in the multilayered structure. Once the initial simulations give a reasonably accurate match to the experimental SIMS data, the mathematical equation solver Profile [Ouwerling, 1989] is used to obtain a best fit. A subroutine for the Profile program runs the ZOMBIE simulation for a set of initial parameters including the diffusion coefficients for each diffusing species. The simulation result is then compared to the experimental SIMS result by the Profile program using the Modified Damped Least Squares non-linear

124

parameter optimization technique. This is an improved variation on the Levenberg-Marquart (lev-mar) method. The diffusion coefficients determined by the best-fit to the ZOMBIE simulation are then considered the values that match the experimental data.

Compelling evidence in support of the assumed diffusion mechanism is obtained when the experimental profiles are accurately described with a specific mechanism and the model yields parameters that are physically reasonable and consistent with other experimental results. It should be emphasized that the experimental dopant profiles are mainly sensitive to the reduced diffusion coefficients D^* that also affect the self-diffusion. Accordingly the consistent modelling of the simultaneous diffusion of self- and dopant atoms in isotope multilayer structures provides direct information about the mechanisms of dopant diffusion and the individual contributions of native defect charge states to self-diffusion.

Modelling of Simultaneous Boron and Silicon Self-Diffusion

The model that appropriately described the simultaneous boron and silicon self-diffusion consisted of the following reactions:

$$B_i^o \Leftrightarrow B_s^- + I^o + h \tag{B.12}$$

$$B_i^o \Leftrightarrow B_s^- + I^+ \tag{B.13}$$

$$B_i^o + V^o \Leftrightarrow B_s^- + h \tag{B.14}$$

$$B_i^o + V^+ \Leftrightarrow B_s^- + 2h \tag{B.15}$$

Where B_i^o is the neutral boron interstitial, B_s^- the negatively charged boron on a substitutional site, I and V represent the corresponding interstitial or vacancy charge state and h represents holes needed for charge neutrality of the reactions.

125

The full set of differential equations used for the modelling and simulation of the boron and silicon simultaneous self-diffusion described in Section 3.1 are presented in Figure B.1. The highlighted reduced diffusion coefficients, D^*, are the values generated by the solution to the set of equations. The first equation, I, represents the change in concentration of the substitutional boron, and the subscripts 1, 2, 3, and 4 denote the contributions from Equations B.12 to B.15, respectively, to the formation of substitutional boron. Equations III, IV, V, and VI of Figure B.1 describe the diffusion of the native defects involved in the reactions B.12 to B.15. Equations II and VII describe the diffusion of the boron interstitial and the silicon self-diffusion, respectively. The equations describing the reduced diffusion coefficients used in the model are also included in Figure B.1.

Modeling of Simultaneous Arsenic and Silicon Self-Diffusion

The simultaneous arsenic and silicon self-diffusion was modeled using the following set of reactions:

$$\left(AsI \right)^- \Leftrightarrow As_s^+ + I^- + e \tag{B.16}$$

$$\left(AsI \right)^o \Leftrightarrow As_s^+ + I^- \tag{B.17}$$

$$\left(AsV \right)^o \Leftrightarrow As_s^+ + V^o + e \tag{B.18}$$

$$\left(AsV \right)^o + I^- \Leftrightarrow As_s^+ + 2e \tag{B.19}$$

Where AsV and AsI are the arsenic-vacancy and arsenic-interstitial pairs, respectively. The vacancy and interstitial of the corresponding charge state are represented by V and I, while e represents electrons used in the reaction for charge neutrality.

The system of differential equations that was generated from the model reactions B.16 to B.19 is given in Figure B.2. These differential equations were used to simulate the diffusion profiles of arsenic and silicon described in Section 3.2.3. The reduced diffusion coefficients of the species in the model reactions, D^*, are highlighted in the differential equations and given in detail at the bottom of the figure. The first equation, I, represents the change in concentration of the substitutional arsenic, and the subscripts 1, 2, 3, and 4 denote the contributions from Equations B.16 to B.19, respectively, to the formation of substitutional arsenic. Equations II, III, IV, V, and VI of Figure B.2 describe the diffusion of the native defects involved in the reactions B.16 to B.19. Equation VII describes the silicon self-diffusion.

Modeling of Simultaneous Phosphorus and Silicon Self-Diffusion

The simultaneous phosphorus and silicon self-diffusion was modeled using the following set of reactions:

$$PI^o(P_i^o) \Leftrightarrow P_s^+ + I^o + e \tag{B.20}$$

$$PI^o(P_i^o) \Leftrightarrow P_s^+ + I^- \tag{B.21}$$

$$PI^o(P_i^o) + V^o \Leftrightarrow P_s^+ + e \tag{B.22}$$

$$PI^+(P_i^+) \Leftrightarrow P_s^+ + I^o \tag{B.23}$$

$$PI^+(P_i^+) + V^o \Leftrightarrow P_s^+ \tag{B.24}$$

Where PI and P_i represent the phosphorus-interstitial pair and phosphorus atom located on an interstitial site, respectively, for the given charge states. The vacancy and interstitial of the corresponding charge state are represented by V and I, while e represents electrons used in the reaction for charge neutrality. The interstitial phosphorus

representation is given in each equation along with PI because the model has only been

generated for PI and therefore, strictly from a modeling standpoint, P_i cannot be ruled out

as a possible replacement for PI in the above equations without further modeling. The

system of differential equations that was generated from the model reactions B.20 to

B.24, assuming a PI defect, is given in Figure B.3. These differential equations were

used to simulate the diffusion profiles of arsenic and silicon described in Section 3.3.

The first equation, I, represents the change in concentration of the substitutional

phosphorus, and the subscripts 1, 2, 3, 4, and 5 denote the contributions from Equations

B.20 to B.24, respectively, to the formation of substitutional arsenic. Equations II, III,

IV, V, and VI of Figure B.3 describe the diffusion of the native defects involved in the

reactions B.20 to B.24. Equation VII describes the silicon self-diffusion. The reduced

diffusion coefficients of the species in the model reactions, D^*, are highlighted in the

differential equations and given in detail at the bottom of the figure.

I. $\dfrac{\partial \widetilde{C}_{B_s}}{\partial t} = \left(\dfrac{\partial \widetilde{C}_{B_s}}{\partial t}\right)_1 + \left(\dfrac{\partial \widetilde{C}_{B_s}}{\partial t}\right)_2 + \left(\dfrac{\partial \widetilde{C}_{B_s}}{\partial t}\right)_3 + \left(\dfrac{\partial \widetilde{C}_{B_s}}{\partial t}\right)_4$

II. $\dfrac{C^{eq}_{B_i}}{C^{eq}_{B_s}}\dfrac{\partial \widetilde{C}_{B_i}}{\partial t} - D^*_{B_i}\dfrac{\partial^2 \widetilde{C}_{B_i}}{\partial x^2} = -\left(\dfrac{\partial \widetilde{C}_{B_s}}{\partial t}\right)$

III. $\dfrac{C^{eq}_{I^0}}{C^{eq}_{B_s}}\dfrac{\partial \widetilde{C}_{I^0}}{\partial t} - D^*_{I^0}\dfrac{\partial^2 \widetilde{C}_{I^0}}{\partial x^2} = \left(\dfrac{\partial \widetilde{C}_{B_s}}{\partial t}\right)_1$

IV. $\dfrac{C^{eq}_{I^+}}{C^{eq}_{B_s}}\dfrac{\partial \widetilde{C}_{I^+}}{\partial t} - \dfrac{\partial}{\partial x}\left[D^*_{I^+}\dfrac{\partial \widetilde{C}_{I^+}}{\partial x} - D^*_{I^+}\dfrac{\widetilde{C}_{I^+}}{\sqrt{\widetilde{C}^2_{B_s} + 4\widetilde{n}^2_i}}\dfrac{\partial \widetilde{C}_{B_s}}{\partial x}\right] = \left(\dfrac{\partial \widetilde{C}_{B_s}}{\partial t}\right)_2$

V. $\dfrac{C^{eq}_{V^0}}{C^{eq}_{B_s}}\dfrac{\partial \widetilde{C}_{V^0}}{\partial t} - D^*_{V^0}\dfrac{\partial^2 \widetilde{C}_{V^0}}{\partial x^2} = -\left(\dfrac{\partial \widetilde{C}_{B_s}}{\partial t}\right)_3$

VI. $\dfrac{C^{eq}_{V^+}}{C^{eq}_{B_s}}\dfrac{\partial \widetilde{C}_{V^+}}{\partial t} - \dfrac{\partial}{\partial x}\left[D^*_{V^+}\dfrac{\partial \widetilde{C}_{V^+}}{\partial x} - D^*_{V^+}\dfrac{\widetilde{C}_{V^+}}{\sqrt{\widetilde{C}^2_{B_s} + 4\widetilde{n}^2_i}}\dfrac{\partial \widetilde{C}_{B_s}}{\partial x}\right] = \left(\dfrac{\partial \widetilde{C}_{B_s}}{\partial t}\right)_4$

VII. $\dfrac{\partial C_{Si}}{\partial t} - \dfrac{\partial}{\partial x}D_{Si}\dfrac{\partial C_{Si}}{\partial x} = 0$

$D^*_{B_i} = \dfrac{C^{eq}_{B_i}D_{B_i}}{C^{eq}_{B_s}} \quad \rightarrow \quad D_B = D^*_{B_i}\cdot\dfrac{n_i}{C^{eq}_{B_s}}$

$D^*_{I^0} = \dfrac{C^{eq}_{I^0}D_{I^0}}{C^{eq}_{B_s}}$

$D^*_{I^+} = \dfrac{C^{eq}_{I^+}D_{I^+}}{C^{eq}_{B_s}} \approx \dfrac{C^{eq}_{I^0}D_{I^0}\,g\,\exp\left(\dfrac{E_{I^{0/+}} - E_f}{kT}\right)}{C^{eq}_{B_s}}$

$D_{Si} = f_{I^0}C_{I^0}D_{I^0} + f_{I^+}C_{I^+}D_{I^+} + f_{V^0}C_{V^0}D_{V^0} + f_{V^+}C_{V^+}D_{V^+}$

Figure B.1 The full set of differential equations used to model the simultaneous B and Si self-diffusion. Also included are the equations for the reduced diffusion coefficients, D^* and the Si self-diffusion coefficient. (Courtesy of H. Bracht)

I. $$\frac{\partial \tilde{C}_{As_s}}{\partial t} = \left(\frac{\partial \tilde{C}_{As_s}}{\partial t}\right)_1 + \left(\frac{\partial \tilde{C}_{As_s}}{\partial t}\right)_2 + \left(\frac{\partial \tilde{C}_{As_s}}{\partial t}\right)_3 + \left(\frac{\partial \tilde{C}_{As_s}}{\partial t}\right)_4$$

II. $$\frac{C^{eq}_{(AsI)^-}}{C^{eq}_{As_s}}\frac{\partial \tilde{C}_{(AsI)^-}}{\partial t} - \frac{\partial}{\partial x}\left[D^*_{(AsI)^-}\frac{\partial \tilde{C}_{(AsI)^-}}{\partial x} - D^*_{(AsI)^-}\frac{\tilde{C}_{(AsI)^-}}{\sqrt{\tilde{C}^2_{As_s} + 4\tilde{n}^2_i}}\frac{\partial \tilde{C}_{As_s}}{\partial x}\right] = -\left(\frac{\partial \tilde{C}_{As_s}}{\partial t}\right)_1$$

III. $$\frac{C^{eq}_{(AsI)^o}}{C^{eq}_{As_s}}\frac{\partial \tilde{C}_{(AsI)^o}}{\partial t} - D^*_{(AsI)^o}\frac{\partial^2 \tilde{C}_{(AsI)^o}}{\partial x^2} = -\left(\frac{\partial \tilde{C}_{As_s}}{\partial t}\right)_2$$

IV. $$\frac{C^{eq}_{(AsV)^o}}{C^{eq}_{As_s}}\frac{\partial \tilde{C}_{(AsV)^o}}{\partial t} - D^*_{(AsV)^o}\frac{\partial^2 \tilde{C}_{(AsV)^o}}{\partial x^2} = -\left(\frac{\partial \tilde{C}_{As_s}}{\partial t}\right)_3 - \left(\frac{\partial \tilde{C}_{As_s}}{\partial t}\right)_4$$

V. $$\frac{C^{eq}_{I^-}}{C^{eq}_{As_s}}\frac{\partial \tilde{C}_{I^-}}{\partial t} - \frac{\partial}{\partial x}\left[D^*_{I^-}\frac{\partial \tilde{C}_{I^-}}{\partial x} - D^*_{I^-}\frac{\tilde{C}_{I^-}}{\sqrt{\tilde{C}^2_{As_s} + 4\tilde{n}^2_i}}\frac{\partial \tilde{C}_{As_s}}{\partial x}\right] = \left(\frac{\partial \tilde{C}_{As_s}}{\partial t}\right)_1 + \left(\frac{\partial \tilde{C}_{As_s}}{\partial t}\right)_2 - \left(\frac{\partial \tilde{C}_{As_s}}{\partial t}\right)_4$$

VI. $$\frac{C^{eq}_{V^o}}{C^{eq}_{As_s}}\frac{\partial \tilde{C}_{V^o}}{\partial t} - D^*_{V^o}\frac{\partial^2 \tilde{C}_{V^o}}{\partial x^2} = \left(\frac{\partial \tilde{C}_{As_s}}{\partial t}\right)_3$$

VII. $$\frac{\partial C_{Si}}{\partial t} - \frac{\partial}{\partial x}D_{Si}\frac{\partial C_{Si}}{\partial x} = 0$$

$$D^*_{(AsI)^-} = \frac{C^{eq}_{(AsI)^-}D_{(AsI)^-}}{C^{eq}_{As_s}} \quad ; \quad D^*_{(AsI)^0} = \frac{C^{eq}_{(AsI)^0}D_{(AsI)^0}}{C^{eq}_{As_s}} \quad ; \quad D^*_{(AsV)^0} = \frac{C^{eq}_{(AsV)^0}D_{(AsV)^0}}{C^{eq}_{As_s}}$$

$$D^*_{I^-} = \frac{C^{eq}_{I^-}D_{I^-}}{C^{eq}_{As_s}} \quad ; \quad D^*_{V^0} = \frac{C^{eq}_{V^0}D_{V^0}}{C^{eq}_{As_s}} \quad ; \quad D_{Si} = f_{I^0}C_{I^0}D_{I^0} + f_{V^0}C_{V^0}D_{V^0} + f_{I^-}C_{I^-}D_{I^-} + f_{(AI)^0}C^{eq}_{(AI)^0}D_{(AI)^0} + \dots$$

Figure B.2 The full set of differential equations used to model the simultaneous As and Si self-diffusion. The equations for the reduced diffusion coefficients of each of the diffusing species, D^*, and the Si self-diffusion coefficient are presented at the bottom of the figure. (Courtesy of H. Bracht)

$$\text{I.} \quad \frac{\partial \tilde{C}_{P_s}}{\partial t} = \left(\frac{\partial \tilde{C}_{P_s}}{\partial t}\right)_1 + \left(\frac{\partial \tilde{C}_{P_s}}{\partial t}\right)_2 + \left(\frac{\partial \tilde{C}_{P_s}}{\partial t}\right)_3 + \left(\frac{\partial \tilde{C}_{P_s}}{\partial t}\right)_4 + \left(\frac{\partial \tilde{C}_{P_s}}{\partial t}\right)_5$$

$$\text{II.} \quad \frac{C_{(PI)^+}^{eq}}{C_{P_s}^{eq}} \frac{\partial \tilde{C}_{(PI)^+}}{\partial t} - \frac{\partial}{\partial x}\left[D_{(PI)^+}^* \frac{\partial \tilde{C}_{(PI)^+}}{\partial x} + D_{(PI)^+}^* \frac{\tilde{C}_{(PI)^+}}{\sqrt{\tilde{C}_{P_s}^2 + 4\tilde{n}_i^2}} \frac{\partial \tilde{C}_{P_s}}{\partial x} \right] = -\left(\frac{\partial \tilde{C}_{P_s}}{\partial t}\right)_4 - \left(\frac{\partial \tilde{C}_{P_s}}{\partial t}\right)_5$$

$$\text{III.} \quad \frac{C_{(PI)^0}^{eq}}{C_{P_s}^{eq}} \frac{\partial \tilde{C}_{(PI)^0}}{\partial t} - D_{(PI)^0}^* \frac{\partial^2 \tilde{C}_{(PI)^0}}{\partial x^2} = -\left(\frac{\partial \tilde{C}_{P_s}}{\partial t}\right)_1 - \left(\frac{\partial \tilde{C}_{P_s}}{\partial t}\right)_2 - \left(\frac{\partial \tilde{C}_{P_s}}{\partial t}\right)_3$$

$$\text{IV.} \quad \frac{C_{I^0}^{eq}}{C_{P_s}^{eq}} \frac{\partial \tilde{C}_{I^0}}{\partial t} - D_{I^0}^* \frac{\partial^2 \tilde{C}_{I^0}}{\partial x^2} = \left(\frac{\partial \tilde{C}_{P_s}}{\partial t}\right)_1 + \left(\frac{\partial \tilde{C}_{P_s}}{\partial t}\right)_4$$

$$\text{V.} \quad \frac{C_{I^-}^{eq}}{C_{P_s}^{eq}} \frac{\partial \tilde{C}_{I^-}}{\partial t} - \frac{\partial}{\partial x}\left[D_{I^-}^* \frac{\partial \tilde{C}_{I^-}}{\partial x} - D_{I^-}^* \frac{\tilde{C}_{I^-}}{\sqrt{\tilde{C}_{P_s}^2 + 4\tilde{n}_i^2}} \frac{\partial \tilde{C}_{P_s}}{\partial x} \right] = \left(\frac{\partial \tilde{C}_{As_s}}{\partial t}\right)_2$$

$$\text{VI.} \quad \frac{C_{V^0}^{eq}}{C_{P_s}^{eq}} \frac{\partial \tilde{C}_{V^0}}{\partial t} - D_{V^0}^* \frac{\partial^2 \tilde{C}_{V^0}}{\partial x^2} = -\left(\frac{\partial \tilde{C}_{P_s}}{\partial t}\right)_3 - \left(\frac{\partial \tilde{C}_{P_s}}{\partial t}\right)_5$$

$$\text{VII.} \quad \frac{\partial C_{Si}}{\partial t} - \frac{\partial}{\partial x} D_{Si} \frac{\partial C_{Si}}{\partial x} = 0$$

$$D_{(PI)^+}^* = \frac{C_{(PI)^+}^{eq} D_{(PI)^+}}{C_{P_s}^{eq}} \quad ; \quad D_{(PI)^0}^* = \frac{C_{(PI)^0}^{eq} D_{(PI)^0}}{C_{P_s}^{eq}}$$

$$D_{I^-}^* = \frac{C_{I^-}^{eq} D_{I^-}}{C_{P_s}^{eq}} \quad ; \quad D_{I^0}^* = \frac{C_{I^0}^{eq} D_{I^0}}{C_{P_s}^{eq}} \quad ; \quad D_{V^0}^* = \frac{C_{V^0}^{eq} D_{V^0}}{C_{P_s}^{eq}}$$

$$D_{Si} = f_{V^0} C_{V^0} D_{V^0} + f_{I^0} C_{I^0} D_{I^0} + f_{I^-} C_{I^-} D_{I^-} + f_{(PI)^0} C_{(PI)^0} D_{(PI)^0} + f_{(PI)^+} C_{(PI)^+} D_{(PI)^+}$$

Figure B.3 The full set of differential equations used to model the simultaneous P and Si self-diffusion. The equations for the reduced diffusion coefficients of each of the diffusing species, D^*, and the Si self-diffusion coefficient are presented at the bottom of the figure. (Courtesy of H. Bracht)

B.2 Modeling of the Diffusion of Silicon in Germanium

The modeling of the diffusion of silicon in germanium was performed using a Fick's law type differential equation like that of Equation B.20:

$$\frac{\partial C_{Si}}{\partial t} = -\frac{\partial}{\partial x} D_{Si} \frac{\partial C_{Si}}{\partial x} \qquad \text{(B.20)}$$

Unlike the extensive systems of equations used in the previous section for simultaneous self- and dopant diffusion, only a single differential equation is needed to appropriately describe the diffusion of Si in Ge. As in the previous approach, the partial differential equation solver ZOMBIE [Jüngling, 1985] was utilized to numerically solve the differential equation for the appropriate boundary and initial conditions. The concentration profile of the as-grown structure determined via SIMS was taken as the initial concentration profile of the simulation. The mathematical equation solver Profile [Ouwerling, 1989] was again used to obtain a best fit to the experimental SIMS results by employing the Modified Damped Least Squares non-linear parameter optimization technique (Levenberg-Marquart method) on the ZOMBIE simulations. The diffusion coefficient for Si in Ge was the fitting parameter in the Profile best-fit routine. The value of the diffusion coefficient was determined by the best-fit of the experimental results to the ZOMBIE simulation. The simulation was performed assuming a concentration independent Si diffusion coefficient with reflecting boundary conditions at the upper boundary and a sink at the lower boundary (sample surface).

References

Antoniadis, D. A., Gonzalez, A. G., and Dutton, R. W., *J. Electrochem. Soc.* **125** 813 (1978).

Barr, L. W., The origin of quantitative diffusion measurements in solids: A centenary view, in *Defects and Diffusion Forum* **143-147**, 3, Trans. Tech, Zurich Switzerland, (1997).

Becquerel, H., *Comptes Rendus* **122**, 501 (1896).

Benninghoven, A., *Z. Physik* **230** 403 (1970).

Benninghoven, A, Rüdenauer, F. G., Werner, H. W., *Secondary Ion Mass Spectrometry: basic concepts, instrumental aspects, applications, and trends*, J. Wiley, New York (1987).

Blaise, G., and Nourtier, A., *Surf. Sci.* **90** 495 (1979).

Bracht, H., *Defect and Diffusion Forum*, **143-147** 979 (1997)a.

Bracht, H., and Rodriguez Schachtrup, A., *Mat. Res. Soc. Symp. Proc.* **469** 25 (1997)b.

Bracht, H., Haller, E. E., and Clark-Phelps, R., *Phys. Rev. Lett.* **81** 393 (1998).

Bracht, H., *Physica B* **273-274** 981 (1999)a.

Bracht, H., Norseng, M., Haller, E. E., Eberl, K., Cardona, M., *Solid State Communications* **112** 30 (1999)b.

Bracht, H., Nicols, S. P., Walukiewicz, W., Silviera, J. P., Briones, F., and Haller, E. E., *Nature* **408** 69 (2000).

Bracht, H., Habilitationschrift, Universität Münster, (2001)a.

Bracht, H., Nicols, S. P., Haller, E. E., Silviera, J. P., and Briones, F., *J. Appl. Phys.* **89** 5393 (2001)b.

Brundle, C. R., Evans Jr., C. A., and Wilson, S., eds., *Encyclopedia of Materials Characterization: Surfaces, Interfaces and Thin Films*, (Butterworth-Heinemann; and Manning publishers, Greenwich) p. 40 (1992).

Compaan, K., and Haven, Y., *Trans. Faraday Soc.* **52** 786 (1956).

Compaan, K., and Haven, Y., *Trans. Faraday Soc.* **54** 1498 (1958).

Corbett, J. W., McDonald, R. S., and Watkins, G. D., *J. Phys. Chem. Solids* **25** 873 (1964).

Cowern, N. E. B., Theunuissen, M. J. J., Roozeboom, F., and van Berkum, J. G. M., *App. Phys. Lett.* **75** 181 (1999).

Eaglesham, D. J., Stolk, P. A., Gossmann, H. -J., Poate, J. M., *Appl. Phys. Lett.* **65**(18) 2305 (1994).

Einstein, A., *Ann. Phys.* **17**, 549 (1905). (English translation, *Investigations on the theory of Brownian Movement by Albert Einstein*, edited by R. Fürth, Methuen, London, 1926).

Fahey, P., Barbuscia, G., Moslehi, M., and Dutton, R. W., *Appl. Phys. Lett.* **46** 784 (1985)a.

Fahey, P., Ph.D. thesis, Stanford University (1985)b.

Fahey, P. M., Griffin, P. B., and Plummer, J. D., *Reviews of Modern Physics* **61** 289 (1989).

Fair, R. B., and Tsai, J. C. C., *J. Electrochem. Soc.* **124** 1107 (1977).

Fairfield, J. M., and Masters, B. J., *J. Appl. Phys.* **38** 3148 (1967).

Fick, A., Ueber diffusion, *Poggendorffs Ann. Phys. Chem.*, 59 (1855)a.

Fick, A., On liquid diffusion, *Philos. Mag. J. Sci.* **10**, 31 (1855)b.

Fourier, J. B. J., *Théorie Analytique de la Chaleur*, F. Didot, Paris, (1822).

Frank, W., Gösele, U., Mehrer, H., and Seeger, A., *Diffusion in Silicon and Germanium*, in Diffusion in Crystalline Solids, Eds. G. E. Murch and A. S. Nowick, Academic Press, New York, p. 63 (1984).

Frenkel, Y., *Zeitschrift für Physik* **35**, 652 (1926).

Fuchs, H. D., Walukiewicz, W., Haller, E. E., Dondl, W., Schorer, R., Abstreiter, G., Rudnev, A. I., Tikhomirov, A. V., Ozhogin, V. I., *Phys. Rev. B* **51** 16817 (1995).

Ghoshtagore, R. N., *Phys. Rev. Lett.* **16** 890 (1966).

Groh, J., and Hevesy, G., *Ann. Phys.* **63**, 85 (1920).

Groh, J., and Hevesy, G., *Ann. Phys.* **65**, 216 (1921).

Herzog, R. F. K., and Vieböck, F. P., *Phys. Rev.* **76** 855L (1949).

Hevesy, G., and Obrutsheva, A., *Nature* **115**, 674 (1925).

Hirvonen, J., and Anttila, A., *Appl. Phys. Lett.* **35** 703 (1979).

The International Technology Roadmap for Semiconductors (ITRS), Semiconductor Industry Association, San Jose, CA (2001).

Jüngling, W., Pichler, P., Selberherr, S., Guerro, E., and Pötzl, H. W., *IEEE Trans. Electron.Devices ED* **32** 156 (1985).

Kirkendall, E. O., *Trans. AIME* **147**, 104 (1942).

LeClaire, A. D., *Phil. Mag.* **14** 1271 (1966).

Littmark, U. and Hofer, W., *J. Mater. Sci.* **13** 2577 (1978).

Makris, J. S., and Masters, B. J., *J. Electrochem. Soc.* **120** 1252 (1973).

Masters, B. J., and Fairfield, J. M., *Appl. Phys. Lett.* **8** 280 (1966).

Masters, B. J., and Fairfield, J. M., *J. Appl. Phys.* **40** 2390 (1969).

Maul, J. and Wittmaack, K., *Surf. Sci.* **53** 596 (1975).

Mayer, H. J., Mehrer, H., and Maier, K, *Proceedings of the IOF International Conference on Radiation Effects in Semiconductors, Dubrovnik, 1976* (Institute of Physics, London) p.186 (1977).

McVay, G. L., and DuCharme, A. R., *J. Appl. Phys.* **44** 1409 (1973).

McVay, G. L., and DuCharme, A. R., *Phys. Rev. B* **9** 627 (1974).

McVay, G. L., and DuCharme, A. R., *Inst. Phys. Conf. Ser.* **23** 91 (1975).

Mizuo, S., and Higuchi, H., *Jpn. J. Appl. Phys.* **20** 739 (1981).

Mizuo, S., Kusaka, T., Shintani, A., Nanba, M., and Higuchi, H., *J. Appl. Phys.* **54** 3860 (1983).

Morin, F. J., and Maita, J. P., *Phys. Rev.* **96** 28 (1954).

Mullen, J. G., *Phys. Rev.* **121** 1649 (1961).

Nakabayashi, Y., Osman, H. I., Segawa, T., Saito, K., Matsumoto, S., Murota, J., Wada, K., Abe, T., *Jpn. J. Appl. Phys.* **40** L181 (2001).

Narasimhan, T. N., Fourier's heat conduction equation: History, influence, and connections, *Reviews of Geophysics* **37**, 151, (1999).

Nørskov, J. K., and Lundqvist, B. I., *Phys. Rev. B* **19** 5661 (1979).

Ohm, G. S,, *Die galvanische Kette, mathematisch Bearbeitet*, T. H. Riemann, Berlin, (1827). (English translation, W. Francis, *The Galvanic Circuit Investigated Mathematically*, Van Nostrand, New York, 1891).

Ouwerling, G. L. J., doctoral thesis, Delft University of Technology, (1989).

Packan, P. A., *MRS Bulletin*, **25** (6) 18 (2000).

Peart, R. F., *Phys. Stat. Sol.* **15** K119 (1966).

Räisänen, J., Hirvonen, J., and Antilla, A., *Solid-State Electronics* **24** 333 (1981).

Roberts-Austen, W. C., On the diffusion of metals, *Philos. Trans. R. Soc. London* **187**, 383, (1896).

Roentgen, W. C., *Sitzgber. Physik. –Med. Ges. Wurzburg* **137** (1895).

Roosendaal, H. E., in *Sputtering by Particle Bombardment I*, Springer Series Topics in Applied Physics, Springer Verlag, Berlin **47** 219 (1981).

Sadigh, B., Lenosky, T. J., Theiss, S. K., Caturla, M. J., Diaz de la Rubia, T., and Foad, M.A., *Phys. Rev. Lett.* **83** 4341 (1999).

Seeger, A., and Chik, K. P., *Phys. Stat. Sol.* **29** 455 (1968).

Seith, W., and Keil, A., *Z. Phys. Chemie B* **22** 350 (1933).

Sharp I. D., Bracht, H. A., Silvestri, H. H., Nicols, S. P., Beeman, J. W., Hansen, J., Nylandsted Larsen, A., Haller, E. E., *Mat. Res. Soc. Symp. Proc.* **719** F13.11.1 (2002).

Shockley, W., and Last, J. T., *Phys. Rev.* **107** 392 (1957).

Shockley, W., and Moll, J. L., *Phys. Rev.* **119** 1480 (1960).

Smigelskas, A. D., and Kirkendall, E. O., *Trans. AIME* **171**, 130 (1947).

Södervall, U., and Friesel, M., *Defect and Diffusion Forum* **143-147** 1053 (1997).

Stolwijk, N.A., and Bracht, H., "Diffusion in Silicon, Germanium and their Alloys" in Landolt Börnstein New Series Vol. III/33 Subvolume A (Springer) p 1-257 (1998).

Strohm, A., Voss, T., Frank, W., Räisänen, J, and Dietrich, M., *Physica B* **308-310** 542 (2001).

Strohm, A., Voss, T., Frank, W., Laitinen, P., Räisänen, J, *Z. Metallkd.* **93** 737 (2002).

Tan, T. Y., and Gösele, U., *Appl. Phys. A* **37** 1 (1985).

Thomson, J. J., *Phil. Mag.* **20** 252 (1910).

Thurmond, C. D., Guldner, W. G., and Beach, A. L., *J. Electrochem. Soc.* **103** 603 (1956).

Uematsu, M., *J. Appl. Phys.* **82** 2228 (1997).

Uppal, S., Ph.D. thesis, University of Southampton (2003).

Ural, A., Griffin, P. B., and Plummer, J. D., *Appl. Phys. Lett.* **79** 4328 (2001).

Vickerman, J. C., Brown, A., and Reed, N. M., *Secondary Ion Mass Spectrometry: Principles and Applications*, Oxford University Press, New York (1989).

Wang, L., Wolk, J. A., Hsu, L., Haller, E. E., Erickson, J. W., Cardona, M., Ruf, T., Silviera, J. P., Briones, F., *Appl. Phys. Lett.* **70** 1831 (1997).

Watkins, G. D., Corbett, J. W., and McDonald, R. S., *J. Appl. Phys.* **53** 7097 (1982).

Watkins, G. D., in *Deep Centers in Semiconductors, A State of the Art Approach* edited by S. T. Pantelides (Gordon and Breach Science Publishers, New York) p. 147 (1986).

Weber, E. R., *Appl. Phys. A* **30** 1 (1983).

Werner, M., Mehrer, H., Hochheimer, H. D., *Phys. Rev. B* **32** 3930 (1985).

Windl, W., Bunea, M. M., Stumpf, R., Dunham, S. T., and Masquelier, M. P., *Phys. Rev. Lett.* **83** 4345 (1999).

Zangenberg, N. R., Lundsgaard Hansen, J., Fage-Pedersen, J., and Nylandsted Larsen, A., *Phys. Rev. Lett.* **87** 125901-1 (2001).